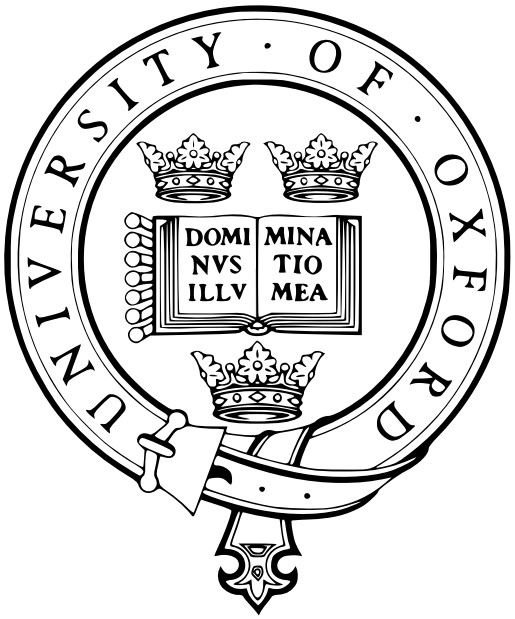


Tactoid formation in suspensions of Pf4 virus particles and the role of impurities

Mariana de Oliveira Silva

St Peter's College
University of Oxford

Supervisor: Prof. Dirk G. A. Aarts

A thesis submitted for the degree of
Doctor of Philosophy

22/11/2022

To my aunt Nene, my friend Flavia
and all COVID-19 victims.

When education is not liberating,

the dream of the oppressed is to become the oppressor.

Paulo Freire

Acknowledgements

I want to start by thanking my research group. My supervisor, Dirk Aarts, for the guidance, the great chats, and new scientific perspective. I will most definitely miss your puns. Thank you Adam and Alice for the warmest welcome; Joe and Miranda for the fascinating conversations; Jack, for introducing me to the wonderful world of croquet; Callum, for the best birthday card ever and the most productive office conversations; Camille, for the partnership and becoming such a good and special friend; Lucia, Taiki, Nick, Olivia, Johnny, Lizzie, Iago, and all my other lab mates. You have made this phase much more special. I will never forget pub Fridays.

I am grateful for the staff in the Department of Chemistry and the Physical and Theoretical Chemistry Laboratories. Sometimes we may not see you, but you made sure all the work was possible to happen. Special thanks to Paul for all the patience and help provided.

To Iago and our collaborators Dr Abul Tarafder, Prof Tanmay Bharat, Dr Yucen Han, Prof Apala Majumdar, Yucen, and Prof Lei Zhang , thank you for the samples, calculations, and discussions - they were fundamental to enrich this work.

To my friends of new. You made my journey in Oxford worth so much more. Jess and Steve, thank you for all the support, especially in the last few months. You taught me a lot (very important things such as playing zombicide). I hope to be like you when I grow up. Deborah, thank you for enjoying arts, trips, and so many other joyful aspects of life with me. I am grateful to Sensei Chris, Andy, Natsumi, Paolo, and all Shorinji Kempo kenshi. You helped me to be a better person while still having a great time. Natalia for all the dancing and friendship. My former housemates, Amy, Pat, and Vania, for all the dinners and laughs. My new Brazilian friends, Ba, Lu, Vinicius, Isa, Licio, Rafha, and Ze. Nat thanks for sharing my neediness and showing me that all the chemists are crazy and special. Bia for sharing the dream of seeing a better Brazil.

I don't want to prolong myself too much. All that I said in my master thesis is (thankfully) still true, but I could not thank again some people. Mom Nilza and my aunt Vera, Dede, and

Nene. You taught me to be strong, and kind, and to believe in myself. Thank you for all the support and love. My cousin Caren, thanks for always being there and sharing a similar wish to just be who you are. To my cousin Paulo and my new baby cousin Giulia, you will always be *mon ami*. It was incredible having you so close.

To my friends from old, thank you for still being here so present. Bia and Beavis, I lack the words to describe how important you are to me. Filipe, thanks for all the lengthy discussions (especially the silly ones). Elisinha, thank you for always bringing new perspectives. Dri and Ju, thanks for being there, even when it is hard. Bianquinha, thank you for all your patience and support with my crazy ideas. You inspire me not to give up on my dreams and being healthy. Marilia, after 20 years of friendship what more can I say?

These four years were some of the best and hardest of my life. I would not have made it this far without your support. Thank you for being part of my life.

Acknowledgement of funding

This study was financed in part by the Coordenação de Aperfeiçoamento de Pessoal de Nível Superior – Brasil (CAPES) - Finance Code 001

Abstract

In this work, we first studied the synthesis of bent-core particles and if they could be used as model particles or for the formation of lyotropic liquid crystals. We used perturbation to obtain a kink, with temperature proven to be successful. We noticed a significant dependency with the base concentration and with the extension of TEOS pre-hydrolysis. However, these two parameters are hard to control, especially the second one, resulting in a synthesis hard to reproduce.

Our main goal was to understand the behaviour of tactoids (nematic droplets in an isotropic medium) formed in suspensions of sodium alginate and Pf4 virus and the role of impurities. This virus is of increasing interest due to its role in the protection of the pathogen *P. aeruginosa* against antibiotics. We explored the synthesis of spherocylindrical silica rods to mimic these bacteria and modified the particles to obtain positive or hydrophobic surfaces.

We then studied the phase behaviour of the tactoids with confocal microscopy to evaluate their growth, size, and to obtain a phase diagram. We found a dependence on the size and growth time with the concentration of polymer, in which a low concentration of sodium alginate led to slow kinetics and bigger tactoids. The number density of tactoids was related to the concentration of phage. We obtained an experimental phase diagram in which isotropic and biphasic regions were obtained, with the latter being further seen as tactoids or network structures. The comparison with the theoretical phase diagram showed good agreement.

Subsequently, we investigated the interaction of tactoids with different rods (bacteria *B. subtilis* and *E. coli* and synthetic silica and SU8 rods) as impurities. Four different configurations were found and classified as no attachment, partial attachment, sandwich and encapsulation. Partial attachment was the state seen most frequently and encapsulation was only seen for *E. coli* and SU8 rods. We found a relationship between the length of the tactoid and the length of the rod and the aspect ratio of the rod itself for each configuration. Changes in the surface of silica rods did not result in encapsulation, indicating the particle's topography

is also important. To further understand this problem, we explored the system theoretically, by looking exclusively at the elastic energy of the encapsulated configuration, and then by investigating all energy components of a free boundary tactoid. With this second model, all the states obtained empirically were found as well as a relationship with the anchoring strength. We further noticed that the rod prefers to be close to the tip of the tactoid since the proximity of the defects minimizes the energy of the system, with high aspect ratio rods having a smaller energetic cost. Furthermore, having a quasi-2D system alters the system and encapsulation was obtained for all the impurities evaluated.

Finally, we explored the rheological behaviour of the Pf4-sodium alginate system. The presence of tactoids resulted in an increase in viscosity, but the sample was still fluid-like. Differently, we saw a transition from solid- to liquid-like at concentrations where networks were formed. These results were compatible with the observations seen with the confocal microscope and this behaviour may relate to the biofilm's ability to protect against pathogens.

Declaration

This thesis is submitted for the degree of Doctor of Philosophy in Physical and Theoretical Chemistry at the University of Oxford. No part of this thesis has been accepted or is currently being submitted for any degree, diploma, certificate or other qualification in this University or elsewhere. This thesis is wholly my own work, except where indicated.

Contents

Acknowledgements **i**

Abstract **iii**

Declaration **v**

1 Introduction **1**

1.1 Colloidal domain 1

1.1.1 Depletion interaction 2

1.2 Liquid Crystals 3

1.2.1 Isotropic-Nematic transition 6

1.2.2 Rotational diffusion and viscosity 8

1.2.3 Elastic Energy 9

1.2.4 Defects 10

1.2.5 Anchoring 11

1.2.6 Tactoids 12

1.3 Biological background 14

1.3.1 Rheology of Biofilms 16

1.3.2 Thesis outline 18

2 Theoretical background and experimental methods **19**

2.1 Materials 20

2.2 Experimental methods 20
2.2.1 Pf4 isolation and purification 20
2.2.2 Synthesis of SU8 rods 21
2.2.3 Bacteria growth and staining 21
2.2.4 Tactoid formation 22
2.3 Theoretical background of experimental methods 25
2.3.1 Microscopy 25

3 Synthesis of silica rods 31

3.1 Introduction 32
3.2 Synthesis background 32
3.2.1 Sol-Gel route 32
3.2.2 Silica rods synthesis 34
3.2.3 Surface modification 35
3.3 Experimental methods 36
3.3.1 Materials 36
3.3.2 Straight rods synthesis 37
3.3.3 Spherocylindrical rods 38
3.3.4 Bent silica rods 38
3.3.5 Silica rods - Surface Modifications 39
3.3.6 Characterization 40
3.4 Results and Discussion 41
3.4.1 Straight Rods 41
3.4.2 Surface modification 43
3.4.3 Bent Rods Synthesis 45
3.5 Conclusion 55

4 Phase behaviour of Pf4 and sodium alginate 57

4.1 Introduction . . . 58
4.2 Experimental methods and materials . . . 59
4.2.1 Phase diagram theoretical background . . . 61
4.3 Results and Discussion . . . 66
4.3.1 Kinetics . . . 66
4.3.2 Size . . . 69
4.3.3 Phase Diagram . . . 73
4.3.4 Theoretical phase diagram . . . 77
4.3.5 Conclusion . . . 80

5 The effect of impurities on the behaviour of Pf4 tactoids 83

5.1 Introduction . . . 84
5.2 Experimental Method . . . 85
5.3 Theoretical background . . . 86
5.3.1 Elastic energy of tactoid . . . 86
5.3.2 Free boundary numerical model . . . 90
5.4 Results and Discussion . . . 93
5.4.1 Experiments with bacteria . . . 93
5.4.2 Experiments with synthetic rods . . . 95
5.4.3 Experiments with surface modified silica rods . . . 97
5.4.4 Elastic energy calculations . . . 99
5.4.5 Numerical model . . . 105
5.4.6 Quasi 2D experiments result . . . 107
5.5 Conclusions and Outlook . . . 108

6 Rheological behaviour of Pf4 and sodium alginate mixtures 111

6.1 Introduction . . . 112
6.1.1 Rheology basics . . . 112

6.1.2 Motivation and outline 116
6.2 Experimental method 117
6.3 Results and discussion 118
6.3.1 Tactoid samples 119
6.3.2 Network samples 121
6.4 Conclusions and outlook 123

7 Conclusion **125**

Bibliography **129**

Chapter 1

Introduction

In this chapter, we will introduce the most important topics for this thesis. We will begin by explaining what the colloidal domain is, the importance and use of colloidal particles, and of the depletion interaction. Then, we will introduce liquid crystals, covering the isotropic-nematic transition, elastic energy, defects, anchoring and tactoids. We will finish the chapter by presenting a short biological background. These topics are important since the aim of this work is to study the behaviour of Pf4 phage (colloidal particle) in a biphasic (isotropic-nematic) system, with the choice of this specific virus being made based on its important biological role.

1.1 Colloidal domain

Colloidal particles are traditionally defined by their dimensions with at least one component in the order of nanometres to a few micrometres. These dimensions are situated between atoms and molecules (microscopic) and biological systems (macroscopic). There is no abrupt transition, and colloids have characteristics associated with the micro- and macro-world, being classified as mesoscopic [1]. They can be considered a supramolecular component dispersed in a medium considered as "background" and approximated as continuum [2].

Due to the dimensions, the individual particles' behaviour is classical, and several phenomena are observed, such as the self-assembly of different structures. As a result, colloidal particles have multiple uses in industry (e.g. food, coating, petrochemical) and research. They form different phases and the transitions are similar to atomic and molecular systems, giving insight

into how matter organizes. Hence, they can be used as probes and help answer fundamental questions of soft matter and material science [3].

With packing constraints, colloids allow us to understand how entropy and geometry govern the structure and the dynamics of self-assembly. When the concentration of particles increases, the space available for translation is larger in an ordered state than in a disordered one [3]. This ordering is effectively a phase transition due to entropy and was first shown by Onsager for infinitely long hard, going from the isotropic to the nematic phase [4].

The similarities in the behaviour of colloids and atoms, especially the random motion of particles in the absence of an external field, called Brownian motion, lead to them being used for decades as model atoms [5,6]. The statistical mechanics' foundation for the colloid-atom analogy was developed by Einstein [7], Onsager [8, 9], and McMillan and Mayer [10]. They showed that the solvent can be considered a "background", meaning its degrees of freedom can be eliminated. In this way, the only interaction between the particles is an effective potential, which accounts for the medium. Because of their sizes and typical time scale (seconds), they can be easily imaged with optical microscopy, making it possible to determine the particle position and orientation, and thus determining the behaviour directly, instead of obtaining indirect measurements as scattering techniques [11].

There are limitations to using colloids as probes since they have their own behaviour not found on the atomic scale [3]. They show reduced colligative properties when compared to molecules in the same mass concentration [1]. And, differently from the pair interactions found in atoms, the interaction among colloids can be tuned by changing the particle type or size, system temperature, solvent used and adding another compound such as polymers or electrolytes [1, 2, 6].

1.1.1 Depletion interaction

In the presence of a non-adsorbing polymer or small particles, colloids feel an "effective attraction through repulsion", called the depletion interaction. Even though all the individual interactions (colloid-colloid, colloid-polymer, polymer-polymer) in the system are repulsive, the particles are brought together. Near the colloidal surface, there will be a loss of configurational entropy for the polymer which results in a depletion layer. When the particles come close and these

depletion layers overlap, the local osmotic pressure pushes the particles against each other. The final result is the available volume for the polymer increases, and an effective attractive force between the colloidal particles [2, 12, 13], as schematically shown in figure 1.1.

The depletion attraction can be modulated by changing the size of the depletant, which affects the range of the interaction. Adjusting the concentration (and, consequently, osmotic pressure) modifies the interaction strength [2, 12, 13]. The surface roughness is also important when the dimensions are similar to the depleting particles, with smooth parts acting as attractive patches [14].

Since colloids are found in a wide range of environments and products, which also contain more than one particle and/or polymer, depletion is an important effect. Understanding this interaction and the possible tuning allows us to obtain the desired effect and study phase behaviour. Viruses are commonly precipitated and isolated using PEG as a depletant [15, 16], but using different polymers and concentrations, liquid crystalline droplets can be obtained [2]. Both cases will be important and used in this thesis.

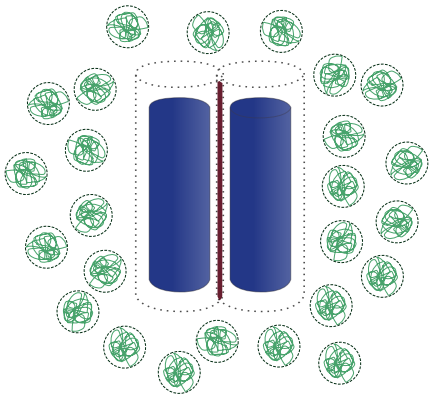


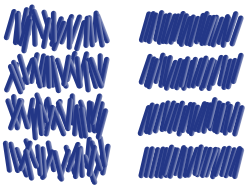
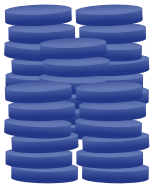
Figure 1.1: Schematic of the depletion interaction in which the green bundles, the rods in blue and the dotted line represent the polymers, the colloidal particles, and the excluded volume, respectively.

1.2 Liquid Crystals

Liquid is a state of matter capable of flowing, defined by its viscosity, while a solid is characterized by its elasticity. On the atomic scale, liquids are organized at short-distance while crystalline solids have long-range order. The state of matter characterized by properties and molecular organization between the ones found in liquids and solids is called the liquid crystalline state. Liquid crystals (LC) can flow and present molecular organization in at least long-range orientational order [17, 18].

Liquid crystal phases are formed by anisotropic particles with some rigidity, such as rods or discs, called mesogens. The various liquid crystalline phases have different degrees of order and are formed by changes in concentration (lyotropic) or temperature (thermotropic), depending on the mesogen. The least ordered LC phase is the nematic, in which the molecules do not have positional order, but, on average, the main axis of all molecules is oriented in the same direction. More organized phases are smectic, in which there is also a layering arrangement (1D positional order plus orientational order) and columnar (2D positional order plus orientational order) as summarized in table 1.1 [18, 19].

Table 1.1: Summary of the main liquid crystalline phases. For the smectic phase, the molecules are aligned within each layer, with the director parallel to the layer normal for SmA and the director and layer normal making an angle for SmC.

Phase	Positional order	Orientational order	Schematic
Isotropic liquid	None	None	
Nematic	None	Yes	
Smectic	1D	Yes	
Columnar	2D	Yes	
Crystalline	3D	Yes	

In this thesis, we will focus on the nematic phase, where all the molecules are on average oriented along a common axis. This axis is represented by a unit vector called the director (**n**), and a schematic representation is shown in figure 1.2. The order parameter is used to describe the magnitude of the orientational ordering by obtaining the average orientation of each mesogen. The scalar order parameter can be calculated as

$$S = \left\langle \frac{3}{2}\cos^2 2\theta - \frac{1}{2} \right\rangle = \langle P_2(\cos\theta)\rangle, \tag{1.1}$$

where θ is the angle between the molecule's long axis and the director and P_2 is the second Legendre polynomial [20].

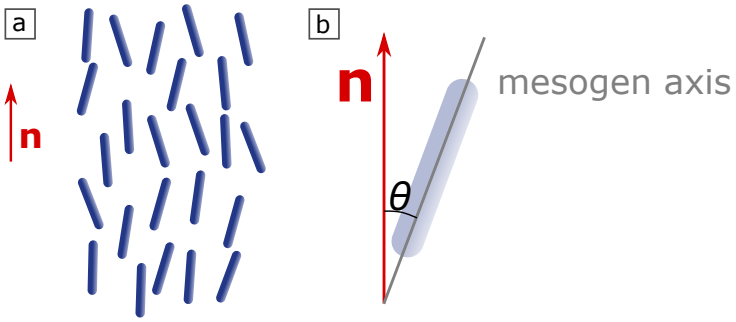


Figure 1.2: Schematic of the director (**n**) for (a) a nematic phase, and (b) of the angle θ between the director and the mesogen axis.

A value of $S = 0$ is obtained when there is no alignment, representing the isotropic phase. Values between 0 and 1 describe the nematic phase, and 1 is the perfect nematic. Experimentally obtained values are usually between 0.7 and 0.8 [18, 19]. The order parameter is even in **n**, meaning that +**n** and -**n** represent the same physical state, and are equivalent. The director is distributed around a unit sphere, uniformly and randomly for the isotropic, and non-uniformly for the nematic phase. This distribution is described by the orientational function $f(\theta)$. Since for the isotropic, the director is uniformly distributed, there is an equal chance of the molecule pointing anywhere at a solid angle 4π, so

$$\int f(\theta)\, d\mathbf{\Omega} = 1, \tag{1.2}$$

$$f(\theta) = \frac{1}{4\pi} \text{ for the isotropic phase,} \tag{1.3}$$

where $(\theta)d\Omega$ is the fraction of molecules in a solid angle $d\Omega$ which are oriented at an angle θ from the director [17].

1.2.1 Isotropic-Nematic transition

The transition from the isotropic to the nematic phase (I-N transition) leads to a reduction in orientational entropy, so another factor must drive the phase change. For small molecules, this is usually compensated by favourable attractive interactions, such as van der Waals forces. For concentration transitions, a gain in translational entropy is the driving force [18, 19]. The theoretical study of liquid crystal phase transitions can be described by molecular field (such as Maier-Saupe or Onsager) or phenomenological (such as Landau-de Gennes) theories. Maier-Saupe and Landau-de Gennes are more suitable for the transition of thermotropic LC [17]. For lyotropic, Onsager theory is applied and is the one used in chapter 4.

Onsager

Onsager developed a theory, assuming the liquid crystal is composed of infinitely long hard rods with only excluded-volume repulsion interaction (eq. (1.4)).

$$\text{Interaction potential } V_{ij} = \begin{cases} 0 & \text{if no overlap} \\ \infty & \text{if overlap} \end{cases} \tag{1.4}$$

This repulsion prevents them from overlapping, thus the rod's centre of mass cannot be inside the overlap region. For a rod of length L and radius D, this region comprises a parallelepiped with height L, width $L|sin(\theta)|$ and depth $2D$ (excluded volume $v_e = 2DL^2|sin(\theta)|$), with θ being the relative orientation between the two rods as shown in figure 1.3 [4].

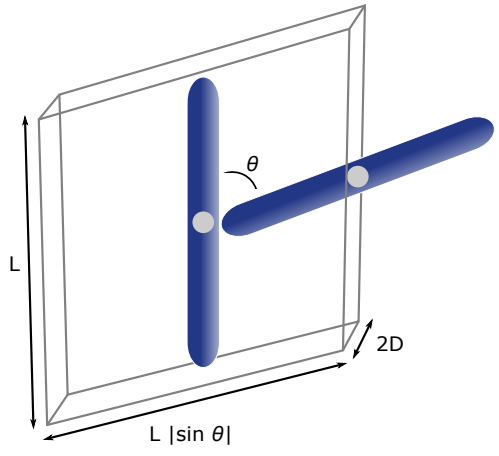


Figure 1.3: Representation of the excluded volume of a rod, which depends on the angle θ between the rods.

Since the excluded volume depends on the relative orientation of the particles, alignment minimizes the excluded volume and increases the translational entropy. This favours the nematic phase, while the orientational entropy favours the isotropic phase. Thus, the phase transition is purely entropic and will occur at a certain (dimensionless) concentration c

$$c = \frac{\pi}{4} L^2 D \frac{N}{V} = \frac{L}{D} v_0 \frac{N}{V} = \frac{L}{D} \phi, \tag{1.5}$$

where v_0 is the volume of the rod (assuming a cylinder) and ϕ is the volume fraction. The excluded volume is used since the interaction is dependent on this parameter rather than on the actual volume of the rod. Since the volume fraction required for the phase transition is inversely proportional to the aspect ratio L/D, the excluded volume will become more important with an increase in aspect ratio or in volume fraction. In reality, additional interactions are present in the systems besides the excluded volume, the rods may not be stiff, and so forth. The theory was developed for infinitely long rods; thus, modifications are needed for shorter ones [4].

Between the pure isotropic and nematic, a biphasic region is found, in which both phases coexist. They can be macroscopically separated, but in this work, they are found as nematic droplets in an isotropic medium as will be explained in section 1.2.6. In the presence of polymer (depletion interaction), the limit of the biphasic region opens up. Figure 1.4 shows an example of a theoretical phase diagram, and further details of this topic will be given in the theoretical background of chapter 4 (section 4.2.1).

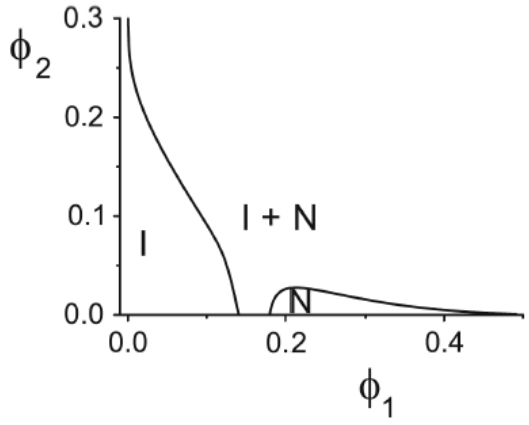


Figure 1.4: Theoretical phase diagram of a mixture of hard rods with polymer, where ϕ_1 and ϕ_2 are the volume fraction of rods and polymers, respectively. In the diagram, I is used for the isotropic phase, N for the nematic and I+N for the biphasic region. Extracted from [2].

Polydispersity and flexibility

The polydispersity of the mesogens influences the IN transition - it widens the coexistence region. The transition also becomes less defined, and it is more difficult to do a theoretical analysis. Flexibility also affects this transition. It suppresses the concentration gap between the coexistence domain (eg. Fd reduced to 10 % of the concentration of the coexistence isotropic phase from 30 % predicted for rigid rods) [21].

1.2.2 Rotational diffusion and viscosity

The movement of rod-like particles is highly dependent on the concentration of particles in the solution. For a very dilute solution, the Brownian motion dominates and it is independent of the concentration. As a result, the rods are free to move and the viscosity of the solution is the viscosity of the solvent. Differently, when the concentration of the system increases, the motion of the rods is restricted, due to the entanglement of the particles. Doi has shown that for an entangled, but thermodynamically ideal solution (so below the IN transition concentration) that a thin rod is able to always move in the direction of its own axis, but can only move the distance given between its centre of mass and the nearest rod (small distance); in this way, the perpendicular translation is forbidden. Furthermore, the rotational motion is restricted, being hindered by other rods [22], with the diffusion coefficient (D_r), being proportional to the diffusion coefficient for a dilute solution (D_{r0}), the concentration of rods in the solution (c) and the length of the rods (L):

$$D_r \approx D_{r0} c^{-2} L^{-6} \tag{1.6}$$

where

$$D_{r0} = \frac{3kT(L/D)}{\pi \eta_s L^3}, \tag{1.7}$$

D is the diameter of the rod, and η_s is the viscosity of the solvent, so

$$D_r \propto c^{-2} L^{-9} \tag{1.8}$$

The drastic decrease in rotational diffusion constant is the main reason for the non-

Newtonian viscoelasticity of a solution containing rods. In a dilute solution, the viscosity is highly dependent on the viscosity of the solvent:

$$\eta \approx \eta_s + \frac{ckT}{D_{r0}} \approx \eta_s(1 + cL^3) \tag{1.9}$$

Then, in a concentrated solution, since D_{r0} is substituted by D_r, the viscosity of the medium is much greater than the viscosity of the solvent and is highly dependent on the length and concentration of the rods

$$\eta \approx \eta_s(1 + (cL^3)^3) \tag{1.10}$$

1.2.3 Elastic Energy

Any variation in the director as a function of the position will result in mesogens not being uniformly aligned and will lead to an increase in free energy. Three main deformations can be defined: splay, twist and bend. Each one of them is defined by the relationship between the director and the gradient direction [23, 24]. A schematic representation of these modes is presented in figure 1.5 [19].

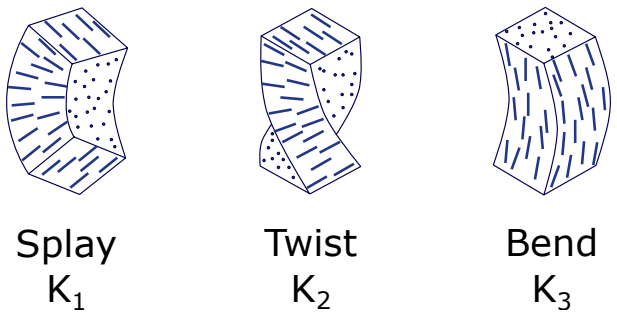


Figure 1.5: Schematic representation of the three main deformations. Adapted from [25]

The total elastic cost can be described by the Oseen-Frank energy [23, 24],

$$E[\mathbf{n}] = \iiint \frac{1}{2}(K_1(\nabla \cdot \mathbf{n}))^2 + K_2(\mathbf{n} \cdot \nabla \times \mathbf{n})^2 + K_3(\mathbf{n} \times \nabla \times \mathbf{n})^2 \, d\Omega, \tag{1.11}$$

in which the constants $K_1, K_2,$ and K_3 are related to the splay, twist and bend deformations, respectively. Note that in a more complete model the splay-bend deformation, proportional to $K_2 + K_4$ is also considered. In cases where there is anchoring by a surface, the saddle-splay term is constant and independent of the director field in the bulk, so it can be neglected. The

three main constants may be different and depend on the physical properties of the mesogens, such as length, aspect ratio and stiffness [26, 27]. Usually, K_3 is bigger than K_1 and K_2, but they are of the same order of magnitude and scale as $k_B T/L$ [28]. It is common to use the one constant approximation ($K_1 = K_2 = K_3 = K$) to calculate the elastic cost, which simplifies the calculation [29]:

$$E[\mathbf{n}] = \frac{K}{2} \iiint_{\Omega} |\nabla \mathbf{n}|^2 \, d\Omega. \tag{1.12}$$

1.2.4 Defects

Certain distortions in the director cannot relax and dissipate, called topological defects, which can be points or lines, called disclinations. The types of defects able to form are dependent on the symmetry of the phase, so, especially for molecular LCs, they can help to identify the phase. A few examples are shown in figure 1.6 [18, 19, 30].

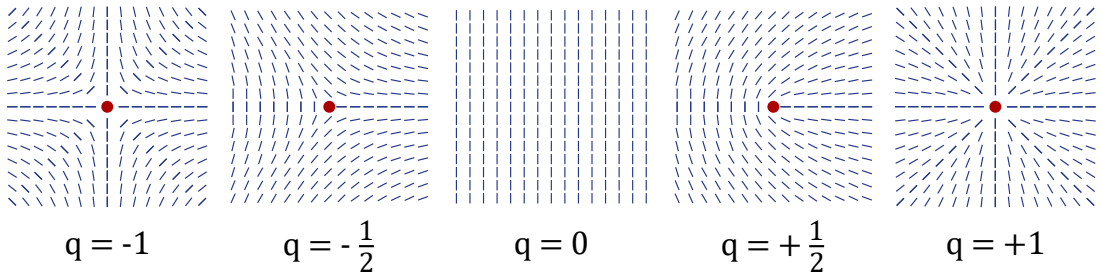


Figure 1.6: Schematic representation of a nematic phase ($q = 0$) and defects with their correspondent topological charge (q).

These defects are characterized by a topological charge (q in figure 1.6) obtained through the Burgers circuit. In essence, the charge is determined by looping around the defect, obtaining the angle change, and dividing this value by 2π. A region without defects will result in zero value. For the nematic in bulk, the defect charge can be an integer or half-integer [18, 19, 30].

All defects result in considerable distortion of the director over a long range, which, consequently, will cost a certain amount of elastic energy [18, 19]. Assuming the one constant approximation, the Frank-Oseen free energy can be written, in 2D per unit length, as

$$E[\theta] = \frac{K}{2} \iint |\nabla \theta|^2 \, r \, dr \, d\theta. \tag{1.13}$$

The absolute minimum of eq. (1.13) is obtained for the uniform director field. However, the

defect represents a local minimum. We can obtain the elastic cost of the defect following a scaling relation $\nabla\delta \approx q/r$, which leads to

$$F = \int_0^\infty r\,dr \int_0^{2\pi} \frac{1}{2} K \frac{q^2}{r^2}\,d\theta \tag{1.14}$$

$$= \pi K q^2 [\ln(r)]_0^\infty, \tag{1.15}$$

in which the term $[\ln(r)]_0^\infty$, diverges at both limits. The Frank elastic theory assumes the magnitude of the nematic order (S) is constant, but close to the defect, $\mathbf{n}$, changes considerably, so the gradient is large, resulting in a significant elastic cost. The theory does not apply at short distances and trying to apply this model when $r \to 0$, will result in infinity energy, called the ultraviolet divergence – the natural cut-off for short length scales is the size of the defect.

In a simulation, a small region around the defect may melt (i.e., become isotropic). There are multiple ways to avoid this problem, and the most common is to assume a core around the defect, with a radius in the order of the typical length scale of the mesogens which has an energy E_{core}. Outside the core radius, the Frank elastic energy is applicable [29].

The other limit, as $r \to \infty$, is called the infrared divergence. It happens at large distances, where the Frank elastic energy theory is no longer valid. To avoid this problem, in simulations, the limit has to be cut off to a maximum value for the sample size.

1.2.5 Anchoring

In the presence of a surface, the mesogen orientation is changed, a phenomenon called anchoring. In the case of a nematic phase, the director aligns according to the interactions with the surface. Two parameters can define this phenomenon, preferred axis (or "easy axis") and strength, which are characteristic of a particular surface [18, 31].

There are three possible preferred axes of orientation - planar, tilted or homeotropic. In the first, the director is tangent to the surface and if all mesogens are on the same axis it is called homogeneous, otherwise, it is degenerate anchoring. In the tilted orientation, the director is at a certain angle with the surface, and homeotropic is a specific case, where the director is perpendicular to the surface [18].

Anchoring competes with elastic energy, and the ease with which the proposed orientation

is changed depends on the anchoring strength. If the surface forces are stronger than the elastic cost, then the molecules will align according to the surface preferred axis and this will be called strong anchoring (a Dirichlet boundary condition) [18]. Else, if the anchoring is weak, then the alignment will not be complete. The latter is more common than the former, part of the reason why strong anchoring approximations can deviate from reality [31].

The specific direction near the surface the LC director follows, propagates up to a certain distance in the bulk from tens of nanometres to tens of micrometres (mesoscopic phenomenon). This is measured by the extrapolation length(ξ) and is a way to determine the competition between surface anchoring and elastic energy. For the one constant approximation, it can be expressed as

$$\xi = \frac{K}{w}, \tag{1.16}$$

where K is the elastic constant and w is the anchoring constant [17, 18].

The anchoring orientation is dependent on the chemical and physical properties of the surface, with surface chemistry and topography as two important parameters. The topography of an object is related to its shape, size and geometry, and it has been experimentally related to the anchoring preferred axis, for instance with the presence of grooves. The actual effect of surface chemistry in anchoring is commonly related to surface tension and a few empirical relations have been found [32].

However, surface anchoring involves several mechanisms, and the "easy axis" of a surface is usually discovered empirically [33]. The molecular details are still not completely understood [31] and this is related, in part, to the difficulty to characterize surfaces, so they are not very well defined [34]. Measuring interactions at the molecular scale is difficult, so only a few systems have been characterized enough to elucidate the mechanisms of the surface physical chemistry on the anchoring [32].

1.2.6 Tactoids

Tactoids are droplets of nematic phase in an isotropic medium that may be formed in the coexistence region of the two phases. These tactoids have been found in molecular, polymeric and colloidal lyotropic liquid crystals, including viruses such as *fd*, and tobacco mosaic viruses (TMV). They can initially form by nucleation and growth or after phase separation by spinodal

decomposition. The coalescence of tactoids has been seen in lyotropic liquid crystals, e.g. *fd* viruses [35], cellulose nanocrystals [36], and F-actin [37].

Tactoids are an out-of-equilibrium phase [38]. In certain mesogens, like CNC, no phase separation is observed. This is possibly due to the high viscosity of the system or the similar density between the isotropic and nematic phases, resulting in slow tactoid sedimentation [20]. The viscosity of the medium is dependent on the rotational diffusion of the rods for a highly concentrated solution. To better understand this, we will look at Doi [22].

The shape and director field of the tactoid depends on the competition between the elastic, and the surface (anchoring and surface tension) properties of the liquid crystalline phase [39–41]. The latter favours a spherical and the former an elongated shape, so the balance of these will determine the shape depending on the size of the droplet [39, 40]. The director can be homogeneous or bipolar as shown in figure 1.7, with strong anchoring between the director and boundary (tangential boundary condition) [41]. Larger droplets tend to prefer being symmetrical due to the high surface cost, being bipolar if the surface tension is strongly anisotropic or homogeneous otherwise. Smaller droplets are more elongated, spindle-like, due to the higher elastic cost, and the director is dependent on the anchoring strength. There is also a dependency on the aspect ratio of the rod with more elongated rods having a higher resistance to being bipolar [39, 40].

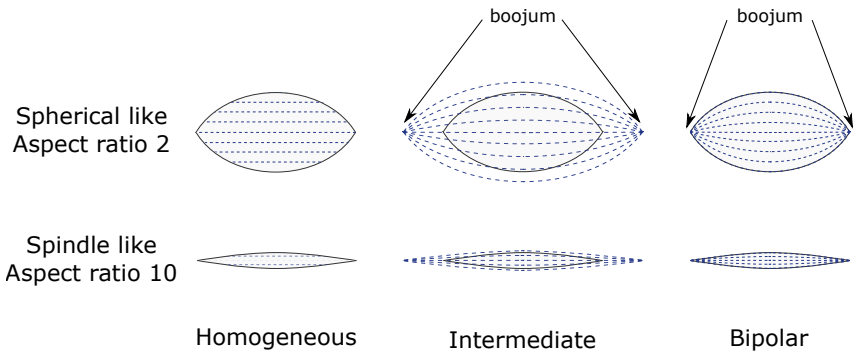


Figure 1.7: Schematic representation of tactoids with different aspect ratios and director, with the defect (boojum) at the tip or outside the tactoid.

The weight elastic and surface properties have on the tactoid shape and director field will also depend on characteristics of the mesogens, such as aspect ratio and rod length [28, 42]. For example, for sulfated CNC no bipolar director field is observed, indicating this mesogen presents a high bending constant [28]. With amyloid fibrils, it is possible to observe that specific shapes and configurations are obtained depending on the fibril length. Cholesteric droplets (chiral

nematic phase) are only obtained for shorter ones, while for longer fibrils highly elongated tactoids are seen [42].

Following the IN transition from the nucleation and growth of tactoids, and up-concentration until a state of equilibrium is reached. Using different elastic constants and surface tension for each mesogen used, it was observed that different multiple-order-order phase transitions occur and that the growth of the tactoids is connected with the concentration in each phase. Again, depending on the characteristic of the mesogen, different phases are seen as the tactoids grow [43]. The IN order transition is dependent on the length of the fibrils. For short ones, first-order transitions are observed [38]. The relaxation paths that lead to the different shapes and structures (tactoid vs cholesteric droplet and director) have also been studied. The shape relaxation is always a single exponential decay - an out-of-equilibrium process governed by the iso- and anisotropic contributions of the nematic phase. Differently, the structural relaxation can be first or second order depending on the elastic constants and on the size of the tactoid [44].

Tactoids grow through two different mechanisms: nucleation and growth and spinodal decomposition. Both mechanisms have been observed for F-actin and the mechanism followed depends on the initial concentration of mesogens and on the average filament length. When the concentration is past the onset of IN transition, nucleation and growth are observed. At roughly in the middle of the transition region, and for short rods, spinodal decomposition is followed. The final size of the nematic droplet was similar independent of the mechanism followed [38].

The formation of tactoids by viruses is well known for *fd* [45, 46] and TMV [47, 48], by themselves or in the presence of polymers [49]. However, their importance in biofilms and microbiology was shown more recently. Secor *et al.* showed that rod-shaped Pf4 phage has a symbiotic relationship with *P. aeruginosa* and forms a liquid crystalline matrix in their biofilms [50]. Afterwards, Tarafder *et al.* showed this protection is connected with the encapsulation of these bacteria by the Pf4 tactoid [51], and we will explore this further in the next section.

1.3 Biological background

Microorganisms do not live as individual cells or pure cultures. They form colonies encased by a highly hydrated extracellular polymeric matrix (EPS) called biofilms. In most biofilms, the cells represent 10 % of the dry mass while the matrix represents the other 90 %. Usually, they

are formed at a liquid-solid interface [52].

The exact composition of EPS is varied and difficult to be determined. It depends on the microorganisms present, temperature, availability of nutrients and mechanical history [52]. They are produced by the microorganisms present and consist mainly of biopolymers, including polysaccharides, proteins, nucleic acids and lipids. Due to the concentration of polymers, a 3D network is formed, which immobilizes the cells, allowing them to interact, for example, by communicating through electrical signals. Additionally, this network guarantees the mechanical stability, adhesion of the biofilm, and retention of water [52].

Biofilms and their protection against infections and antibiotics are considered by some as one of the most successful forms of life on the planet, and one of the main challenges when studying antibiotic resistance [52]. *P. aeruginosa* is the main pathogen responsible for the morbidity and mortality of patients with cystic fibrosis, also causing severe infections in patients with a compromised immune system [53]. These bacteria are becoming resistant to the antibiotics used to treat the disease, increasing the risk of mortality associated with it. This has resulted in the pathogen being considered of critical priority for the development of new treatment by the World Health Organisation [54]. This shows the importance of understanding the mechanism of defence these bacteria use when developing new treatments against infections.

Among the components found in biofilms, bacteriophages can also be found, with their production being regulated by bacterial factors [55]. Evidence indicates that the Pf virus has a symbiotic relationship with the *P. aeruginosa* bacteria, showing that phages are upregulated and are also found in the sputum of CF patients [56–58]. Additionally, a higher concentration of Pf in the sputum of patients with CF was correlated with increased age and antibiotic resistance, and high concentrations of the Pf4 virus do not result in biofilm eradication [59]. The presence of Pf in these patients was also related to an increase in chronic infection and a drop in pulmonary function [60]

Secor *et al.* [50] showed that the symbiotic role within *P. aeruginosa* biofilms happens through the formation of a liquid-crystalline matrix. Pf4 are filamentous and rod-shaped viruses with a diameter of 6 to 7 nm and 1 to 4 μm in length and are able of forming lyotropic liquid crystals [51]. In the presence of a non-interacting polysaccharide, the filaments experience the depletion interaction, which promotes the formation of tactoids [45, 46].

The formation of these droplets increases the viscosity of the medium, enhancing the protection offered by the biofilm through an increase in adhesion and tolerance to antibiotics and desiccation. These structures are negatively charged, so Secor *et al.* proposed that the protection they provide comes from sequestering positively charged antibiotics [50]. Tarafder *et al.* showed that not only do these viruses form a tactoid but also that these droplets encapsulate the bacteria. In the presence of sodium alginate and Pf4, the bacteria resistance against antibiotics is higher than if only one component or none are present, even if using ghost filaments (not charged), indicating that the formation of tactoids is responsible for the protection of the bacteria [51].

1.3.1 Rheology of Biofilms

Cystic fibrosis is a disease that leads to the presence of thick mucus, which is difficult to clear, that builds up in the patient's organs, including the lungs. Due to that, biofilms can be more easily formed and are harder to clear. This results in chronic pulmonary infections of the patient, with *P. aeruginosa* one of the main pathogens responsible for these infections. Due to the ability of this organism to adapt, different classes of *P. aeruginosa* have been characterized with the ability to overproduce certain exopolysaccharides [61].

Studies of the extracellular polymeric substance (EPS) of *P. aeruginosa*, after removal of the bacteria, showed that a diluted aqueous solution of EPS has low elasticity, with cross-links formed in the presence of calcium ions [62]. This mechanism is the same observed in sodium alginate aqueous solutions, a polymer commonly found in the biofilm of this pathogen. Calcium is naturally present in the EPS and the increase in alginate results in the entanglement of the chains and formation of electrostatic junctions. The addition of extra calcium results in the formation of permanent junctions and a stronger gel. This indicates the importance of alginate and calcium for the elastic properties of the biofilm [62], even in the presence of the bacteria [63, 64].

These pieces of information are important because the clearance of mucus and biofilm is connected with their viscosity and elasticity. The two mechanisms by which mucus is expelled from the lungs are mucociliary and cough. The first constitutes of the cilia movement being responsible for the shift of the mucus whereas the second one is related to a burst of high-velocity air. The mucociliary clearance is higher for an elastic sample – elasticity promotes energy transfer while viscosity hinders the cilia movement. On the other hand, the cough-clearance is related

to the viscosity – viscous samples move as a whole (intact) while elasticity produces a recoil of the sputum. A healthy sputum will have a balance in the viscoelastic properties which will allow for clearance, mainly by mucociliary [61]. A similar mechanism is believed to happen for the clearance of biofilms. Understanding the physical and mechanical properties of mucus and biofilms is essential to understand the ability to physically disrupt them [65], and rheometry offers a way to study this problem [61].

Sodium alginate rheology

Alginate is a natural anionic polysaccharide usually extracted from brown algae (seaweeds) to be sold commercially, but it is produced by different microorganisms, such as *P. aeruginosa*. It is used in multiple fields, such as biomedical, food industries, pharmaceutical, and others, due to its biocompatibility and ability of gelling. Its molecule is composed of β-D-mannuronate (M) and α-L-guluronate (G) with a 1→4 link (figure 1.8). The exact composition depends on the source of the polymer (different species of seaweeds), but it is usually quite heterogenous and polydisperse. This polysaccharide can be thought of as an unbranched block copolymer with different ratios of M, G and MG blocks [66].

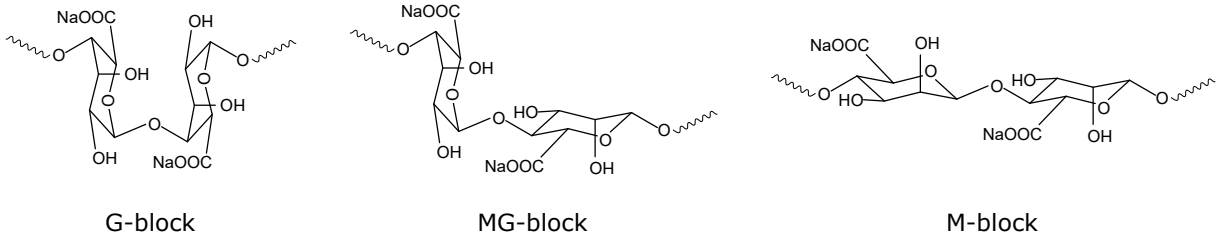


Figure 1.8: Chemical structure of alginate.

Because of the presence of carboxylic acid groups, the polymer's surface is negatively charged and is usually sold commercially as sodium alginate, the water-soluble form. Due to the highly negative surface charge, in a charge-free aqueous environment, the chain behaves like a rigid rod. The lack of intermolecular interaction due to electrostatic repulsion leads to a solution of low viscosity. In the presence of monovalent cations (such as Na^+), the charge screening results in a flexible chain (formation of coils) as if it was a neutral polymer in a good solvent. The higher the ionic strength, the higher the screening, the more flexible the chains and the lower the viscosity of the medium. An elevated concentration of polymer increases the entanglement and, consequently, the viscosity of the solution, resulting in shear-thinning

behaviour. Still, the loss modulus is usually bigger than the storage modulus [67]. On the other hand, in the presence of divalent cations, especially calcium, alginate forms a non-water-soluble strong gel, due to the cross-links. These ions bond more with G blocks than M, consequently affecting the kind of gel obtained – a G-rich sample will result in harder and more brittle gels whereas M-rich samples will lead to softer and more flexible gels [68]. It is known that for sodium alginate, pH, ionic strength, the type of cation, and polymer concentration are important for rheological behaviour [66].

1.3.2 Thesis outline

The main goal of this thesis was to study the phase behaviour of tactoids formed by Pf4 viruses and sodium alginate and to also investigate the role of different impurities. To begin, in chapter 2 we present the experimental methods to isolate and purify Pf4 and to produce the impurities (grow bacteria and synthesize colloidal rods). We also show how the tactoids were prepared and describe the imaging system used. We end this chapter by presenting the background for the main techniques used in this thesis.

Chapter 3 focuses on the synthesis of silica rods, first, with bent-core particles, which potentially could be used to study the behaviour of liquid crystal phases. Then we explore the synthesis and surface modification of spherocylindrical particles used with the tactoids later (chapter 5). In chapter 4 we present the phase behaviour of tactoids by looking at the growth kinetics and then at the size relationship with the concentrations of the components used. Afterwards, we study the phase diagram experimentally and theoretically.

Chapter 5 is the one we explore the configurations formed due to the presence of impurities in the medium with tactoids. We first look at states formed using bacteria and synthetic rods and analyse the distribution of frequencies. We then evaluate the relationship of different configurations with the geometry of the rods using the dimensions of synthetic ones, and the surface properties using the modified ones. Finally, we look at two theories (elastic energy and free boundary problem) to shed some light on the observed phenomena and the effect of quasi-2D confinement. In chapter 6, we look at the rheological properties of the tactoids by focusing on the changes in the polymer solution when tactoids are formed, and, finally, we conclude the thesis in chapter 7.

Chapter 2

Theoretical background and experimental methods

Abstract

In this chapter, we outline the Pf4 production and synthesis of the rods used as well as the bacteria culture. We describe the procedure for tactoid formation and imaging. A brief explanation of microscopy with a focus on confocal and electron microscopy is given since these are the two main tools used to characterize the system studied.

2.1 Materials

The water was obtained from a Millipore System (deionized MiliQ water Direct Q 3UV). The SU-8 50 was obtained from Microchem, cyanine-3 from Lumiprobe, fm4-64 Invitrogen from Thermo Fisher Scientific, and sodium alginate from Scientific Laboratory Supplies. All the other reagents were from Sigma Aldrich.

2.2 Experimental methods

2.2.1 Pf4 isolation and purification

The Pf4 virus was isolated, purified, labelled, and given to us by Dr Abul Tarafder as previously described [51]. In summary, biofilms of the *P. aeruginosa* were grown in a Luria-Bertani (LB) broth at 37 °C until small colony variants were observed. The solution was centrifuged and the supernatant was filtered to eliminate all residual bacteria. The Pf4 phage was then precipitated with polyethene glycol (PEG), resuspended in Phosphate-buffered saline (PBS) and dialysed. The Pf4 was further amplified by incubating with a PAO1 culture again overnight before the PBS was collected and the whole precipitation and purification steps were repeated. The final concentration of the sample was determined using Nanodrop (ThermoScientific).

The virus that was going to be labelled was dialysed in 10 mM sodium carbonate buffer pH 9.2, and 1 mL of the phage (5mg/mL) was mixed with 100 μg A488 dye for 1 hour at room temperature in the dark with agitation. To separate the labelled virus from the free dye, the sample was passed through desalting columns, and the final concentration was obtained using a Nanodrop.

The Pf4 produced in this manner, results in the formation of a native phage and a "ghost" filament (without DNA). They were characterized using cryo-TEM and described in the literature [51]. We present the size distribution for these filaments, reproduced from [51]. The polydispersity has an effect in the phase behaviour of these filaments, as discussed in section 1.2.

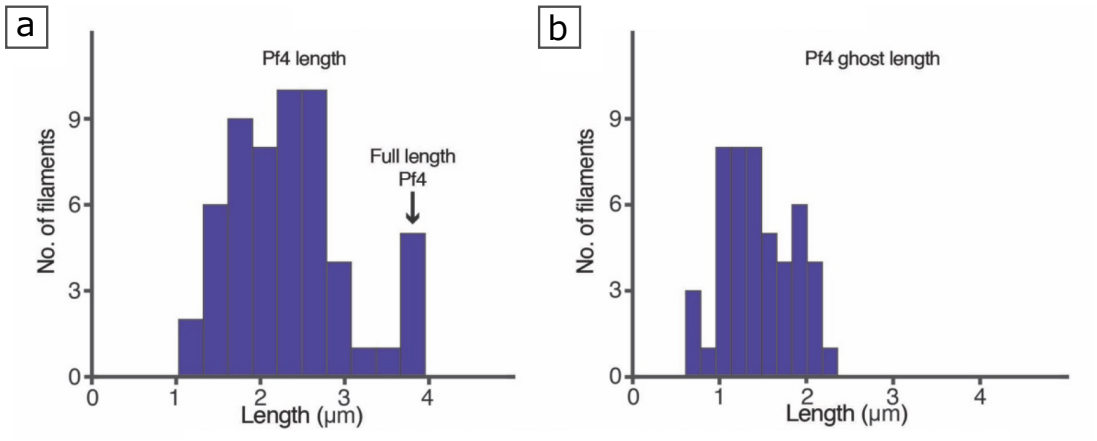


Figure 2.1: Length distribution obtained for (a) native and (b) ghost Pf4 filaments, using cryo-TEM. The full-length Pf4 with intact DNA is indicated by the arrow. Reproduced from [51].

2.2.2 Synthesis of SU8 rods

SU8 rods were synthesized as explained in [69] by another member of the group, Dr Iago Grobas. Briefly, 100 mg of SU8 50 was mixed with 1 mg of the dye Cyanine 3 (Cy3). The SU8 was added to 110 mL of glycerol while being stirred by an impeller at 1800 rpm and remained for 10 min. Then, the solution was passed to a 500 mL beaker to be sonicated at 320 W and 37 kHz for 30 min. After, we transferred the solution to a bottle which was exposed to UV light for 30 min. To wash out the glycerol, water with 0.5 % pluronic was added to reach a final solution of 50 % glycerol. This was transferred to a 50 mL falcon tube which was then centrifuged at 4000 rpm for 1 h. The supernatant was discarded and 10 mL of a solution of 0.5 % pluronic in DI water was added to the pellet, vortexed and finally sonicated for 10 min to destroy the possible aggregates of rods that could be formed during centrifugation.

Before mixing the rods with Pf4, the pluronic needed to be washed out. To do so, 1 mL of this solution was transferred to a 1.5 mL Eppendorf tube and then centrifuged at 3000 g for 40 min. The supernatant was discarded and PBS was added. This process was repeated at least 3 more times so the pluronic was completely washed out of the sample.

2.2.3 Bacteria growth and staining

The bacteria growth and staining were done by Dr Iago Grobas. Glycerol stock of *B. subtilis* NCIB3610 wild-type strain (WT) and *E. coli* K-12 were streaked on a lysogeny-broth (LB)

1.5 % agar plate and grown overnight at 37 °C. A single colony was picked from these plates and cultured in 1 mL of liquid LB for 6 h at 37 °C with aeration at 150 rpm. To visualize the bacteria with fluorescent microscopy, 4 μL of this culture was mixed with the membrane dye fm4-64 at a final concentration of 1 μg/mL.

2.2.4 Tactoid formation

In our experiments, tactoids were obtained by mixing sodium alginate with Pf4 phage. The phage was isolated and purified as described in 2.2.1. A stock solution of sodium alginate 30 mg/mL was prepared every 2 to 3 months by dissolving the powder in PBS. The solution was vortexed for a couple of hours and ultrasound was not used as this can change the characteristics (including viscosity) of the solution [70]. The bubbles were removed by centrifuging or letting the solution rest undisturbed overnight. Any other concentration necessary was prepared by dilution.

Sodium alginate was used since it is the main biopolymer found in the biofilm of *P. aeruginosa* [71]. Other papers have used a mixture of viruses and polymers such as Polyethylene glycol (PEO) [48, 72] and dextran [46, 49]. The main important difference is that these are neutral polymers while sodium alginate is a polyelectrolyte, so charge plays an important role in the physical-chemical properties.

PBS was chosen as the solvent for a similar reason since this buffer is nontoxic, isotonic and with an ion concentration that matches the ones of the human body. It also allows keeping the pH constant, usually at 7.4, a value also similar to the physiological one. It is composed only of monovalent cations, which is important in our application since divalent cations can result in cross-linked sodium alginate, forming a gel and significantly altering the system.

The size of the tactoids depends highly on the concentration of the biopolymer and on the time after preparation. Because of that, different concentrations and times were used, allowing multiple sizes to be obtained. Once the sample had equilibrated, the system was imaged using a Zeiss LSM Exciter 5 (Confocal Laser Scanning Microscope) with a 63x objective.

For the 3D experiments, both solutions were added to an Eppendorf tube and mixed in a vortex mixer for 5 min. Since the amount of liquid was small, the speed was carefully chosen to make sure the solution would mix on the bottom of the tube and not flow up the walls

forming small droplets. The sample was then inserted in a square capillary (0.8 mm wide and 0.16mm wall thickness from CM Scientific) and blown to the middle using compressed air. The capillary was closed and glued to a microscope glass slide with epoxy glue. The samples were left equilibrating before being imaged.

A similar procedure was followed for the quasi-2D experiments, but after vortexing the mixture, the sample was left equilibrating in the vial. After which, an aliquot was put in an agar pad and covered with a glass slide (quasi-2D system). A cover was added to avoid water evaporation from the agar. In the experiments involving the impurities, for both 3D and 2D, the solution containing the rods in PBS was diluted in sodium alginate, before being mixed with the phage.

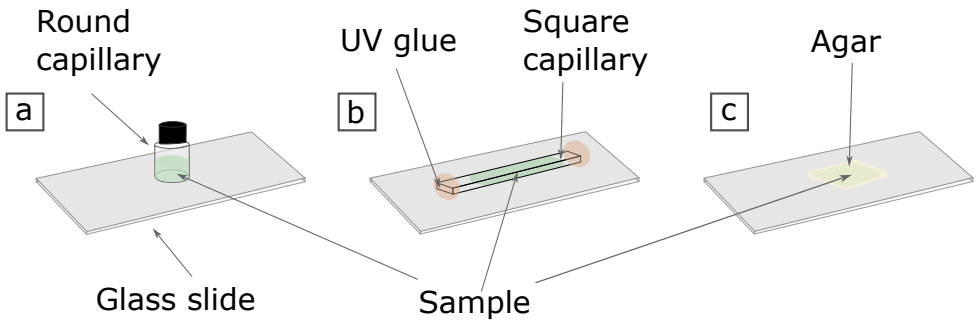


Figure 2.2: Imaging cells used in the experiments: (a) cell for phase diagram, (b) square capillary, and (c) quasi-2D set up.

For the phase diagram, a small capillary (2.5 mm diameter and 1 cm length) was glued with a 61 Noran UV glue to a glass coverslip on one side and PTFE tape was added around its edge until it could be securely closed with a screw thread lid. This allowed us to dilute the sample and guarantee very little evaporation. Because the initial concentrations were high, we decided to use a mixture of labelled and unlabelled phage, especially to avoid saturating the detector. A ratio of 1:200 (labelled:unlabelled) was chosen. For the first point, sodium alginate, Pf4 and PBS were added to the cell, closed and vortexed for 5 min. The mixture was left resting to form the tactoids for 24 h in the fridge. The sample was then imaged and if there were tactoids present it was diluted to the next point. The procedure was repeated until we obtained the isotropic phase.

The cell was weighed with the addition of each component, and after imaging to guarantee there was no evaporation and the right values were being used. Four different dilution lines were made, and the points followed are shown in figure 2.2. Line 4 proved to be challenging because of the amount of sample used. The volume of buffer used to dilute the sample was so small that

was in the range of error of the analytical balance. Because of that, this line was obtained by preparing each point individually in a capillary.

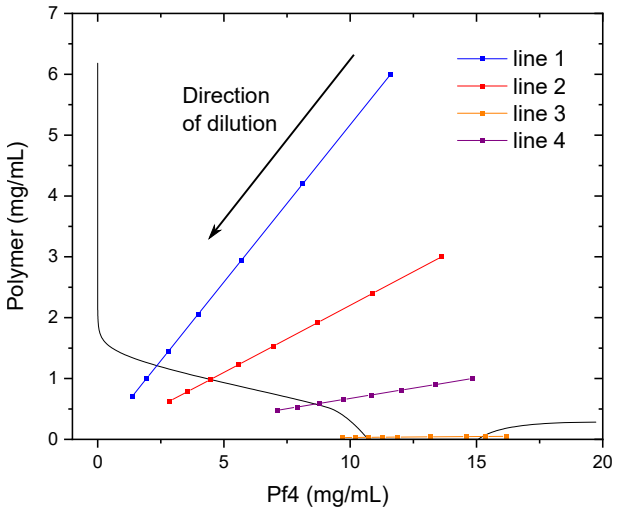


Figure 2.3: Planned dilution lines for the experimental phase diagram.

For the size measurement of the tactoids, a code developed in Mathematica by Olivia Shiels (former part II of the group) was used [25]. In summary, the z-stack was assembled, the 3D image was binarized and small and border components were deleted. The morphological components (each tactoid) were identified and made into a region. The centre of mass was obtained, and the major axis was determined with the two points farthest from the centre. The minor axis was the one perpendicular to the major, going from the boundaries of the region and through the centre of mass.

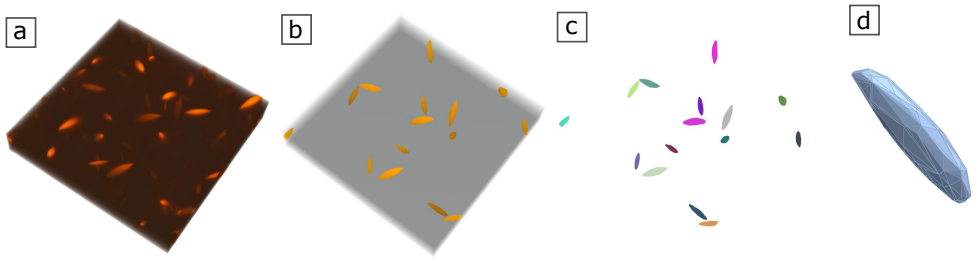


Figure 2.4: Example of the images obtained to measure the size of tactoids starting with the (a) original image, then (b) after excluding small and border components, (c) masked image and finally obtaining the (d) tactoid as a bounded region.

2.3 Theoretical background of experimental methods

2.3.1 Microscopy

The ability to see and distinguish an object is referred to as optical resolution. Objects that are smaller than the resolution of the eye, and thus, can not be seen by the naked eye are studied using microscopes. Different techniques are used, usually divided into optical (or light), electron and probe microscopy. The images are formed due to the interaction of a beam of light, or electron, or a probe, respectively. The different techniques allow for different sizes to be observed [73]. In this thesis, confocal microscopy was the one mainly used, which is a branch of optical microscopy. Electron microscopy was also used in the synthesis of particles. So, a summary of how these two techniques work will be further explained here.

Confocal

Confocal microscopy can be thought of, in a simplified manner, as a fluorescent microscope that can obtain images in 3D. The name originates from the conjugation between the focus point illumination of the specimen and the detection of the signal due to the presence of a pinhole. The ability to remove the out-of-focus light and obtain 3D images (z stacks) can be seen as the main advantage of confocal microscopy. Furthermore, when compared with standard transmission light microscopy, there is a slight improvement in resolution and a significant one in contrast and signal-to-noise ratio.

This can be understood by comparing the point-spread functions (PSF), which describes the diffraction pattern of the emitted light (with wavelength λ) after passing through a lens with numerical aperture (NA). At the point of zero intensity for the PSF, the pattern formed is called the Airy Disk and it determines the limiting performance of the lens - two points are resolved when the Airy patterns are distinguishable. The resolution limit is then defined according to Abbe's Law:

$$d = \frac{\lambda}{2\,NA} \tag{2.1}$$

This means the microscope cannot resolve two points that are closer than a distance d. To increase the resolution, it is necessary to use shorter wavelengths or a lens with higher NA or

change the medium to one with a higher refractive index. For confocal, the width of the curves is smaller and the outer maximum lower than for light microscopy (figure 2.5). As a result, the contrast is greater. Since the resolution is determined by the ability to distinguish between two points, the greater drop for confocal allows two points closer to be distinguished, so the resolution is higher.

Usually, a laser source is used since it results in a greater signal due to its power, but the system does work with other light sources. The beam passes through a filter and is focused on the sample by an objective lens and a dichroic mirror. After interacting with the sample, the excited light, and the emitted photons are focused on the detector by the same mirror and objective. The pinhole, placed in the light path at the back focal point, guarantees that the light coming or going outside the focal plane is blocked. Thus, the sample is only illuminated and light is only obtained from a single spot. Each 2D image is obtained point by point with two moving mirrors changing the point imaged (xy plane). By changing the focal depth, 3D images can be obtained. A schematic of the set-up is presented in figure 2.5.

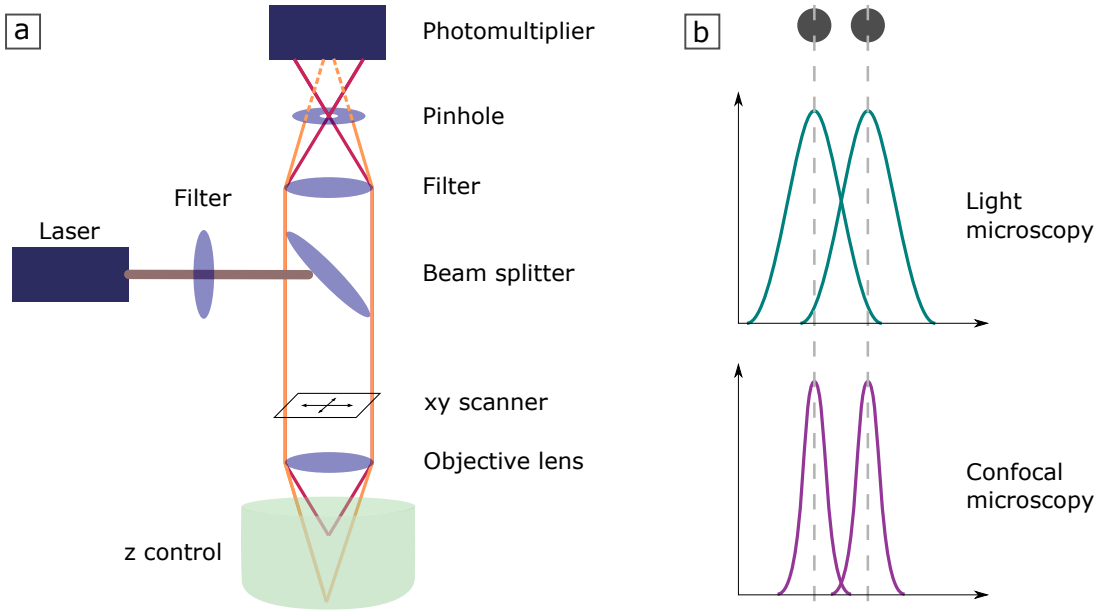


Figure 2.5: (a) Schematics of a laser scanning confocal microscope, and (b) comparison of the point-spread functions (PSF) for optical and confocal microscope.

The most commonly used detector is a photo-multiplier tube (PMT), in which photons of all wavelengths are collected and recorded. The emitted photons are separated using a dichroic mirror and long-pass filter in front of the detector. Most laser scanning confocal microscopes have multiple PMT and in combination with the filters, different wavelengths can be redirected

and it is possible to assign specific wavelengths to the detected photons.

One of the challenges when imaging is finding the conditions that result in a balance between image quality and species damage. A long contact time or high laser intensity with the species will increase the signal but will cause some damage to the species (e.g. fluorophore quenching, heating of sample). Alterations in the pinhole do not affect the sample but have an impact on the signal/noise ratio and the resolution of the image. So, it is important to understand the multiple effects of changing each parameter to obtain a reliable image.

Electron microscopy

The possible resolution obtained with light microscopy is limited due to diffraction. Using electrons as a source, allows much smaller samples to be imaged and higher resolution to be obtained. The interaction of the electron beam will depend on the energy of the beam and different kinds of electrons will be expelled. Having the appropriate detectors allows multiple pieces of information about the sample to be obtained. The lowest energy ones, secondary electrons, are used to image the morphology of samples, while backscattered electrons also give some information on composition due to the further depth of interaction. By having an X-ray detector, detailed composition information can be determined, and with transmission electron microscopy, diffraction patterns can also be obtained. The overall volume of interactions and possibly released electrons are presented in figure 2.6

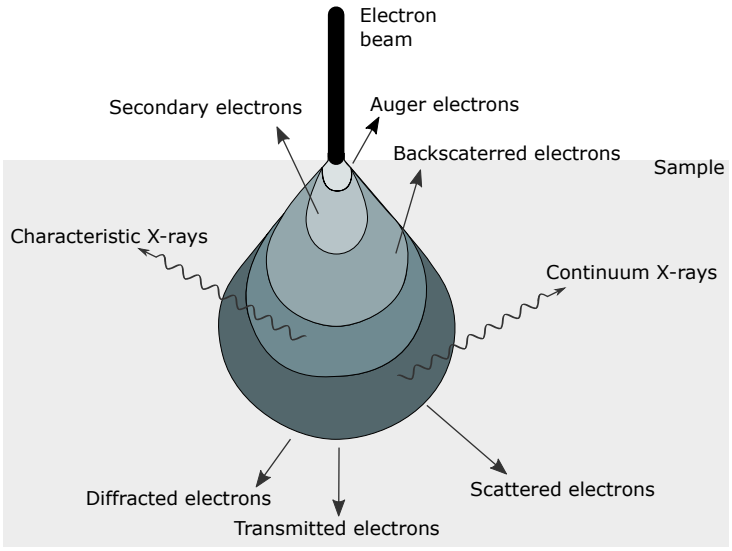


Figure 2.6: Schematic representation of the volume of interaction when the electron beam interacts with the sample and the main electrons emitted.

The setup is quite similar to the ones observed for optical microscopy. A beam of electrons is focused by lenses on the sample. The difference in the position of the detector and, consequently, the maximum thickness of the sample leads to the two EM modes: scanning (SEM) and transmission (TEM). For SEM, the detector is upwards, and there is no limitation in thickness, but only the outer layers of the specimen are seen. For TEM, the detector is below the sample, so they need to be thin for the bean to go through the entire sample (figure 2.7). This explains why an SEM image seems to be in 3D while a TEM one appears to be in 2D.

Especially for SEM, the beam source is quite important in defining the resolution obtained. Thermionic (tungsten filaments) is the one most commonly used, while field emission is normally used when higher resolution is necessary. The resolution is associated with the beam diameter while the current density is connected with the intensity of the emitted signal. For tungsten, the beam diameter is 9 nm while the brightness is $10^5 A/cm^2 sr$, while for field emission they are 1 nm and $10^8 A/cm^2 sr$, respectively, where sr refers to steradian. Because of this, field emission produces samples with higher resolution and it is possible to use beams with lower energy.

For the best resolution possible, electron microscopy is done under vacuum. This avoids the interaction of the beam with the gas before getting in contact with the specimen. Vacuum is also necessary to preserve the filaments, especially for field emission. As a result, only dried samples can be imaged. Cryo systems present a solution to this problem, but sample preparation is complicated to avoid artefacts from freezing. The total cost of the instrument and maintenance is another disadvantage of electron microscopy.

Since the beam is composed of electrons, non-conducting samples will have a surface negatively charged, the electrons will start being deviated and the final image will be distorted. So non-conducting samples are usually coated with a thin layer of conducting metals, such as gold, gold-palladium, platinum, tungsten or carbon, in a process called sputter coating. The main problem with this is the possible loss of details (especially in high resolution when the coating is visible) and the interference of other signals (e.g. when trying to determine sample composition). An alternative, to avoid coating and possible sample degradation due to heat is to use low voltage.

In this thesis, we used two scanning electron microscopes, a JEOL JSM 6010LV and a Zeiss sigma 300 with a field emission gun, and one transmission electron microscope, an FEI Tecnai T12.

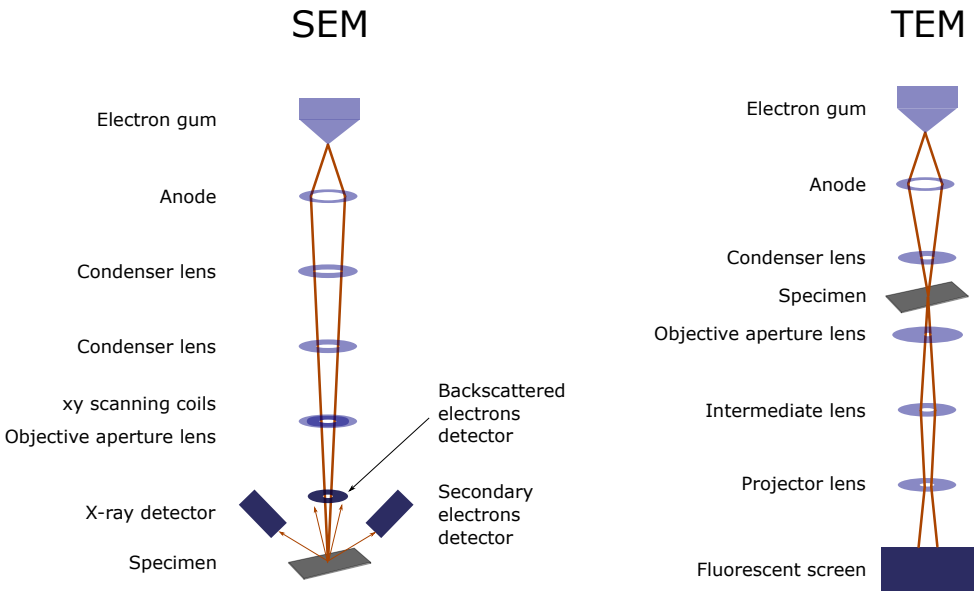


Figure 2.7: Schematic representation of a scanning and transmission electron microscope.

Acknowledgments

We would like to thank Dr Iago Grobas for preparing the SU8 rods and bacteria and helping with part of the experiments involving the tactoids and rods, and Dr Abul Tarafder for the preparation of the Pf4.

Chapter 3

Synthesis of silica rods

Abstract

In this chapter, we explore the synthesis of silica particles, first by focusing on spherocylindrical rods and then on bent-core ones. We aimed to synthesize spherocylindrical rods to mimic a bacteria, and we made these particles with two different sizes within the dimension and zeta potential range described in the literature for *P. aeruginosa*. We modified the rod surface to be positively charged or hydrophobic. These rods will be used as impurities in chapter 5.

We then examined the synthesis of bent-core particles by using a perturbation during the growth of the particle. Initially, a change in surface tension as the rods grew was used as such perturbation. The use of PVP and Span 80 resulted in a change of diameter, while tert-butanol led manly to short rods. Subsequently, we used temperature as perturbation which produced bent-core particles with a broad angle range as described previously in the literature [74]. We investigated the effect of multiple variables to try to decrease the angle distribution. The results showed that ammonia concentration plays an important role, especially to guarantee reproducibility. We then focused on the use of pre-hydrolysed TEOS, investigating the extension of pre-hydrolysis (time of reaction), the proportion of pre-hydrolysed/non-pre-hydrolysed reagent, and the presence of ethanol. We obtained bent rods, but the pre-hydrolysis of TEOS is difficult to characterize, and, consequently, reproduce. The formation of kinks is likely related to the changes in the rate of hydrolysis and condensation caused by the temperature. These rates are highly dependent on the pH and the pre-hydrolysis level of TEOS, so the synthesis proved difficult to reproduce since these two parameters, especially the latter, are difficult to control.

3.1 Introduction

Silica particles have been used for a long time in research and industry due to their properties and versatility. They are employed as adsorbents, in drug delivery, synthesis (catalysis), analytical chemistry (chromatography column), and in multiple other fields [75]. In addition, with easily tunable size and shape, these colloidal particles can be used as model particles [76, 77]. This last application was the main goal in the synthesis of our particles.

Initially, we wanted to use bent-core silica particles as model particles to understand the behaviour of bent-core liquid crystal phases. However, the synthesis of such particles proved to be challenging, so the aim changed to spherocylinder rods mimicking bacteria. In this chapter we will first give a brief introduction on the topics related to the work presented - the sol-gel synthesis (section 3.2.1), the route used for the production of these rods, then, a literature review of the rods' synthesis (section 3.2.2), focusing on the mechanism, and lastly, the theoretical background about surface modification (section 3.2.3). Next, the experimental session is presented in 3.3, followed by the results and discussion. We first describe the synthesis of spherocylindrical silica rods used to mimic bacteria (section 3.4.1) and their surface modification (section 3.4.2). Subsequently, we present the results regarding the attempt to better understand the synthesis of bent silica rods in section 3.4.3. Finally, we conclude the chapter in section 3.5.

3.2 Synthesis background

3.2.1 Sol-Gel route

The sol-gel route is a synthesis that can be summarized as the formation of an initial colloidal suspension (sol) that progresses to form a network of the new solid silica (gel). This synthesis can be made with any alkoxide, being tetraethyl orthosilicate (TEOS) the precursor most commonly used. The reaction starts with hydrolysis followed by condensation. Both steps can happen just in the presence of water, however since it is a slow reaction, it is common to use acid or base catalysis [78]. This synthesis is famously used in a dilute medium to produce silica nanoparticles in the Stöber process [79].

Many parameters affect this synthesis, making it quite sensitive, but also highly tailorable.

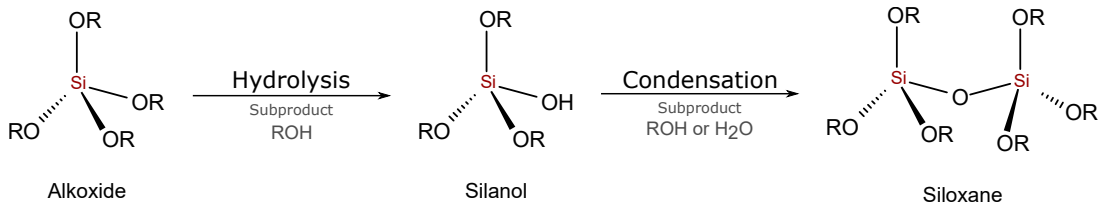


Figure 3.1: Schematic representation of a general sol-gel synthesis – hydrolysis of the precursor (alkoxide), and condensation of the silanol resulting in the final product (siloxane).

The main ones are the type of precursor, the ratio between alkoxide and water (Rw), the type of catalyst used, the type of solvent, the co-solvent (if one is used), the temperature, the relative and absolute concentration of reactants, and the pH [78]. Many of them have been explored in the literature [80, 81], including for the synthesis of silica rods [82–84].

Hydrolysis and condensation have their reaction kinetics affected by the presence of the catalysts. Both steps have an intermediate, positively and negatively charged, for the acid and basic catalysis, respectively. As a result, different rates of each one happen at different values of pH and distinct degrees of networks are obtained as summarized in figure 3.2. For acid catalysis, the reaction rate decreases when processing due to the presence of more hydroxyl groups and the opposite is observed for the base. As a result, with basic catalysis, the fastest condensation rates are seen for fully hydrolysed species, and a highly branched and cross-linked substance is obtained, usually resulting in particles. For acid catalysis, this is not observed and a weakly branched gel is the product of the reaction [78, 79].

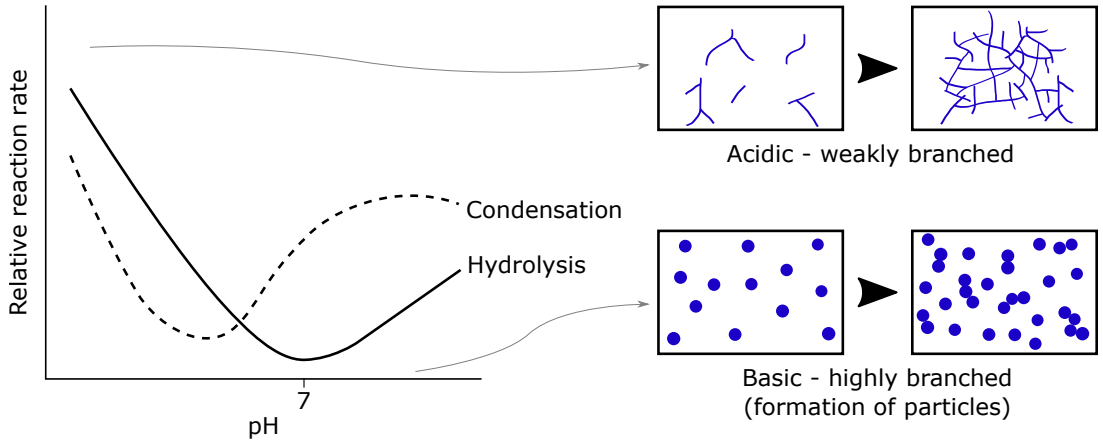


Figure 3.2: Representation of the condensation and hydrolysis reaction rates with pH (adapted from [85]) and of the structures formed in an acidic or alkaline environment.

3.2.2 Silica rods synthesis

Zhang *et al.* [86] have developed a method for synthesizing silica rods in which the authors believed the presence of gold nanoparticles was responsible for the formation of the different morphologies they obtained. In their technique, an emulsion of water-PVP-pentanol was made and the nanoparticles were deemed responsible for the aggregation of the structures formed. Playing with the interaction between gold and PVP was hypothesized as the variable responsible for the different shapes synthesized. They proposed the growth of the rods followed a solution-solution-solid mechanism similar to the one observed for the formation of nanowires with the vapour-solution-solid mechanism.

Later Kuijk *et al.* [76] showed that the component responsible for the formation of the rods was sodium citrate, which was used to stabilize the gold nanoparticles used by Zhang *et al.* [86]. Since then, this synthesis became highly studied and many variables were explored. The most important ones seem to be the concentration of reagents, total volume, mixing, temperature, and pH. Over the years different authors exploited different conditions in an attempt to understand the mechanism and the effect of each variable in the final morphology obtained [82–84, 87–89].

Kuijk *et al.* [76] proposed that since TEOS solubilizes in pentanol, but not in the water, it would initially be in the organic phase. When in contact with the aqueous droplet, containing the catalyst, this molecule would start hydrolysing to a form that is soluble in water. Consequently, the supply of this reagent is unilateral, and the condensation happens on the formed nucleus in one part of the droplet, so the rod grows anisotropically. They showed TEM images of the synthesis as progressed and a schematic can be seen in figure 3.3.

Two papers are of special interest to the work presented in this chapter. By changing the temperature during the rods' growth Datskos et al [88] showed that higher temperatures resulted in smaller droplets, and consequently, thinner rods. This process is reversible, meaning the droplet can also get bigger when the temperature is lowered, thus a rod can be produced having multiple diameters. A different result was obtained by Yang *et al.* [74] following a similar method, but with a smaller amount of ammonium hydroxide. The diameter change was also observed, but there was a shift in the growth direction - they obtained bent-core particles.

One clear morphological difference between the results presented by both papers is the presence of a small "head" (matchstick-like rods) in the rods that bent. This is usually seen

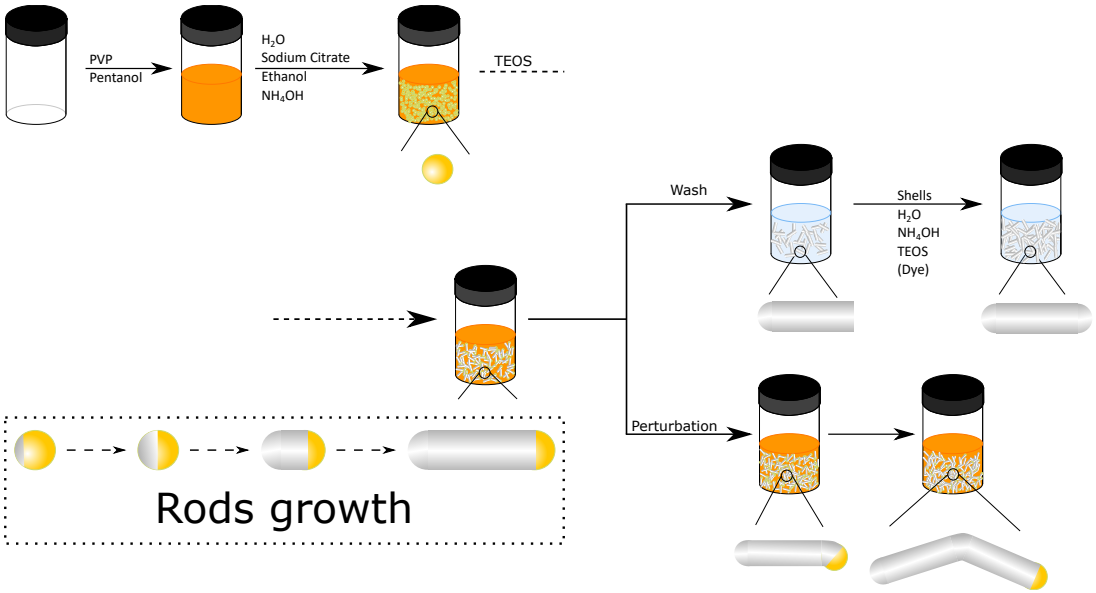


Figure 3.3: Schematic representation of the silica rods growth. In the dotted box, it is possible to see the formation of the silica inside the emulsion droplet. To produce spherocylindrical or bent rods, further steps can be taken.

when the TEOS used in the synthesis has gone through an initial pre-hydrolysis step, resulting in a faster initial condensation, and this matchstick-like structure. Initial hydrolysis was not described in the experiment of Yang *et al.*, and as even indicated by the authors, the reagent used was likely hydrolysed over time [74]. Even though the TEOS reaction rates are slow, reagents that have been left open for too long, out of the desiccator, or opened too often, can start hydrolysing with the humidity from the atmosphere [78]. This difference is a good indicator that a pre-hydrolysed TEOS is necessary for rod bending.

Hagemans *et al.* [87] showed that the addition of tetramethyl orthosilicate (TMOS), which has different hydrolysis and condensation rates than TEOS, and pre-hydrolysed TEOS resulted in bent-core rods. This indicates that changes in the individual or combined hydrolysis and condensation rates are behind the difference between the rods bending or not. It is difficult to find a complete explanation for these observations since the mechanism of the formation of the rod is still not fully understood. In section 3.4.3 we will present our results related to this topic.

3.2.3 Surface modification

Silica particles are negatively charged and hydrophilic due to the presence of hydroxyl groups on their surface. These groups allow for the tailorable change and functionalisation of the surface,

part of the versatility of this material. The most common way to change these surfaces is by using silanes, which can change the charge, wettability, and adhesion, or act as a coupling agent. These silanes react by a general mechanism shown in figure 3.4, with a hydrolysis and a condensation step, even though not all the stages of this synthesis are known and understood. The formation of covalent bonds guarantees high stability [90].

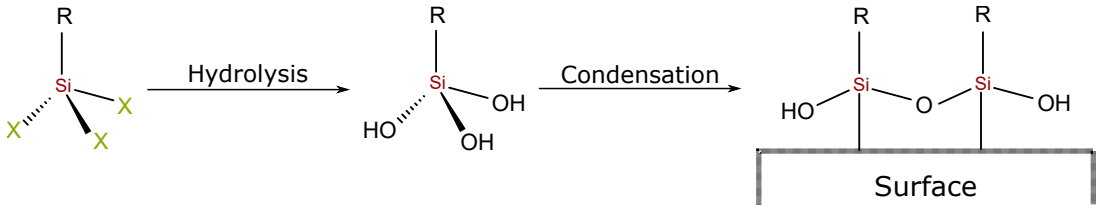


Figure 3.4: Schematic representation of a general surface modification with silanes.

One of the most commonly used silanes is 3-aminopropyltriethoxysilane (APTS). Once hydrolysed it forms a film with aminated silane. On its own, it changes the charge of the particle and may change the wettability, and surface adhesion [91]. It can also act as a coupling agent allowing other compounds to be attached to the surface terminal amines such as dyes [92], and proteins [93]. Amine groups can self-catalyse, so depending on the amount of water present in the system, this reaction can happen in the solution of the reagent itself (being then important to check if the reagent used is not already polymerized) [91].

To make the silica surface more hydrophobic, one or more silyl groups are introduced, a process called silylation. Two of the most commonly used silanes for this purpose are Hexamethyldisilazane (HMDS) and Trimethylsilyl chloride (TMSCl). HMDS hydrolyses and condensates at the surface, releasing ammonia and leaving methyl silanol exposed, responsible for the new wettability of the surface. TMSCl goes through a similar reaction, releasing Cl_2 and also leaving a methyl silanol exposed. All silylation reactions involve several variables and are usually done in apolar dry solvent to guarantee the reaction will happen at the surface [94, 95].

3.3 Experimental methods

3.3.1 Materials

The water was obtained from a Millipore System (deionized MiliQ water Direct Q 3UV). For the synthesis of the silica rods, pentanol and sodium hydroxide were purchased from Alfa Aesar.

All other reagents were from Sigma Aldrich and used without further purification.

The TEOS was always stored on the desiccator, and for most synthesis, new bottles of the reagent were purchased and divided into smaller vials, stored under N_2 and in the desiccator. To overcome problems of reproducibility with ammonium hydroxide, the latest syntheses were done with a new bottle of ammonium hydroxide, and its content was distributed in small vials that were very well closed and stored in the fridge. For each test, a different vial was used and the initial pH was checked.

Regarding the surface modification, toluene was obtained from Fluska (puris, molecular sieve, $H_2O < 0.005$ %) already dried and kept in the molecular sieve. Chlorotrimethylsilane was from Alfa Aesar (98 %) and all other reagents were from Sigma Aldrich and used without further purification.

3.3.2 Straight rods synthesis

The synthesis of straight rods was based on Kuijk *et al.* [76] Briefly, 30 g of PVP 40 kDa were mixed with 300 mL of Pentanol (by shaking and using a vortex mixer and then an ultrasonic bath). When the mixture was homogeneous (no hairline observed), 8.1 mL of water, 1.8 mL of sodium citrate 0.18M, 27 mL ethanol and 4 mL ammonium hydroxide 28 %wt were added. The mixture was vortexed in a high-shear mixer (IKA T 25 ULTRA TURRAX) for 1 minute and then left standing for 60 min (to allow all the bubbles to leave the system and the emulsion to stabilize). Then 1.8 mL of TEOS was added and the mixture was quickly vortexed for 10 sec. The system was left reacting undisturbed overnight and washed the next day.

When we mention the rods were washed, the same procedure was followed: centrifuged for 70 min at 3000 rpm (1811g), then washed twice with ethanol, twice with water and then twice with ethanol at 2500 rpm for 25 min (1258g).

Changing the proportion of the reagents (PVP, Pentanol, water, sodium citrate, ethanol, ammonium hydroxide and TEOS) results in rods of different sizes or different shapes (e.g. curly ones). The synthesis described was the initial one to produce the thick spherocylindrical rods. The amounts for this synthesis and the thin one are shown in table 3.1. The rest of the procedure was exactly the same.

3.3.3 Spherocylindrical rods

The growth of silica shells results in spherocylindrical rods, and the protocol used was based on Gao *et al.* [96]. The shells alter the diameter but do not significantly change the length of the rod. For the thick rods, the rods described in 3.3.2 were suspended in 100 mL of ethanol. In a system with a magnetic stirrer, 7 mL of ammonium hydroxide 25 %wt, 9 mL of water and 0.6 mL of TEOS were added. Under stirring the system was left to react overnight, after which the rods were washed and the same procedure was repeated 2 more times (resulting in 3 layers).

To add a dyed shell, Rhodamine B isothiocyanate (RITC) dye was chosen (considering the Alexa Fluor 488 dye used for the virus). For that, 35 μL of 3-aminopropyltriethoxysilane (APTS) was added to 5 mL of ethanol under stirring and then 35.5 mg of the dye was quickly added to the mixture. This reaction was left overnight. Then the cleaned rods were dispersed in 100 mL of ethanol and 7 mL of ammonium hydroxide 25 %wt, 5 mL of water, 1 mL of TEOS and 5 mL of the RTIC/ethanol mixture were added. The system was left to react overnight under stirring, after which the rods were washed as previously described but with ethanol: ammonium hydroxide 95:5 instead of pure ethanol, otherwise, the rods would agglomerate. For a final layer, the rods were suspended in 100 mL of ethanol: ammonium hydroxide 95:5 and the procedure done for the initial layers was repeated. Having this extra layer guarantees that the rods will be stable at pH 7. The thin rods had only two layers (the first dyed and the second not) and the amounts used are presented in the table 3.1.

3.3.4 Bent silica rods

The synthesis of bent silica rods was evaluated by using surface tension change and temperature as a perturbation of the system during the growth of the rods. The synthesis was done in a 10 mL vial where 1 g of PVP 40 kDa was mixed with 10 mL of pentanol (by shaking/vortex and then by putting it in the ultrasonic bath). When the mixture was homogeneous (no “hairline” like structures seen), 280 μL of water, 100 μL of sodium citrate 0.18 M, 950 μL Ethanol and 135 μL of ammonium hydroxide 28 wt % were added (in this order). The mixture was vortexed for 1 min and left standing for 5 min. Afterwards, 100 μL of TEOS was added, vortexed for 10 s and the system was left to react undisturbed for 3h at room temperature. Then the mixture was heated to 65 °C for 5 min. To finish the mixture was left to react overnight at room

Table 3.1: Amount reagents synthesis

Rods	PVP (g)	Pentanol (mL)	Water (mL)	Sodium citrate (mL)	Ethanol (mL)	Ammonium hydroxide (mL)	TEOS (uL)	RITC solution (mL)
Thick	30	300	8.1	1.8	27	4	1800	-
Shells	-	-	9	-	-	7	600	-
Died shell	-	-	5	-	-	7	1000	5
Thin	10	100	2.7	0.6	9	1.35	1000	-
Shell	-	-	3	-	-	2.3	150	-
Died shell	-	-	1.7	-	-	3	250	1.5

temperature. The rods were then washed. Changes in surface tension were made by adding the reagent after 3 hours the TEOS had been added. The three tests done were using 5 mL of PVP in ethanol (0.4 g/mL), 2.5 mL of Span 80, or 2.5 mL of tert-butanol. A test to change the hydrolysis/condensation rate was also done by adding 4 or 6 μL of TMOS as perturbations.

For the initial pre-hydrolysis of TEOS, it was tested chloridric acid as the acid catalyst and ammonium hydroxide as the base catalyst. The acid pre-hydrolysis was done with 1:1:0.005 mol TEOS:water:HCl, by first making a 0.001 mol/L HCl solution and then mixing 0.36 g of this solution with 4.16 g of TEOS under stirring, with the reaction being timed as soon as the TEOS was added. When the pre-hydrolysys was performed with ethanol, 1.5 mL of the reagent was added after the aqueous solution. For the basic catalysis, 0.36 g of water were mixed with 0.36 g of base and then with 4.16 g of TEOS. This hydrolysed TEOS was mixed with a non-hydrolysed TEOS by volume percentage, usually 7 % (unless specified otherwise).

3.3.5 Silica rods - Surface Modifications

The silica rods were modified to be positively charged (APTS), or more hydrophobic (HDMS and TMSCl). Surface modifications of silica particles are well-known in the literature. However,

since the synthesis of the silica rods involves a lot of reagents that remain in the particles and their surface (especially PVP), the surface of the rods should be prepared for the reaction. It can either be cleaned with HNO_3 or piranha solution, but these reagents destroy the dye. The growth of shells results in a cleaner surface, so the cleaning was not essential, and the reactions were done with the rods after just being washed with ethanol and dried.

The synthesis with APTS was based on Howarter *et al.* [91]. It was done by resuspending 10 mg of silica rods in 9.5 mL of toluene and adding 0.75 mL of APTS (7.5 %) in a round bottom flask. The system was heated to 75 °C and the reaction was left for 24 h under reflux. Once finished, the particles were washed three times with ethanol at 2500 rpm for 25 min (1258g) and left drying at 75 °C.

The synthesis with Hexamethyldisilazane (HDMS) and Trimethylsilyl chloride (TMSCl) was done following Capel-Sanchez *et al.* [94]. In a round bottom flask, 10 mg of dried silica rods were resuspended in 9 mL of toluene and 1 mL of HDMS or TMSCl was added. The mixture was left reacting for 2h under reflux. The rods were washed three times with ethanol at 2500k rpm for 25 min (1258g) and left overnight at 75 °C to finalize the reaction.

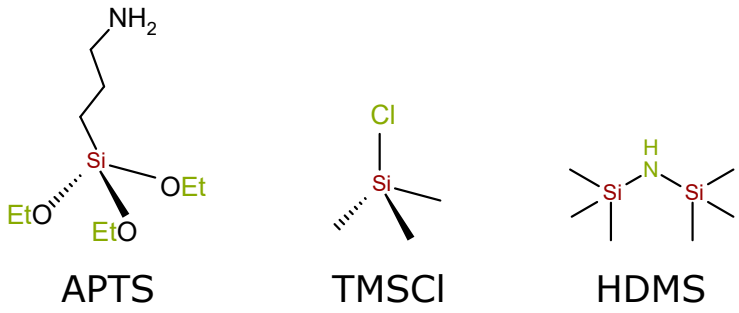


Figure 3.5: Molecular structures of the silanes used - 3-aminopropyltriethoxysilane (APTS), Hexamethyldisilazane (HDMS) and Trimethylsilyl chloride (TMSCl)

3.3.6 Characterization

The rods were characterized by electron microscopy, using a Scanning Electron Microscope JEOL JSM 6010LV (SEM), a Zeiss Sigma 300 Field Emission Gun Scanning Electron Microscope (FE-SEM), and an FEI Tecnai 12 Transmission Electron Microscope (TEM). For the SEM, the sample was suspended in ethanol and a droplet was added to a silica wafer which was glued to a stub with carbon tape. The samples were sputter-coated with gold for 60 sec at 20 mA. The sample for TEM was also suspended in ethanol. The grids were glow discharged and then left

in contact with the droplet for 5 min before being bloated. The size of the rods was determined using the minimum bound rectangle of the OpenCV library in Phyton.

The zeta measurements were done in a Zetasizer nano Z from Malvern. The rods were either suspended in water (0.01mM NaCl) or phosphate-buffered saline (PBS), being the latter the solvent used if not specified. All samples were at 1 mg/mL. For the aqueous sample, an automatic method was used in the software and the cells were filled with a homogeneous sample. For PBS, since it has a high electrolyte concentration, the diffusion barrier method was used to fill the cells, and the measurements were done using monomodal mode with a maximum of 3 repeats for each sample.

3.4 Results and Discussion

3.4.1 Straight Rods

Spherocylindrical rods were synthesized to mimic the shape of bacteria. To do so, we initially synthesized a straight silica rod, which has a bullet shape and grew extra shells. Since the growth of shells changes more the diameter than the length, we chose the thinnest possible rods and made thick and thin ones by changing the number of shells grown. The microscopy images show that we were able to synthesize the bullet shape rods and with the growth of shells produce spherocylindrical rods.

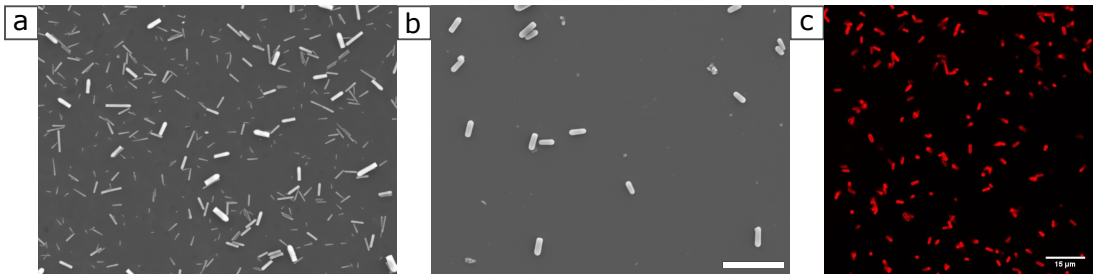


Figure 3.6: (a) SEM image of the initial rod, before the growth of shells and (b) SEM and (c) confocal images of the final rod, after the growth of 4 shells for the thick rods. Both SEM images have the same size and the scale bar is 10 μm.

The size of the rods was determined as described in the 3.3 using the SEM images and the final values (after the shells were grown) for both rods, as well as the zeta potential for the rods in PBS, are presented in the table 3.2. The size and zeta potential of both silica rods are similar to the ones obtained in the literature for *P. aeruginosa*.

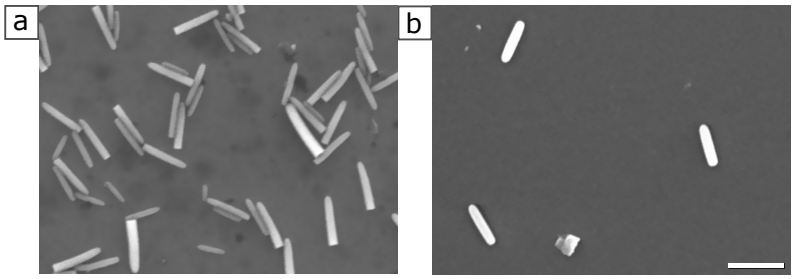


Figure 3.7: SEM image of the (a) initial rod, before the growth of shells and (b) final rod, after the growth of 2 shells for the thin rods. Both images have the same size and the scale bar is 2 μm.

Table 3.2: Size, length diameter, and zeta potential in PBS of the spherocylindrical rods

Rod	Length (μm)	Diameter (μm)	Zeta potential (mV)
Thick	2.43 $\pm$ 0.26	0.98 $\pm$ 0.06	-13.9
Thin	1.67 $\pm$ 0.20	0.41 $\pm$ 0.06	-12.1
P. aeruginosa	1 to 5	0.5 to 1	-7 to -12

We also imaged the rods with FE-SEM since the higher resolution of this technique allowed us to observe the surface of the rods in more detail. As can be seen in figure 3.8, the rods have some defects on the surface, looking like part of spheres attached. This could be the result of the layers growing, with a small droplet condensating at the surface. Even though care has to be taken when looking at high magnification images (especially since the samples were coated with gold and it is possible to see the cracks related to this), it is possible to see some pores, which is common in silica particles produced by the sol-gel method [79].

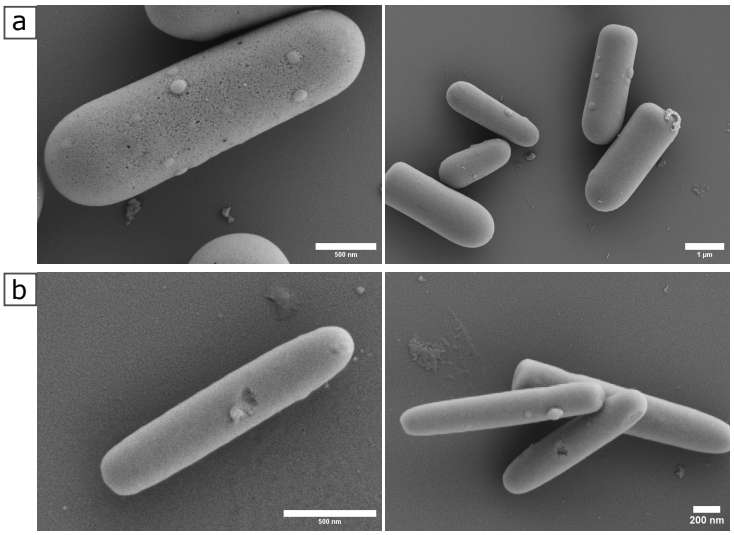


Figure 3.8: FE-SEM images of the (a) thick and (b) thin rods.

3.4.2 Surface modification

In chapter 5 we will discuss the interaction of tactoids and rods. Surface chemistry is one of the factors that explain the anchoring of liquid crystals, so we changed the surface of the rods to be positively charged or hydrophobic. All the surface modifications are dependent on several variables that affect the extension of the surface modification, the thickness and roughness of the new layer, and the conformation of the newly bonded molecule. Temperature, reflux, the concentration of reagents, time of reaction, and curing are some of the most important ones. A new synthesis, equal to the one described for the thick rods was done to evaluate some of these variables before modifying the actual thick rods' surface.

The first modification we did was with 3-aminopropyltriethoxysilane (APTS). This molecule is commonly used to change the surface of silica groups and as it ends in amine groups, being positively charged at pH 7. Since water is needed for the hydrolysis of the molecule, it has been proposed that this happens more effectively when there is sufficient surface water. After the formation of the first hydrolysed layer, there is very little water at the surface and if the concentration of APTS is high, it is more likely that the water will react with a molecule in the bulk instead of further hydrolysing the ones in the surface. As a result, the hydrolysed molecules in bulk will be deposited in the film [91]. Still, a minimum amount of the reagent is necessary to cover the whole particle, and using an optimal concentration leads to a smooth highly positively charged surface [91].

Zeta potential analysis is a reliable technique to evaluate particle charge and allowed us to determine the optimal concentration of APTS used in the synthesis. The zeta potential was obtained in water and PBS to compare since in the first solvent the difference of zeta is higher and easier to see. The concentration that offers the highest zeta potential is between 5 and 10 % (figure 3.9), so 7.5 % was the chosen one. The new zeta potential of the thick rods changed with APTS as can be seen in table 3.3.

Afterwards, we focused on changing the wettability of the particles, modifying them with Hexamethyldisilazane (HDMS) and Trimethylsilyl chloride (TMSCl). Unfortunately, characterizing the wettability of particles is difficult since most techniques to do so require a flat continuous surface. Thus, these modifications were done following the papers referred and qualitative observation of the contact angle was what we considered to evaluate if the surface was

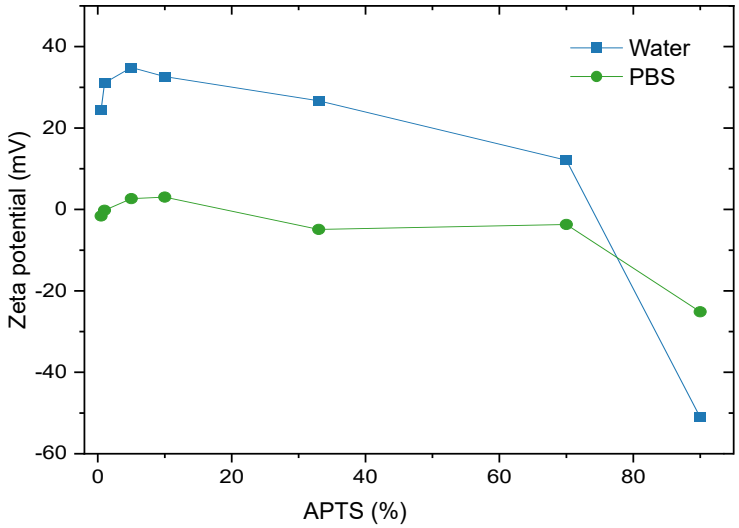


Figure 3.9: Zeta potential in PBS of the silica rods modified by the concentration of APTS used in the synthesis.

modified or not. As can be seen in figure 3.10, the droplet spreads for the pure silica rods, while a full droplet can be seen for the rods modified. Also, when trying to dissolve the particles in water it was possible to see aggregation. So, we can say the particles are hydrophobic, but not by how much.

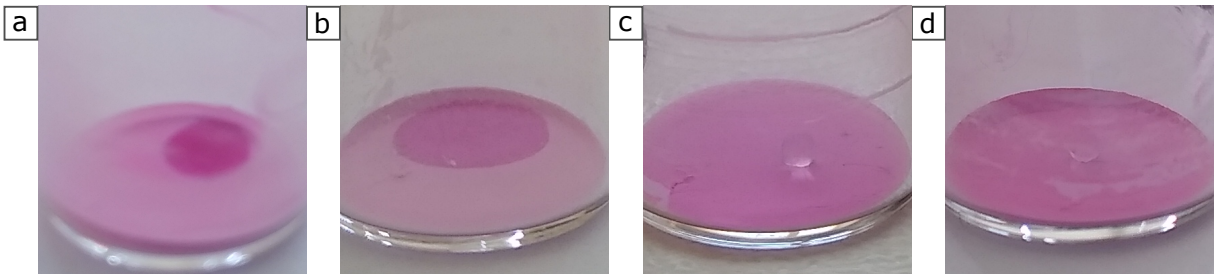


Figure 3.10: Qualitative evaluation of the wettability of the surface-modified rods. Pictures of a 1 μL droplet in dried (a) unmodified and modified silica rods with (b) APTS, (c) HDMS, and (d) TMSCl.

Table 3.3: Zeta potential in PBS of the silica rods modified with APTS, HDMS, and TMSCl.

Rod	Zeta potential (mV)
Thick	-13.9
APTS	10.3
HMDS	-12.90
TMSCl	-0.91

3.4.3 Bent Rods Synthesis

To make bent silica rods, some kind of perturbation is necessary to change the direction of growth. Our first attempt was using a change in surface tension since it was believed this variable allows the rods to grow straight [76]. Later, based on the work of Yang *et al.* [74], we studied how temperature can be used as a perturbation and the effect of TEOS pre-hydrolysis.

Surface Tension as perturbation

The initial surface tension change tests were based on the silica rods' growth mechanism proposed by Kuijk *et al.* [76]. An emulsion of water-in-oil is formed and the rod grows from the aqueous phase caused by the anisotropic supply of reagents. If the local surface tension is constant while the rods are growing, then a straight rod is formed. Thus, our initial approach was to change the surface tension while the rods were growing. Initially, all the different reagents used for the synthesis were tested as such perturbation and possible bending: ethanol, sodium citrate, water and PVP (dissolved in ethanol). The three first did not lead to any significant change in morphology. The addition of PVP resulted in a decrease in the diameter of the rods (figure 3.11). This is compatible with the literature, since a decrease in the droplet diameter with the increase in PVP concentration has been reported, even though it has not been as a perturbation [84]. Murphy *et al.* related this behaviour to the entanglement of the polymer chain - the droplet forming the silica rods is rich in PVP, so the higher the quantity of this polymer, the more entangled it is and the smaller the droplet becomes. It is also interesting to note that at the end, there was the formation of a hollow end in some rods [84].

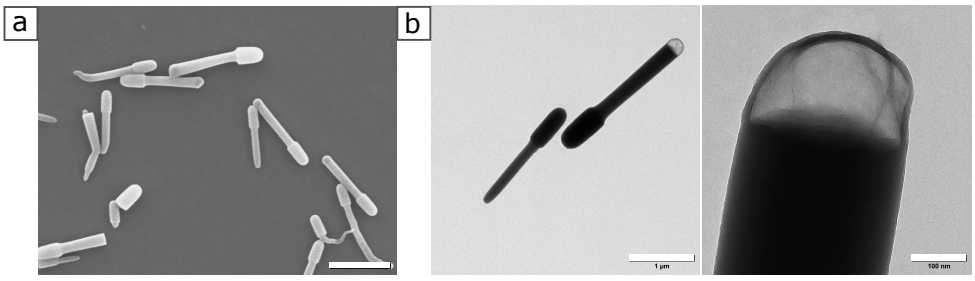


Figure 3.11: (a) SEM (scale bar 2 μm) and (b,c) TEM images of the rods with the addition of PVP in ethanol as perturbation.

Afterwards, a nonionic surfactant, Span 80 was used. In contrast with the PVP, the

addition of Span 80 resulted in a larger diameter of the rods (figure 3.12). This could probably be explained by the surfactant molecules interacting with the aqueous droplet, entering the droplet and increasing its size and/or decreasing the PVP entanglement. Nevertheless, neither of these results led to bent rods.

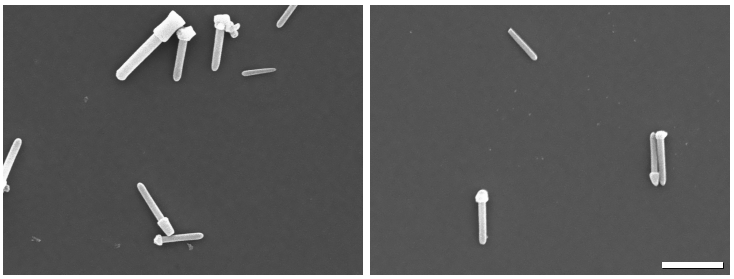


Figure 3.12: SEM images of the rods with the addition of Span 80 as perturbation. Both images are the same size and the scale bar is 2 μm.

Last, we tried the addition of another organic solvent (tert-butanol), based on the change of surface tension [97]. The addition resulted in bent rods as well as in rods with half of the expected size (most common case) as shown in figure 3.13. Probably, the surface change was enough to make the droplet from which the rods were growing unstable, and detach. The bent rods that formed had a broad-angle distribution and the kink where the rods folded had more than one curvature in some cases. Therefore, a new approach to bending the rods was tested (temperature).

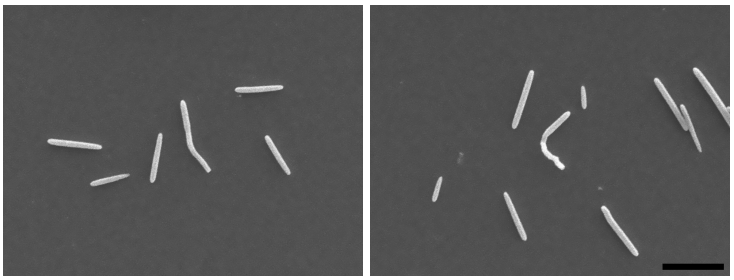


Figure 3.13: SEM images of the rods with the addition of Tert-butanol as perturbation. Both images are the same size and the scale bar is 2 μm.

Temperature as perturbation

The paper by Yang *et al.* [74] describes the synthesis of bent-core colloidal rods using temperature as the perturbation that results in the growth of "the second arm" in a different direction. We were successful in reproducing the synthesis and the results using a temperature of 65 °C, see figure 3.14. However, the angle distribution is quite broad, similar to the one obtained by the

original authors. They found that the higher the temperature, the higher the angle obtained, but also the broader the angle distribution.

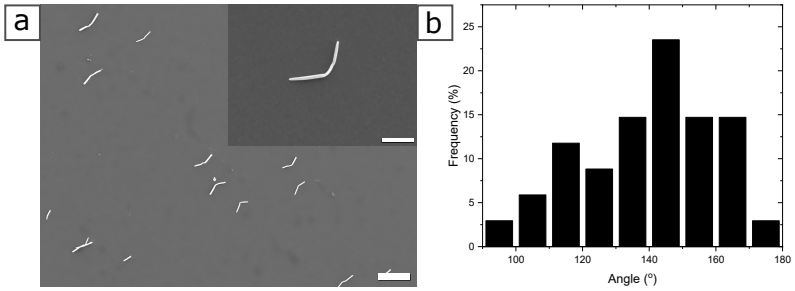


Figure 3.14: (a) SEM images of the rods with temperature (65 °C 5 min) as a perturbation. Scale bars are 10 μmfor the main image and 2 μmfor the inset; (b) distribution of the angle formed by the bent rods. Reproduction of the experimental procedure from Yang *et al.* [74].

The TEOS initially used for the reproduction of Yang's paper was opened for approximately 3 months before the tests began. Even though it had been stored in a desiccator and no "matchstick-like" particles were observed, the reagent could still be partially hydrolysed. When a new reagent was bought, the same procedure did not result in bent rods. Then, any new bottles of TEOS were divided into smaller vials stored in N_2 and desiccator to avoid opening the same bottle many times and, consequently, the hydrolysis of the precursor.

To try controlling this angle distribution, we started evaluating several variables involved in the synthesis with and without pre-hydrolysing the TEOS used. The experiments were done in parallel, but are presented here first without the pre-hydrolysis and after with the pre-hydrolysis. Some images are shown twice to compare conditions, especially for interday cases.

We started by evaluating the amount of each reagent, but except for the base, no significant morphology change was observed. The concentration of ammonium hydroxide (NH_4OH) has been previously reported as being extremely important [76]. As can be found in the manufacturer's product information, ammonium hydroxide is stable at room temperature. However, it is a weak base, which means a large amount of the molecule is found as NH_3. This is a volatile gas that will evaporate if the bottle is left opened or opened multiple times. As a result, the equilibrium will shift to produce more NH_3 and the concentration of NH_4OH will decrease. To minimize this problem the manufacturer recommends the bottle should be stored at 2-8 °C once opened. However, even in this situation, in a synthesis as sensitive as this, storing the reagent in the fridge was still not sufficient as the results presented below will show.

An initial test with a broad range of NH_4OH (10 to 200 uL) was done and the results are shown in figure 3.15. With 10 μL curly rods were obtained. Increasing the amount to 50 μL made the rods less curly, but still not straight. At 100 μL bent rods are seen, even though with smaller angles than before. Increasing further the amount of the base resulted in straight rods, with changes in diameter with temperature.

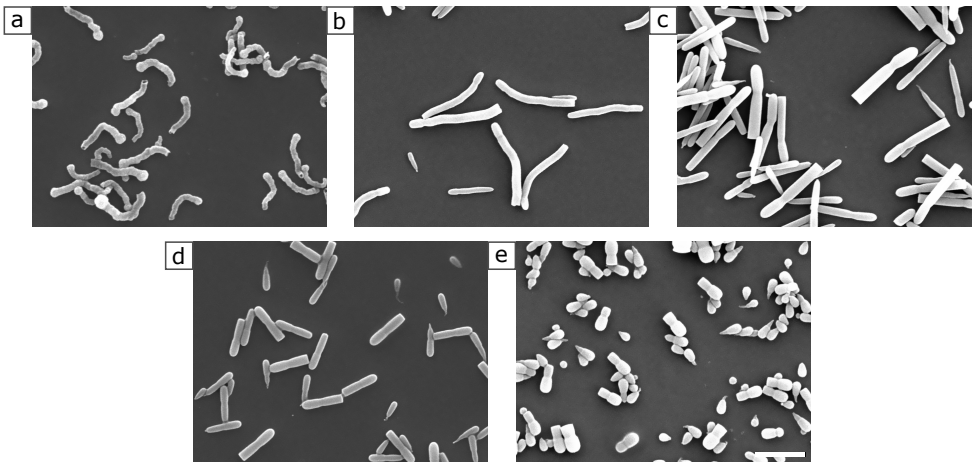


Figure 3.15: Evaluation of the amount of ammonium hydroxide with (a) 10, (b) 50, (c) 100, (d) 150, (e) 200 μL. All the images are the same size and the scale bar is 2 μm.

These results indicate the importance of pH. As exposed in 3.1, the difference between bending and diameter change can be explained by a difference in hydrolysis/condensation rate. These rates are highly dependent on the pH, so it is possible that at specific rates bending is observed. To evaluate the full range in which bent rods were obtained, the experiment was repeated with a smaller interval at low amounts of ammonium hydroxide. These results can be seen in figure 3.16.

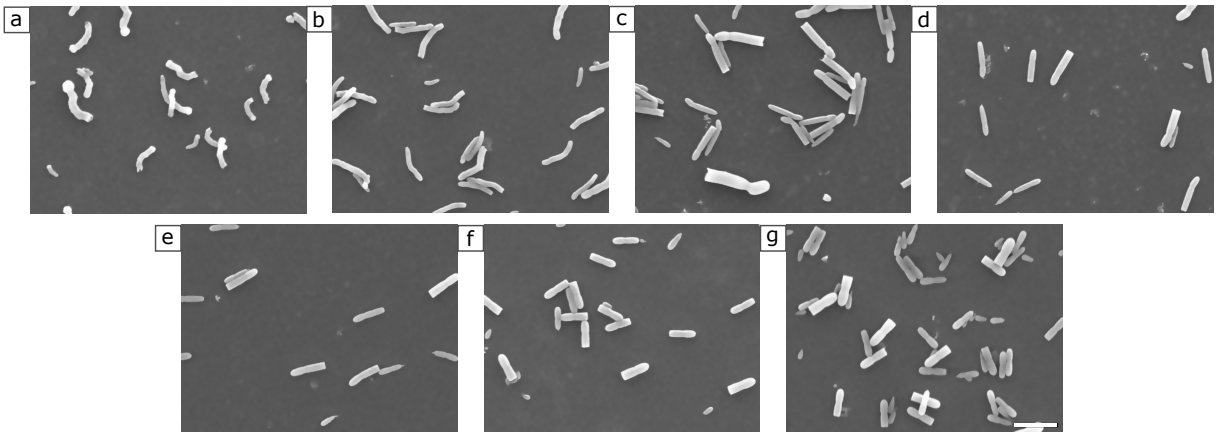


Figure 3.16: Evaluation of the amount of ammonium hydroxide with (a) 20, (b) 40, (c) 60, (d) 80, (e) 100, (f) 135, (g) 150 μL. All the images are the same size and the scale bar is 2 μm.

A similar trend can be observed as before, and above a certain amount of NH_4OH, they never bend, which may be related to the hydrolysis and condensation rates getting closer together with the pH increase (figure 3.2). This can also be part of the reason why in the work of Yang *et al.* [74] bent rods are obtained and not in the work of Dasktos *et al.* [88]. The former used 60 mg NH_4OH (approximately 66 μL) while the latter used 100 μL, and both used the same amounts of the other reagents. It was interesting to note that at 100 μL the rods barely bent compared to the test done before on another day. Similar experiments were done on different days and the results were not always reproducible. A summary of these results can be seen in figure 3.17 for 80 and 100 μL.

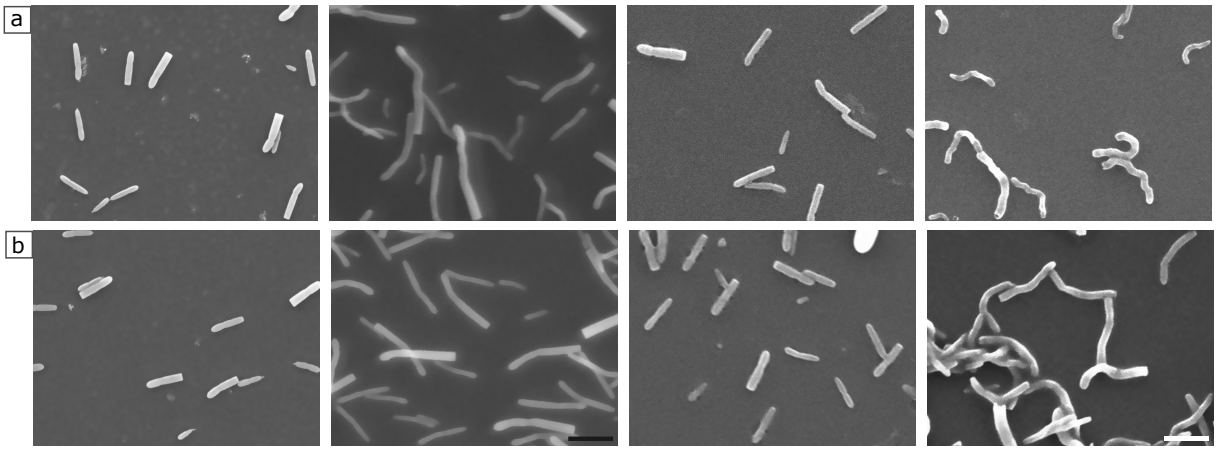


Figure 3.17: Interday reproducibility evaluation of the amount of ammonium hydroxide. Same synthesis conditions using (a) 80 and (b) 100 μL of NH_4OH done on different days. All the images are the same size and the scale bar is 2 μm.

These results were a bit surprising since the bottle of the ammonium hydroxide used had been opened recently, very well closed, and stored in the fridge. Still, it became clear that only using the amount of ammonium hydroxide was not enough to guarantee reproducibility. To overcome this problem, a new bottle of ammonium hydroxide was opened, the content was distributed in small vials that were very well closed and stored in the fridge. For each test done after that, a different vial was used and the pH was initially checked. This way, intra- and interday reproducibility were obtained as it is shown in figure figure 3.18

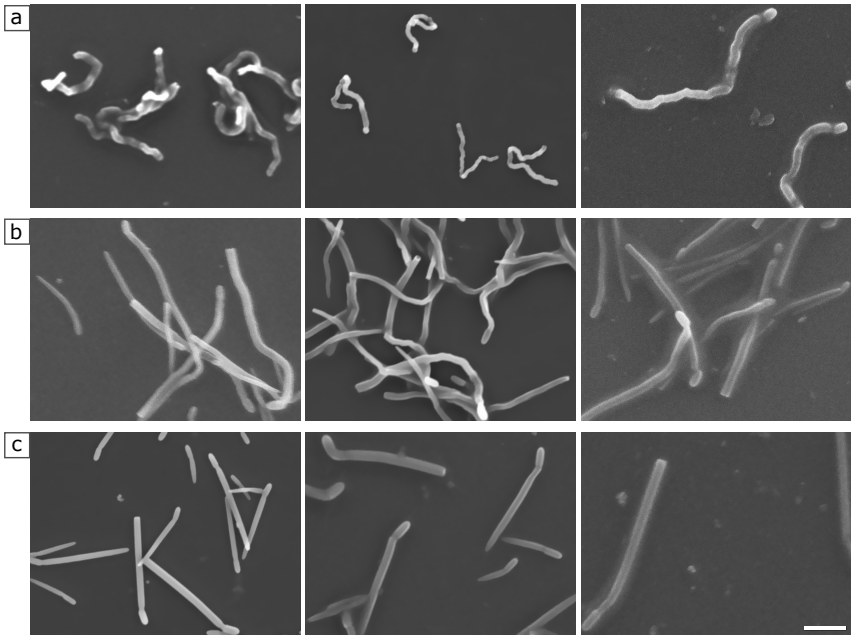


Figure 3.18: Interday reproducibility evaluation of the amount of ammonium hydroxide checked by pH. Same synthesis conditions using (a) 40, (b) 80, and (c) 100 μL of NH_4OH done on different days (each column represents one day). All the images are the same size and the scale bar is 2 μm.

Last, we quickly tested the temperature effect (figure 3.19). No bending was observed for 45 °C differently than before or for Yang *et al.* [74]. Increasing time (65 °C from 5 to 20 min) also did not result in bending at higher temperature. A further increase in temperature (90 °C) finally lead to bent rods, but with smaller angles than expected. None of the conditions tested resulted in more controllable angles.

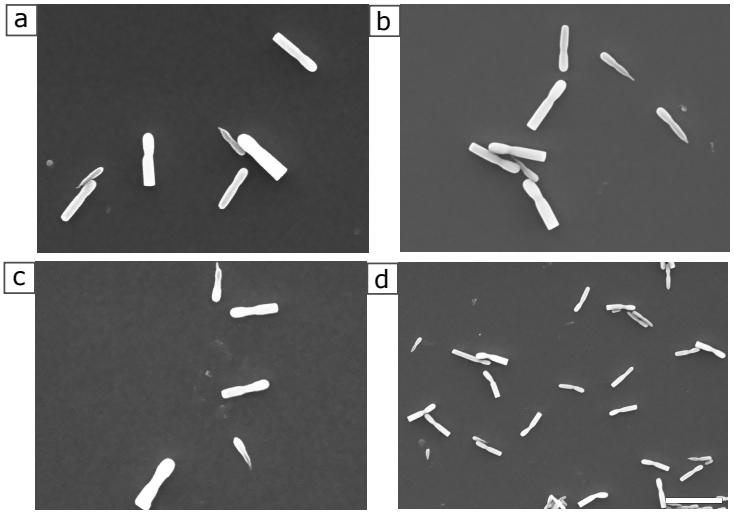


Figure 3.19: Evaluation of different temperatures and time with (a) 45 °C for 20 min, (b) 65 °C for 5 min, (c) 65 °C for 20 min and (d) 90 °C for 5 min. All the images are the same size and the scale bar is 2 μm.

Pre-hydrolysed TEOS

Hagemans *et al.* [87] tested if the pre-hydrolysis was enough to explain the bending of the rods by adding pre-hydrolysed TEOS or TMOS as a perturbation in the middle of the synthesis since both have different rates than pure non-hydrolysed TEOS. The addition of these reagents as perturbation led to bent particles. This is a clear indicator that the change in rates can affect the bending of the rods. So, we tested the addition of TMOS in the middle of the synthesis and we observed bedding (figure 3.20). However, for some rods, the bending resulted in a "double" kink or the end of the synthesis and the formation of a smaller rod. We decided to focus on temperature and evaluate which conditions resulted in bent rods and in a more narrow-angle dispersity.

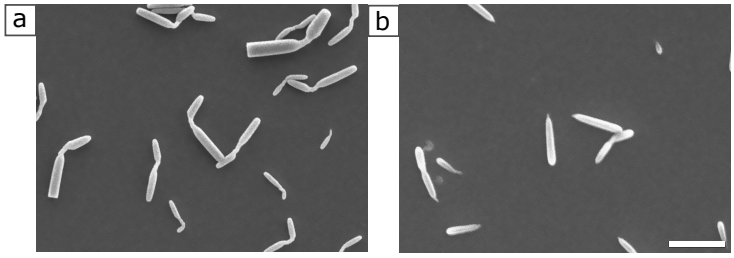


Figure 3.20: SEM images of the rods with the addition of (a)4 and (b) 6 μL of TMOS as perturbation. All the images are the same size and the scale bar is 2 μm.

To begin, we evaluated if the best would be to do acid or basic pre-hydrolysis. Since the hydrolysis rate is higher than the condensation rate for acidic pH, this seemed the best choice, which was done by Hagemans *et al.* [87]. However, the actual rod synthesis is done with base catalysis, so this catalyst was also investigated. As it can be seen in figure 3.21, there was no significant difference between either catalysis. We decided to use acid considering the higher hydrolysis rate and easier comparison with the literature.

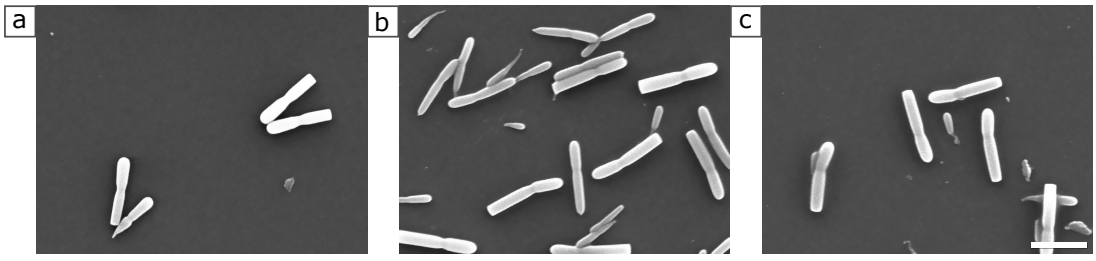


Figure 3.21: Comparison of TEOS with (a) no pre-hydrolysis, and pre-hydrolysed with (b) acid and (c) base. All the images are the same size and the scale bar is 2 μm.

The next variable we tested was the ratio of pre-hydrolysed TEOS to non-pre-hydrolysed

and the time of pre-hydrolysis, 30 and 120 min, as shown in figure 3.22. We used the same amounts reported in the literature (2.3 and 7 %) for 30 and 120 min. Relatively similar results were obtained independent of these percentages, for the same time, with longer rods with a higher bending angle being obtained at longer times of pre-hydrolysis. We also tested 100 % of TEOS pre-hydrolysed for 120 min and a curly bell shape was obtained. On the same day, we used an old TEOS that was opened for a long time and stored outside the desiccator. We can see the presence of "heads", long rods, and large bending angle distribution. The problem with using an old TEOS is reproducibility, especially once the reagent is finished (figure 3.22)

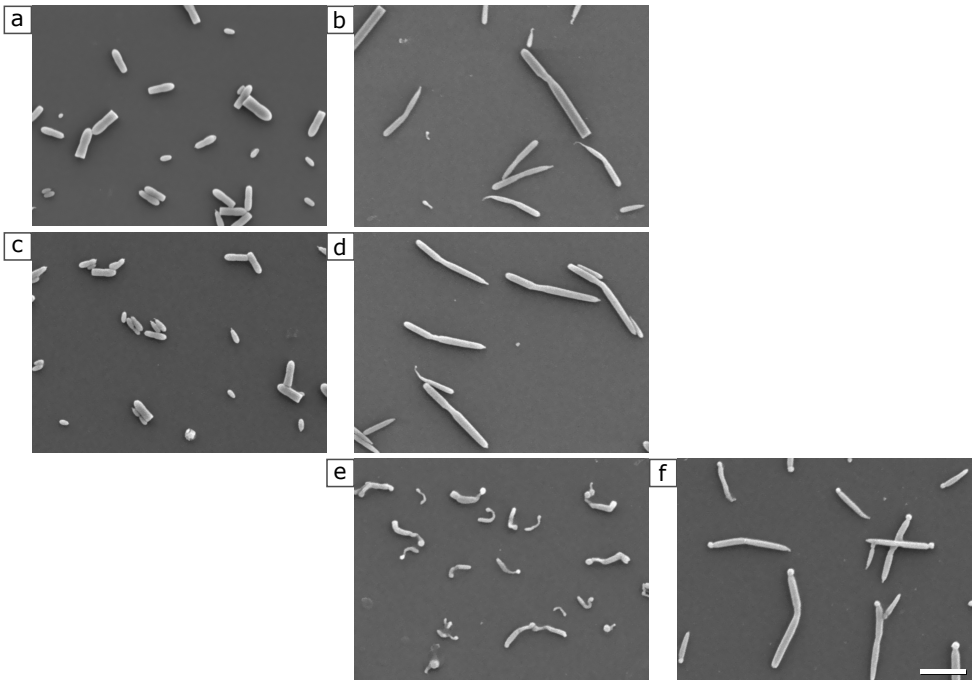


Figure 3.22: Evaluation of ratio of pre-hydrolysed:non-pre-hydrolysed TEOS and time of pre-hydrolysed with (a,b) 2.3 %, (c,d) 7 % and (e) 100 %; (a,c)30 min and (b,d)120 min; (f) is old TEOS. All the images are the same size and the scale bar is 2 μm.

Using a 7 % ratio, we evaluated further the impact of time and performed an experiment with a broad range of time as shown in figure 3.23. The results were quite different from the previous ones. During the pre-hydrolysis, precipitation (probably of silica) was observed approximately 10 min after the synthesis had started. TEOS and water are not miscible, however, ethanol is a sub-product of the synthesis and this ternary mixture has a region of miscibility. We never observed a complete homogenization of the system, differently than what has been reported for the concentrations used [87]. Possibly this is connected with how old the TEOS is, even though we were careful regarding this. The resulting mixture was then heterogeneous, explaining the difference observed interday.

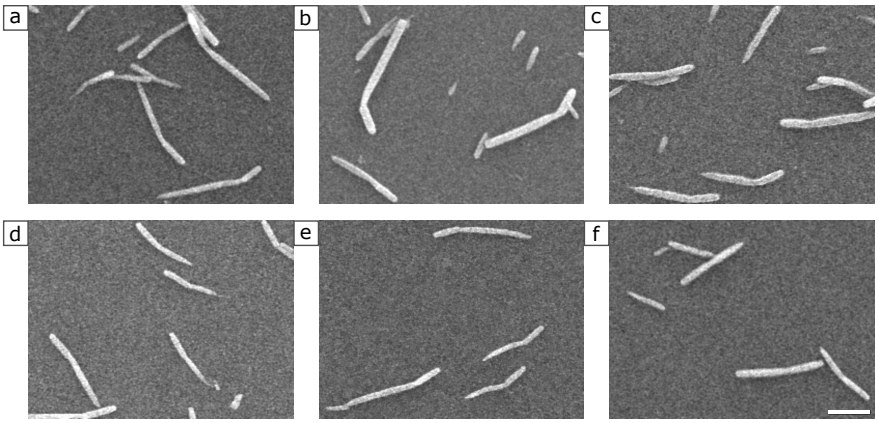


Figure 3.23: Evaluation of time of pre-hydrolysed with (a) 10min, (b) 30 min (c) 60 min, (d) 90 min, (e) 120 min and (f)180 min. All the images are the same size and the scale bar is 2 μm.

To try to solve this problem, a minimum amount of ethanol to allow complete homogenization was added to the system and the pre-hydrolysis was carried out. The extra amount of ethanol added to the system was negligible, so it was not taken out from the reagent being added in the synthesis. A homogeneous aliquot used in the synthesis was guaranteed this way. As can be seen in figure 3.24, there seemed to have a small difference in bending, so we kept testing the pre-hydrolysis with ethanol. This allowed us to have interday reproducibility (figure 3.25).

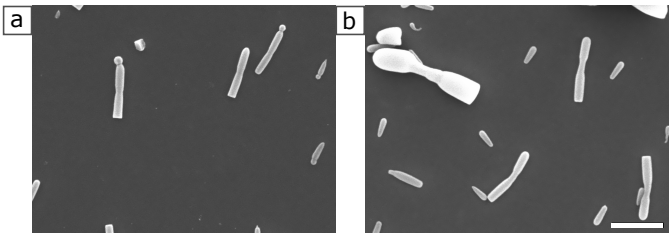


Figure 3.24: Evaluation of pre-hydrolysis done (a) without, and (b) with ethanol. All the images are the same size and the scale bar is 2 μm.

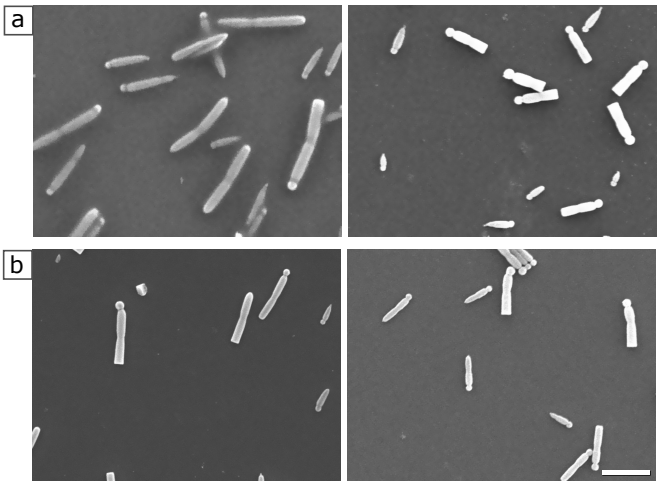


Figure 3.25: Interday evaluation of time of pre-hydrolysed with (a) 10min, and (b) 30 min. All the images are the same size and the scale bar is 2 μm.

Knowing that there is a relationship between the hydrolysis/condensation rate and bending, we tested the amount of ammonium hydroxide. Figure 3.26 shows a similar trend as before where the rods are curly then start bending, then straight. The bending was still observed at higher amounts of NH_4OH (135 μL) compared to when using non-pre-hydrolysed TEOS. The pre-hydrolysis works as the "matchstick" head can be seen.

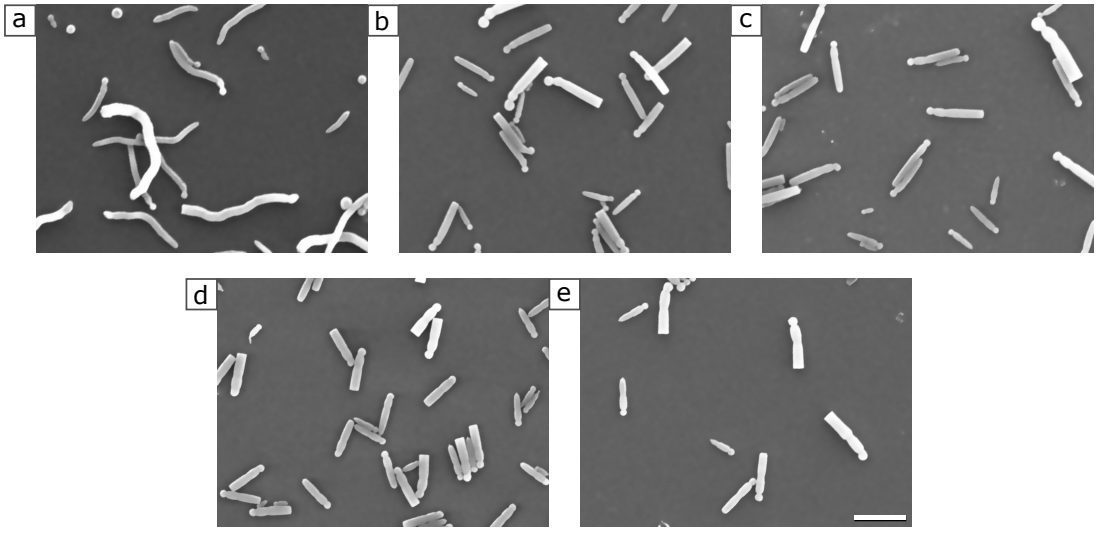


Figure 3.26: Evaluation of the amount of ammonium hydroxide with pre-hydrolysed TEOS with (a) 40, (b) 60, (c) 80, (d) 100, (e) 135 μL. All the images are the same size and the scale bar is 2 μm.

To check if the synthesis is reproducible, we repeated the experiment on different days, and the results were not reproducible. Figure 3.27 shows that the aspect ratio and bending of the rods are different when the synthesis is done on different days. This may be explained by a relationship between pH and pre-hydrolysis extension. Even though the time and proportion of pre-hydrolysis were the same, we did not check if the hydrolysis extension was equal. Small amounts of catalyst can have a significant difference in the rate of reaction [78]. The synthesis is more sensitive at lower NH_4OH concentrations, making it challenging to control the morphology without having the certainty of the pre-hydrolysis extension.

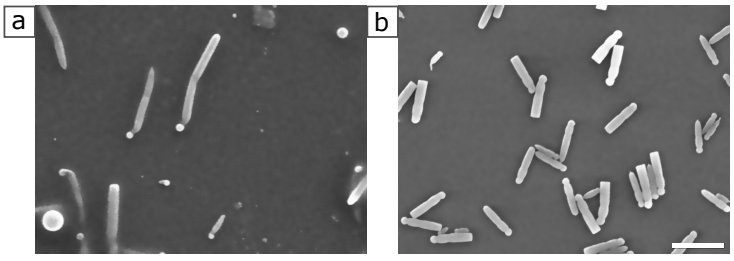


Figure 3.27: Interday reproducibility evaluation of the amount of ammonium hydroxide with pre-hydrolysed TEOS. Same synthesis conditions using 100 μL of NH_4OH done on different days. All the images are the same size and the scale bar is 2 μm.

Finally, we tested the amount of ammonium hydroxide using the old TEOS. It is possible to see the same pattern as before is followed with the increase of NH_4OH (figure 3.28). The rods do bent, just one more piece of evidence of the importance of pre-hydrolysed TEOS. Since it is not possible to control the extension of hydrolysis of an old TEOS, we could not make the angles more monodisperse in this case.

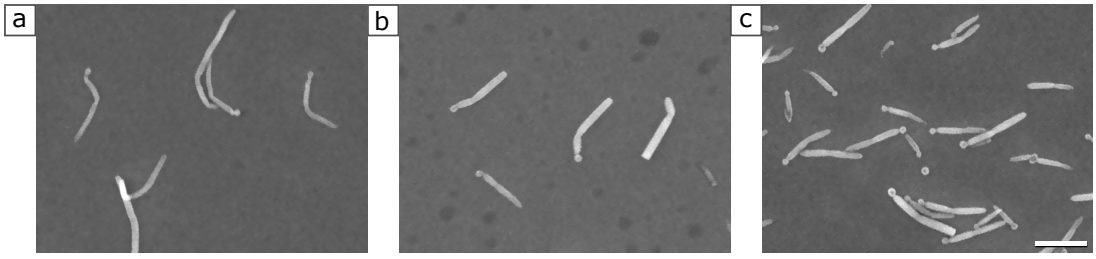


Figure 3.28: Interday reproducibility evaluation of the amount of ammonium hydroxide with pre-hydrolysed (old) TEOS. Same synthesis conditions using (a) 60, (b) 80, (c) 100 μL of NH4OH done on different days. All the images are the same size and the scale bar is 2 μm.

The synthesis has proven to be a challenge to reproduce and even more difficult to control and produce rods with monodisperse angles. It is possible that by changing the rates of hydrolysis and condensation, the silica starts growing differently within the droplet. There may be a quicker formation of solid on a new part of the droplet instead of the previous straight plane, and this results in the rod growing with a different orientation (angle). If this is the case, then the formation of random angles is inherent to the synthesis with perturbation, and it would not be possible to obtain a smaller angle distribution. More experiments are needed to confirm this hypothesis.

3.5 Conclusion

We were able to synthesize spherocylindrical rods in different sizes to mimic bacteria. The size and zeta potential of these rods were similar to the ones reported in the literature for *P. aeruginosa*. We were also able to modify their surface to later evaluate the effect of this parameter in the interaction with tactoids (chapter 5). The modifications resulted in positively charged or hydrophobic particles. Due to the challenge of determining particle wettability, we were able to only qualitatively determined the hydrophobicity of the particles.

The synthesis of bent-core particles was studied, first by attempting to change the surface

tension as a perturbation to move the rod's growth direction, which proved unsuccessful. PVP and Span80 resulted in a change of diameter while tert-butanol resulted in bent particles in a small number, while the majority of the particles were just short, probably due to the droplet being detached. Using temperature as perturbation resulted in the rods bending with a broad angle as reported previously in the literature [74]. Thus, we focused on trying to obtain different angles with a narrower distribution. Our study showed that ammonium hydroxide plays an important role and, due to its instability, using concentration instead of pH results in a lack of reproducibility. We also tested the effect of pre-hydrolysing TEOS to evaluate the changes in reaction rates following previous reports in the literature [87]. We noticed the rods bent, but again, reproducibility was challenging due to the difficulty in characterizing the extension of hydrolysis. The change in ammonium hydroxide and pre-hydrolysis indicates that the ratio of hydrolysis and condensation reaction rates is important for the direction the rod grows. However, it is difficult to control the pre-hydrolysis of TEOS, and, consequently, the synthesis is not easily reproducible. This is a problem when a specific morphology is desired.

Chapter 4

Phase behaviour of Pf4 and sodium alginate

Abstract

In this chapter, we present the study of tactoids formed by the mixture of Pf4 phage and sodium alginate. Using confocal microscopy, we followed the growth of tactoids over time for low concentrations of polymer. We also evaluated the size dependence with the concentration of the polymer. Finally, we obtained an experimental phase diagram in which isotropic and biphasic regions were measured. The biphasic region was further divided into tactoids or a network structure. We calculated a theoretical phase diagram, based on free volume theory, which agreed well with the experimental one. We have put our results into the context of liquid crystalline behaviour formed by other colloidal particles, including viruses.

4.1 Introduction

Rod-like particles are able to form liquid crystals, including droplets of nematic phase in an isotropic medium, called tactoids [98]. They are commonly found for both thermotropic and lyotropic liquid crystals and were first reported by Bawden in 1936 using a suspension of tobacco mosaic virus (TMV) [47]. Ever since, tactoids have been extensively studied theoretically and experimentally for several systems such as CNC [99], polyamides [72], clays [100], amyloid fibrils [42], and viruses [45, 46, 48].

Tactoids are a metastable state [45] – an intermediate energetic state that is a local minimum, with an energy barrier significantly that needs to be overcome to obtain the state of lowest energy state [101]. A system with F-actin was shown to present several steady states near equilibrium. Initially, there is the formation of a few tactoids of similar size, a relaxed steady state. After a perturbation is applied, there is an initial break of the droplets and slow formation of a bigger number of tactoids with varying sizes. This is indicative of the metastability of the system – a small perturbation alters the system and once altered, the system never returns to its previous state.

One possible explanation for this difference observed after the perturbation, is an energy barrier which is prohibitive for the onset of nucleation even at high concentrations. Once this barrier is overcome, it is energetically favourable for the tactoids to grow with the mesogens that are diffusing in the solution, leading to the formation of the two coexisting phases. The perturbation breaks these droplets and multiple seeds, which have already gone over the barrier, are present. In this way, more tactoids are formed within a wider size range (in this case coalescence was also observed) [38].

As mentioned in the introduction (chapter 1), the shape and director field of the tactoid depends on the competition between the elastic, and the surface (anchoring and surface tension) properties of the liquid crystalline phase [39]. The weight elastic and surface properties have on the tactoid shape and director field will also depend on characteristics of the mesogens, such as aspect ratio [28]. With amyloid fibrils, it is also possible to observe that specific shapes and configurations are obtained depending on the rod length [42]. cholesteric droplets (chiral nematic phase) are only obtained for shorter ones, while for longer fibrils highly elongated tactoids are seen. It was also observed that a decrease in fibril length also resulted in a decrease in anchoring

strength, which can explain the dependence of shape with the length [42].

With the addition of a non-adsorbing polymer, the depletion interaction plays a significant role in the phase behaviour, and the biphasic region is expanded [2]. The liquid crystalline phase behaviour displayed by mixtures of virus particles and polymer is well-known for certain *model* viruses such as *fd* virus [45,46] and TMV [47,48]. Recently, there is an increased interest in another rod-like phage, Pf4, in the presence of biopolymers [50, 51]. These particles have a symbiotic relationship with the pathogen *P. aeruginosa* in their biofilms, [50] and the formation of tactoids is believed to have a protective role against antibiotics [51].

In this chapter, we focus on the phase behaviour of mixtures of the Pf4 phage with the biopolymer sodium alginate. Sodium alginate was used since it is the main biopolymer found in the biofilm of *P. aeruginosa* [71]. Other papers have used a mixture of viruses and polymers such as Polyethylene glycol (PEO) [48, 72] and dextran [46, 49]. The main important difference is that these are neutral polymers while sodium alginate is a polyelectrolyte, so charge plays an important role in the physical-chemical properties.

PBS was chosen as the solvent for a similar reason since this buffer is nontoxic, isotonic and with an ion concentration that matches the ones of the human body. It also allows keeping the pH constant, usually at 7.4, a value also similar to the physiological one. It is composed only of monovalent cations, which is important in our application since divalent cations can result in cross-linked sodium alginate, forming a gel and significantly altering the system.

We explore the growth of the tactoids over time by looking at the effect of the polymer concentration (section 4.3.1). Having noticed a difference in tactoid size with the polymer concentration, we further study this observed phenomena as a function of sodium alginate and Pf4 concentrations (section 4.3.2). Last, we present the experimental phase diagram (section 4.3.3) and compare it to the theoretical one (section 4.3.4), identifying the boundary from isotropic to biphasic.

4.2 Experimental methods and materials

The experiments were done using the Pf4 isolated and purified as described in section 2.2.1 and the tactoids prepared as explained in section 2.2.4. Here we will briefly summarize how each

one of the experiments presented in this chapter was done.

We began by doing experiments focusing on the kinetics of the system. The labelled phage was mixed with the sodium alginate 1:1 (v:v) to obtain 6 μL of samples with final concentrations of 1 mg/mL of Pf4 and 2.5 or 15 mg/mL of sodium alginate. The phage was added in the capillary cell (figure 2.2), then the polymer was added, mixed in the vortex for 5 minutes and quickly imaged (less than one minute on average). For the sample of 15 mg/mL, we also tried to add the polymer in the cell already containing Pf4 in the microscope and mix it with the pipette tip to image it quicker; however, that did not provide additional information and was not explored further.

For the experiments to evaluate the effect of the component's concentration on the tactoid sizes, samples with final concentrations 1, 2, and 3 mg/mL of Pf4 in combination with sodium alginate 2.5, 5, 10, and 15 mg/mL were prepared. Aliquots of 3 μL of each component in different initial concentrations were added in an Eppendorf tube and vortexed for 5 min. Then the samples were transferred to a square capillary (figure 2.2), left equilibrating for 24 h in the fridge, and were imaged. The samples were returned to the fridge for another 24 h and were imaged again. The size of the tactoids was measured using a code developed previously in the group [25]. At least 3 z-stacks were obtained and after the individual tactoids have been extracted, their minor axis ($2r$), major axis ($2R$) (figure 4.1), aspect ratio (R/r), and volume were obtained. Each image shown for the same concentration of sodium alginate has approximately equal size (x and y dimensions are the same, and z varied at maximum by 3 μm). The z-stacks for the samples with sodium alginate 2.5 mg/mL are 2/3 longer since the tactoids are considerably bigger.

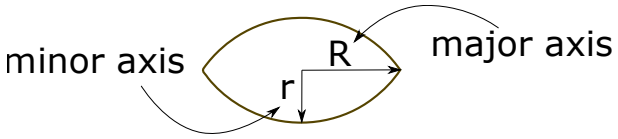


Figure 4.1: Schematic of tactoid showing the major axis (2R) and minor axis (2r).

For the phase diagram, first, a mixture of 1:200 labelled:unlabelled virus was prepared, which allowed higher concentrations to be obtained and avoid the detector saturation. Three different initial points were prepared similarly to the samples for kinetics. They were left equilibrating for 24h before being imaged. Then, they were diluted, each line at a different ratio, and left equilibrating for 24 h before being imaged. To guarantee the right concentration of

each point, the samples were weighed after being prepared, diluted and before and after being imaged. The procedure was followed until the isotropic phase was obtained. This could not be done for line 4 since the amount necessary to have the appropriate weight was too high, so the individual points were prepared in capillary similarly to the study of concentration. The first points used and the dilution ratio are presented in table 4.1.

Table 4.1: Final concentrations of the first point and dilution ratio for each line experimentally explored in the phase diagram.

Line	Pf4 (mg/mL)	Sodium alginate (mg/mL)	Dilution ratio
1	11.7	6.0	0.70
2	13.6	3.0	0.80
3	14.7	1.0	0.90
4	16.2	0.05	0.95

4.2.1 Phase diagram theoretical background

To calculate the theoretical phase diagram, we followed the procedure set out in the book by Lekkerkerker and Tuinier [2]. First, we used Onsager's theory to calculate the point where the isotropic-nematic (IN) transition occurs, assuming thin, long rigid hard rods. Onsager showed that no attraction forces were necessary to obtain phase separation, and the free energy may be described using a virial expansion. In the case of high aspect ratio hard particles, the expansion may be truncated after the second virial term (the results are exact for infinitely thin rods). The Helmholtz free energy for a dispersion of N rods can then be written as

$$\frac{F[f]}{NkT} = constant - 1 + ln(c) + \sigma[f] + c\rho[f], \tag{4.1}$$

where c represents a dimensionless concentration, σ is proportional to the orientational entropy per particle and ρ is the packing entropy per particle. The orientation distribution of the particles (f) is determined by the minimization of the free energy. Considering that the distribution function must satisfy the inversion symmetry (θ is equivalent to $\pi - \theta$) and that must be normalized, it is possible to obtain f for the isotropic phase for all concentrations, and consequently ρ, σ and the free energy

$$f_I = \frac{1}{4\pi}, \quad \sigma_I = 0, \quad \rho_I = 1, \tag{4.2}$$

and therefore

$$\frac{F_I}{NkT} = const - 1 + ln(c) + c. \tag{4.3}$$

For the nematic phase, an analytical expression for f has not yet been obtained, so numerical methods or a trial function can be used. The first approach gives more accurate results, but the second is simpler to solve. Onsager successfully chose a function that agrees very well with the numerical methods. However, it is not a simple function, so we chose to use the Odijk approximation, in which a Gaussian distribution is used for the orientation distribution function:

$$f_G \approx \begin{cases} \tilde{N}(\kappa)exp(\frac{-1}{2}\kappa\theta^2) & \text{for } 0 \leq \theta \leq \frac{\pi}{2}, \\ \tilde{N}(\kappa)exp(\frac{-1}{2}\kappa(\pi-\theta)^2) & \text{for } \frac{\pi}{2} \leq \theta \leq \pi, \end{cases} \tag{4.4}$$

where $\tilde{N}$ is the normalization constant.

For a transition to happen, the phases must be in mechanical and chemical equilibrium. This means that both phases must have the same osmotic pressure and chemical potential, represented by the coexistence equations:

$$\begin{cases} P_I(c_I) = P_N(c_N), \\ \mu_I(c_I) = \mu_N(c_N). \end{cases} \tag{4.5}$$

The osmotic pressure and chemical potential can be obtained from the free energy, by differentiating with respect to V and N, respectively, resulting in

$$\begin{cases} \frac{Pb}{kT} = c + c^2\rho[f], \\ \frac{\mu}{kT} = const + ln(c) + \sigma[f] + 2c\rho[f]. \end{cases} \tag{4.6}$$

Using eq. (4.2) it is possible to obtain P and μ for the isotropic phase. With the Odijk approximation, it is possible to obtain σ and ρ in terms of κ for the nematic phase. κ is found by minimizing the free energy, such that the pressure and chemical potential are obtained and

by equating the expressions for both phases, the coexistence equations are derived

$$\begin{cases} c_I + c_I^2 = 3c_N, \\ ln(c_I) + 2c_I = 3\ln(c_N) + ln\left(\frac{4}{\pi}\right) + 3, \end{cases} \tag{4.7}$$

and, consequently, the concentrations of each phase where the transition occurs, are equal to

$$c_I = 3.451, c_N = 5.122. \tag{4.8}$$

To consider the effect of the rods aspect ratio and the presence of the depletion attraction, higher virial terms are necessary. For that, we use Scaled Particle Theory (SPT) to calculate the transition, first without and then in the presence of a depletant. SPT allows the chemical potential and pressure of a system to be obtained based on the reversible work necessary to add a new particle to the system studied. With this theory, it is possible to incorporate higher virial coefficients.

To start, the reversible work (W) necessary to insert an additional rod in a system with rods has to be obtained. This is done by expanding the size of the particle to be inserted from zero to its actual size. This way, the excess part of the chemical potential can be calculated. Replacing this contribution in eq. (4.6), the chemical potential is

$$\frac{\mu}{kT} = const + ln(y) + \sigma[f] + (1 + 2A[f])y + (A[f] + \frac{3}{2}B[f])y^2 + B[f]y^3, \tag{4.9}$$

where

$$A[f] = 3 + \frac{3(\gamma-1)^2}{3\gamma-1}\rho[f], \qquad y = \frac{\phi}{1-\phi},$$
$$B[f] = \frac{12\gamma(2\gamma-1)}{(3\gamma-1)^2} + \frac{12\gamma(\gamma-1)^2}{(3\gamma-1)^2}\rho[f], \qquad \phi = nv_0,$$
$$v_0 = \frac{\pi}{4}LD^2 + \frac{\pi}{6}D^3,$$
$$\gamma = 1 + \frac{L}{D}.$$

Using the Gibbs-Duhem equation, it is possible to obtain the pressure

$$\frac{Pv_0}{kT} = y + A[f]y^2 + B[f]y^3, \tag{4.10}$$

and the free energy

$$F = \frac{F[f]}{NkT} = constant - 1 + \sigma[f] + ln(y) + A[f]y + \frac{1}{2}B[f]y^2. \tag{4.11}$$

To calculate the transition concentrations, the free energy ($F[f]$) is minimized with respect to f. Then, f is obtained, the pressure and chemical potentials are determined and the coexistence equations are solved. Instead of minimizing the free energy, we again use the Gaussian distribution approximation. The calculations are simpler and it has been shown there is good agreement with the numerical solutions, even though it overestimates. Minimizing the free energy with respect to κ gives

$$\kappa = \frac{36}{\pi}\frac{(\gamma-1)^4}{(3\gamma-1)^2}\left(y + \frac{2\gamma}{3\gamma-1}y^2\right)^2. \tag{4.12}$$

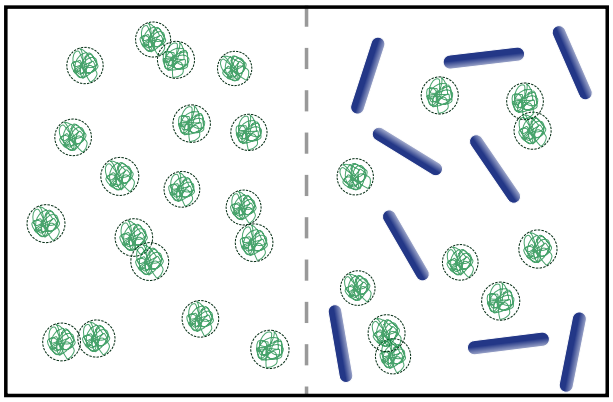


Figure 4.2: Schematic representation of the system of rods and depletants in equilibrium with a reservoir of depletants.

Finally, to consider the presence of depletants, we consider a polymer represented as a penetrable hard sphere (phs) with a diameter σ. We first assume there is a system of colloidal rods + phs in osmotic equilibrium with a theoretical reservoir of phs (figure 4.2). This theory is known as the free volume theory, and the concentration of phs in each phase follows the semi-grand potential that describes the colloid+depletant system, allowing it to be calculated through

$$\Omega(N_1, V, T, \mu_2) = F_0(N_1, V, T) - P^R < V_{free} >_0, \tag{4.13}$$

where the subscript 0 refers to a system of just rods, 1 and 2 to the rods and the depletants, respectively, in the system, the superscript R to the reservoir and $< Vfree >$ to the volume

available in the system for the penetrable hard spheres. F_0 can be obtained through eq. (4.11) and the osmotic pressure of the phs in the reservoir is

$$P^R = n_2^R kT, \tag{4.14}$$

where n_2^R is the number density of phs in the reservoir. The free volume is defined in terms of the free volume fraction $\alpha = \frac{<Vfree>_0}{V}$ and can be found from the reversible work for inserting the phs in the hard rod suspension (W). This can be obtained using SPT, and the free volume fraction is found to be

$$\begin{aligned} \alpha &= (1-\phi_1)exp[-Q(\phi_1)], \\ Q(\phi_1) &= ay_1 + by_1^2 + cy_1^3, \end{aligned} \tag{4.15}$$

where

$$\begin{aligned} a &= \frac{6\gamma}{3\gamma-1}q + \frac{3(\gamma+1)}{3\gamma-1}q^2 + \frac{2}{3\gamma-1}q^3, & y_1 &= \frac{\phi_1}{1-\phi_1}, \\ b &= \frac{1}{2}\left(\frac{6\gamma}{3\gamma-1}\right)^2 q^2 + \left(\frac{6\gamma}{3\gamma-1} + \frac{6(\gamma-1)^2}{(3\gamma-1)^2}\rho[f]\right)q^3, & q &= \frac{\sigma}{D}, \\ c &= \frac{2}{3\gamma-1}\left(\frac{12\gamma(2\gamma-1)}{(3\gamma-1)^2} + \frac{12\gamma(\gamma-1)^2}{(3\gamma-1)^2}\right)q^3, & \gamma &= \frac{L}{D}+1. \end{aligned}$$

The pressure and chemical potential of the system are then

$$\begin{aligned} P = -\left(\frac{\partial\Omega}{\partial V}\right)_{N_1,\mu_2} &= P^0 + P^R\left(\alpha - n_1\frac{d\alpha}{dn_1}\right), \\ \mu = \left(\frac{\partial\Omega}{\partial N_1}\right)_{V,\mu_2} &= \mu_1^0 - P^R\frac{d\alpha}{dn_1}, \end{aligned} \tag{4.16}$$

where the superscript 0 refers to the pure rod system. With all the contributions to the semi-grand potential, it is possible to obtain the phase diagram using the same procedure as before. Again, we use the Gaussian distribution and calculate the dimensionless pressure and chemical potential as follows

$$\begin{aligned} \tilde{p} &= \tilde{p^0} + \phi_2^R\left(\alpha - \phi_1\frac{d\alpha}{d\phi_1}\right)\frac{1}{2q^3}(3\gamma-1), \\ \tilde{\mu_1} &= \tilde{\mu_1^0} - \phi_2^R\frac{d\alpha}{d\phi_1}\frac{1}{2q^3}(3\gamma-1). \end{aligned} \tag{4.17}$$

Note that κ is still given by eq. (4.12) as it is needed for the unperturbed system, i.e. the

system without phs. Finally, we solve the coexistence relations

$$\begin{cases} \mu_1^I(n_1^I, \mu_2) = \mu_1^{II}(n_1^{II}, \mu_2) \ , \\ P^I(n_1^I, \mu_2) = P^{II}(n_1^{II}, \mu_2) \ . \end{cases} \tag{4.18}$$

4.3 Results and Discussion

The tactoids formed by Pf4 virus and sodium alginate have been studied previously in the group [25, 102] and some of the phenomena observed were further explored in this thesis. First, we investigated the growth of the tactoid over time (section 4.3.1). Afterwards, we evaluated the size of the tactoid dependence with the concentration of the components in section 4.3.2. We then explored the phase diagram, experimentally using four different dilution lines (section 4.3.3), and theoretically using free volume theory (section 4.3.4).

4.3.1 Kinetics

To evaluate the growth of tactoids with different sizes, two different concentrations of sodium alginate were used, 15 and 2.5 mg/mL, named samples 1 and 2, respectively, both with Pf4 at 1 mg/mL. The tactoid formation is faster and does not change in size significantly at higher concentrations of sodium alginate. The size will be explored later, in section 4.3.2. Sample 1 formed so fast that whenever we obtained the first image ($t_0 = 0$), tactoids had already formed. We tested imaging more quickly by having the sample cell with Pf4 in the microscope and adding the polymer just before imaging, but still, tactoids had already formed, indicating the process happens in a few seconds.

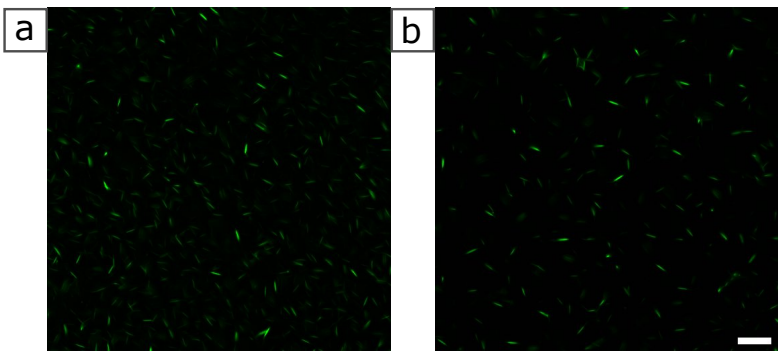


Figure 4.3: Confocal microscope image of sample 1, high polymer concentration, at t= (a) 0 and (b) 5 h. All images are the same size and the scale bar represents 10 μm.

Using a lower concentration of sodium alginate (sample 2) we could follow the growth of the tactoids. Initially, we saw a few brighter dots on a green background. This is indicative of the presence of a few nuclei in an isotropic medium. Because all the viruses are died and move quicker than the microscope scanning time, it is not possible to see individual phages, but rather this leads to a continuous green background (using high saturation). Eventually, the tactoids start growing, and a homogeneous black background is obtained approximately 1 hour after mixing. Figure 4.4 shows the growth of tactoids for almost 3 hours, although, since the tactoids move in and out of the imaging region, it was difficult to follow the same ones growing. After equilibrating for 5 hours it is possible to see in figure 4.5 b that their size after the same amount of time is significantly bigger than for the sample 1.

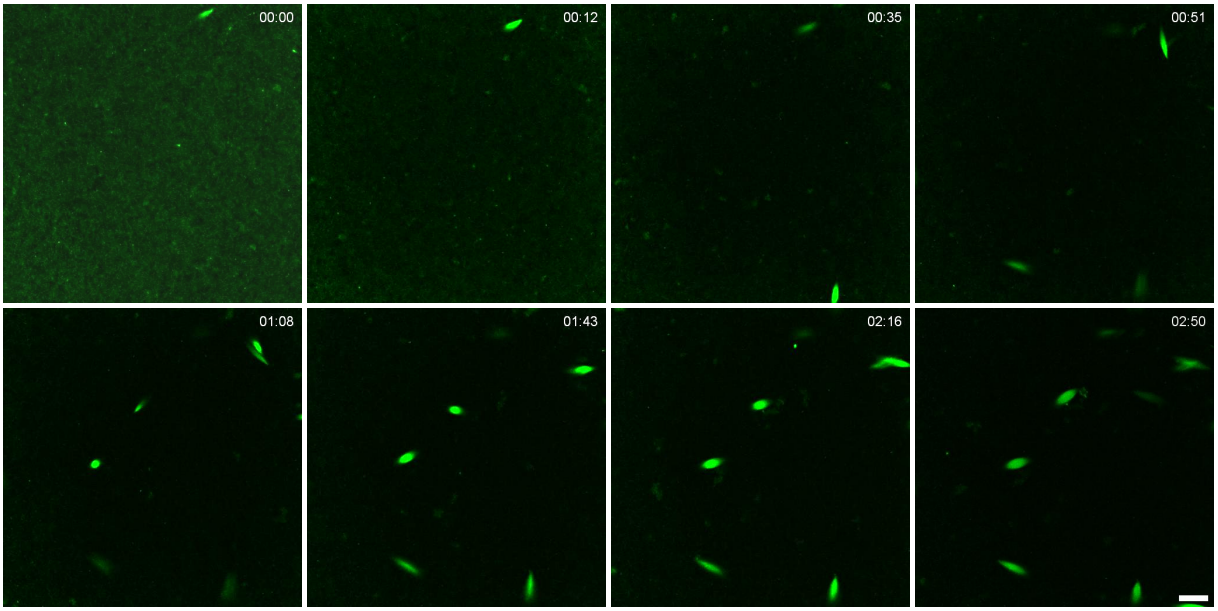


Figure 4.4: Confocal microscope images at different times of tactoid growth for sample 2, low concentration of sodium alginate. The images were obtained only at one height, so the tactoids are coming in and out of the plane. All images are the same size, the scale bar represents 10 μm, and the time is in hours:minutes.

The exact growth pathway that a tactoid follows is not completely understood, but some experiments reported in the literature elucidate our observations. A simulation following the isotropic-nematic transition for a system of colloidal hard rods showed spinodal decomposition and nucleation and growth mechanisms [103], which were experimentally observed for boehmite rods [104], F-actin [38, 105], and clay rods [106]. Similar observations were made on mixtures of rod-like viruses and polymer. Using flow-induced quench with *fd* virus and Dextran polymer, it

has been shown that the mechanism followed is dependent on the overall concentration of the nematic phase. [35, 107].

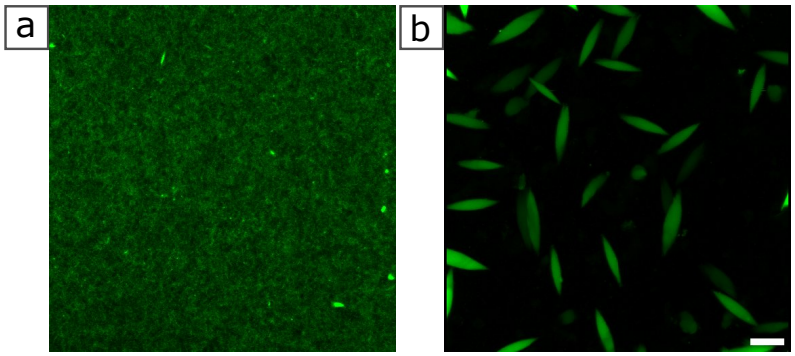


Figure 4.5: Confocal microscope images of sample 2, low concentration of sodium alginate, at t= (a) 0 and (b) 5 h. All images are the same size and the scale bar represents 10 μm.

None of our results suggests spinodal decomposition was followed. Since the mesogen concentrations we used are not as high as the ones reported in the literature, the only mechanism that took place was probably nucleation and growth. Alternatively, it is possible that the time frame for Pf4 is different and that we could not observe the initial stages of spinodal decomposition. Regarding the growth of the tactoid, two mechanisms have been observed: mesogen diffusion from the isotropic to the nematic phase and the coalescence of tactoids. In our experiments, only the first was observed. The second has been seen for Pf4, in our group [102], and reported for other mesogens [37, 108].

For tactoids to coalesce, they need to be in close proximity, so the viscosity of the isotropic phase is important for the diffusion of the tactoids. Once the tactoids are in close proximity, the viscosity of the nematic droplet is important since it refers to the resistance to flow, a resistance that the tactoids need to overcome in order to coalesce. This has been shown in the literature - the tactoid coalescence is dominated by liquid properties (viscosity and interfacial tension) [37]. In this way, it is likely that the alignment of the viruses is necessary for the tactoids to merge, being tip-to-tip for Pf4 [37, 102, 108]. This alignment is dependent on the rotational diffusion, so it can be a slow process or rarely observed, especially in our system which contains long rods.

The depletion interaction probably also has a role in the observed timescale. The higher the concentration of the depletant, the stronger the interaction, which means that locally, viruses will feel a stronger effective attraction in the more concentrated system, resulting in the observed

quick formation of tactoids of sample 1. However, for a smaller concentration of sodium alginate, small nuclei form, but the depletion interaction is not as strong to push all rods together, resulting in the isotropic phase initially observed and slowly growing droplets.

The increase in polymer concentration also leads to a change in the viscosity of the system, which influences the virus diffusion from the isotropic phase to the nematic droplets. Probably, for sample 1, the viscosity of the system is so high, that the individual rods (and tactoids) diffuse slowly. The opposite is seen for sample 2, where most of the particles are initially in the isotropic phase and the phage diffuses to the nematic phase. The difference in depletion interaction and viscosity can explain the difference in size for the same amount of time, and possibly, for the final equilibrated state, showing how this problem becomes more complex due to the addition of polymers.

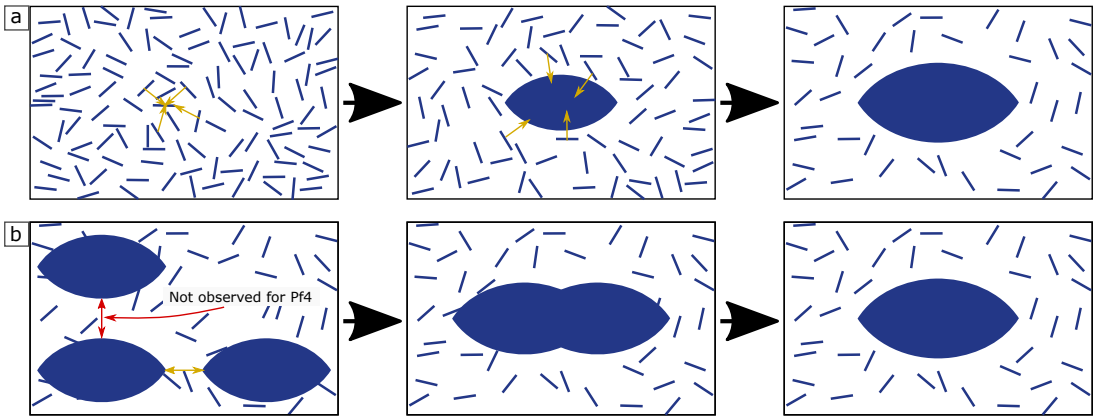


Figure 4.6: Schematics of the tactoids growth mechanisms: (a) nucleation and growth with mesogens diffusing from the isotropic to the nematic phase and (b) coalescence of tactoids.

4.3.2 Size

To evaluate how Pf4 and sodium alginate affect the tactoid size, we imaged samples of multiple concentrations 24 and 48 h after their preparation. Visually it is possible to notice that as the concentration of sodium alginate increases, the measured size of the tactoid decreases (as seen in section 4.3.1). From 2.5 to 5mg/mL, the tactoid size differs greatly, with this difference getting smaller with the polymer concentration. These observations seem to be the case for both 24 (figure 4.7) and 48 h.

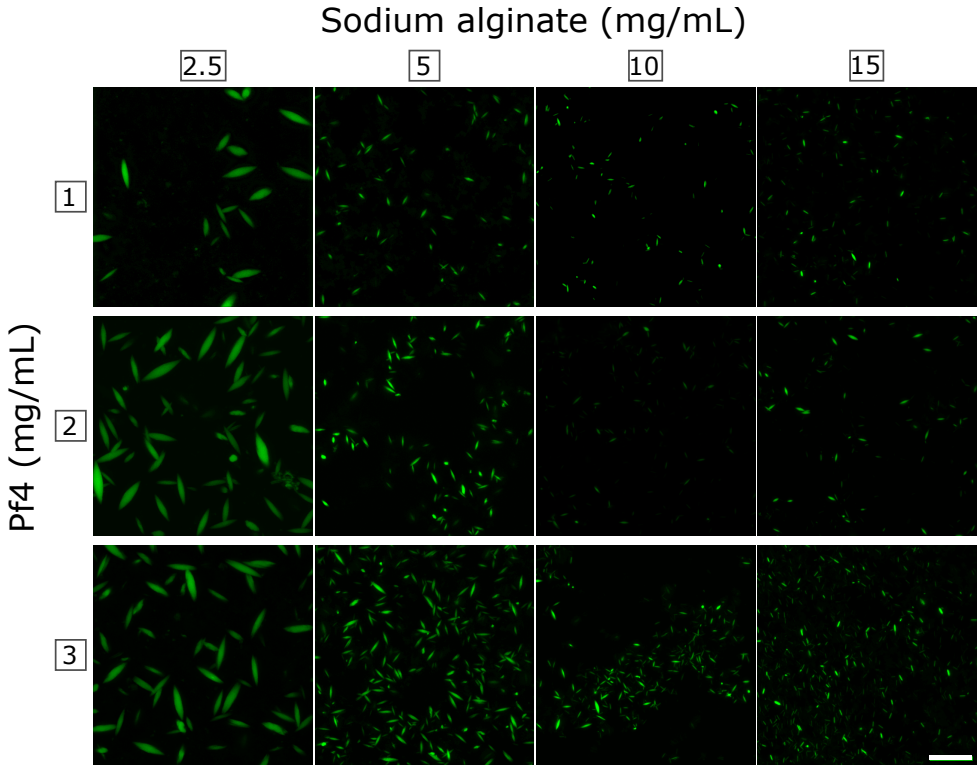


Figure 4.7: Confocal microscope images of the tactoids with different concentrations of sodium alginate and Pf4 after 24 h equilibrating. All images are the same size and the scale bar represents 20 μm.

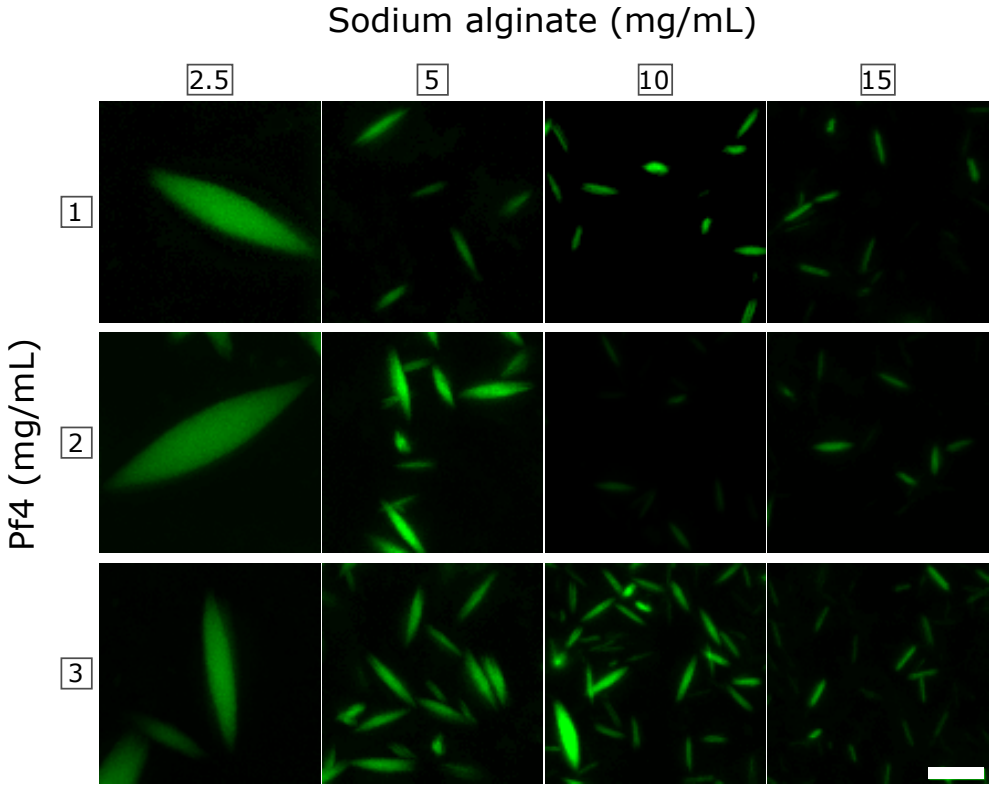


Figure 4.8: Magnification of figure 4.7 - confocal microscope images of the tactoids with different concentrations of sodium alginate and Pf4 after 24 h equilibrating. All images are the same size and the scale bar represents 5 μm.

To confirm the actual sizes and relationship with concentration, the tactoids were measured from 3D stacks as described in section 2.2.4. For all the values obtained, there is a noisy trend. This could be due to actual physical phenomena, or to the difficulty of measuring small tactoids due to the microscope resolution. We will discuss by looking at the main trends. In the magnification of the small tactoids, we see the shape is not spindle-like for a high concentration of polymer. They are more similar to a rectangular bundle, and this could also affect our measurements and observations (figure 4.8).

It is possible to note that both the minor and major axis decreased with the increase of sodium alginate for each concentration of Pf4 and for both times analysed. The aspect ratio of the tactoid follows a similar trend as the one observed for each dimension – the lower the concentration of sodium alginate, the higher the aspect ratio. The aspect ratio does not change considerably over the times analysed. The volume of the tactoids has changed from 24 to 48 h, with most samples growing, and the greater difference being for smaller sodium alginate concentrations as seen in the previous section – the tactoids grow slowly with the increase of viscosity (figure 4.9).

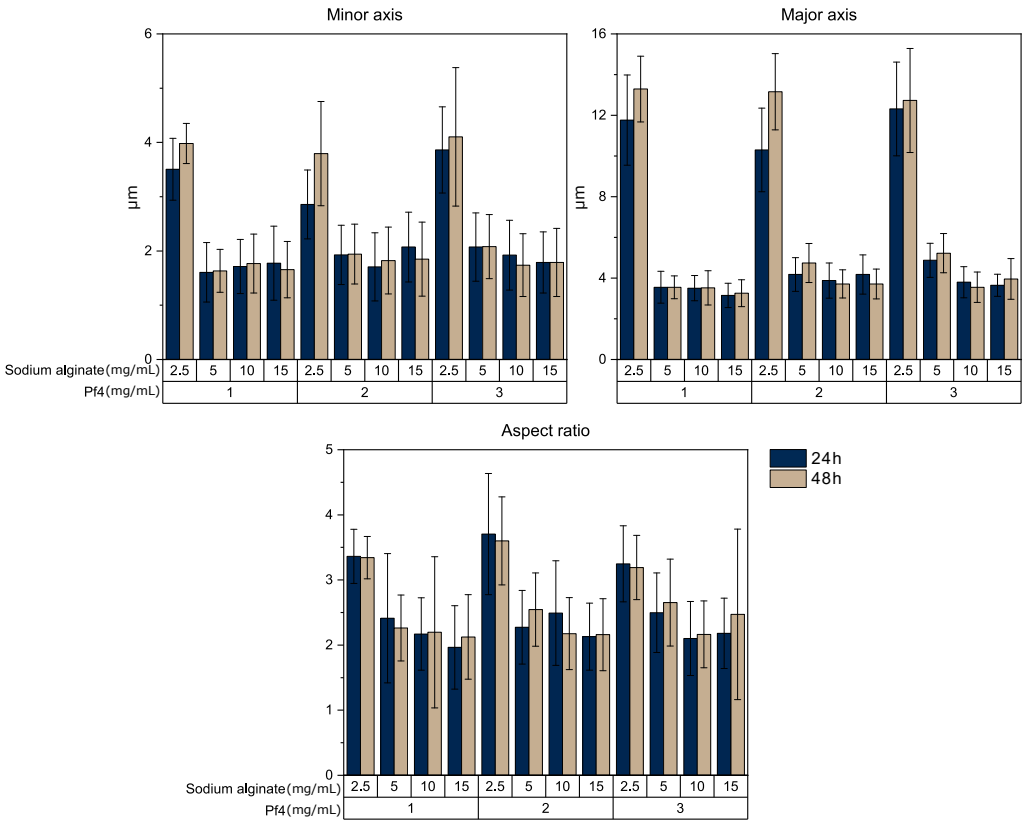


Figure 4.9: Distribution graphs of the size of the major axis (2R), minor axis (2r) and aspect ratio (R/r) of the tactoids after 24 and 48 h equilibrating. The column bars show the average and the error bars the standard deviation of the measurement.

Size determinations were done using 2D measurements previously in the literature [51] and in the group [102], and an increase followed by a decrease on the major axis and area, respectively, was observed. Both studies used only one concentration for these measurements, being closer to our sodium alginate 5 mg/mL and Pf4 1 mg/mL. For this sample specifically, no change is observed in the major axis size and the volume of the tactoid does decrease from 24 to 48 h. In this way, we can see that the noise in the trend may be related to specific behaviours of each concentration, and related to the time necessary to equilibrate.

The concentration of Pf4 seems to influence the number density of tactoids (number of tactoids per volume) in the sample (figure 4.10). The higher the concentration of the virus, the more tactoids are formed. In general, the number of tactoids decreased from 24 to 48 h indicating they merged, which has been previously observed in the group [102] and with tactoids of other mesogens [99]. It is expected that as the tactoids grow, for a bipolar director field, the aspect ratio decreases since bigger tactoids pay less elastic distortion, resulting in a more spherical shape, while smaller tactoids are spindle-like to avoid paying a higher elastic penalty. For us, the volume decreases with the increase in sodium alginate while the aspect ratio decreases. This could be due to the aspect ratio obtained being small (between 2 and 4.5), indicating that the elastic distortion dominates.

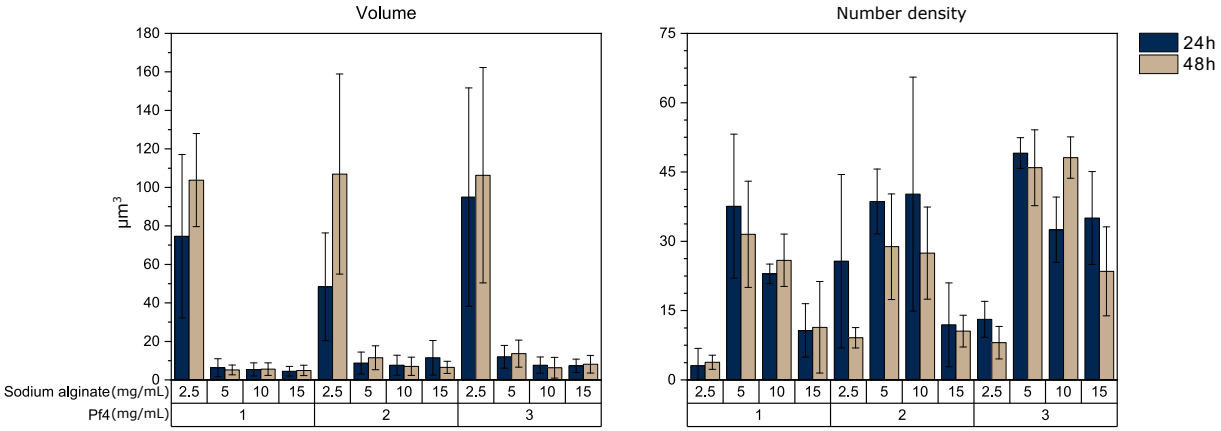


Figure 4.10: Distribution graphs of the volume and number density of the tactoids after 24 and 48 h equilibrating. The column bars show the average and the error bars the standard deviation of the measurement. For the number density of the tactoids, the average and standard deviations were calculated using each image as one data point for each concentration. For the number density, the values were normalized and border tactoids are not considered, which may result in a variation compared to the actual values.

When imaging the bigger tactoids (sodium alginate 2.5 mh/mL), a "flower-like" array was observed a few times. This has been reported previously in the literature for amyloid fibrils

with longer rods. The authors' hypothesis is that the longer rods can form entanglement points where the structures nucleate [42]. Considering our sample is polydisperse for the length of the rods [51], it is difficult to say only the longest rods were the ones forming the structures.

However, fractionation is a well-known phenomenon in biphasic liquid crystalline systems [106, 109]. As shown in the introduction, the concentrations for transition depend on the aspect ratio of the mesogens. In this way, when longer rods are together, the concentration necessary for the formation of the nematic phase is smaller. So, the longer rods will be in the nematic phase, while the shorter ones will remain in the isotropic [106, 109], suggesting that longer rods are predominantly present in our tactoids. A relationship with the size of the tactoid probably also exists since these structures were not observed with the small tactoids.

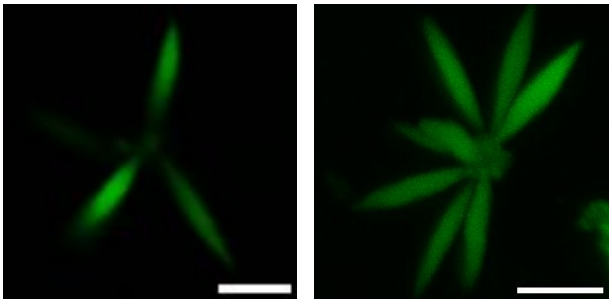


Figure 4.11: Flower-like array of tactoids. Scale bar represents 5 μm.

4.3.3 Phase Diagram

Four initial samples were prepared and diluted in different ratios, resulting in four dilution lines. The microscopy images obtained for all the points after 24 h of equilibration are presented in figure 4.13 and the corresponding diagram in figure 4.12. An isotropic and a biphasic region were obtained, with the biphasic region further separated in tactoids and network structures based on the morphology. A fully nematic phase was not observed, possibly because of the highest concentration of the virus we could obtain. Note that the viscosity of the Pf4 phage increases considerably with the concentration, making it difficult to concentrate a sample above 20 mg/mL. Considering the length of our rods rotational diffusion is very slow, and the viscosity is so high that may be too long for practical terms to observe complete phase separation in the coexistence region and may also explain why no pure nematic phase was observed in our work.

In line 1, we only observed tactoids, while in line 2 there was a transition from network to tactoids, and in lines 3 and 4 only network structures were obtained. The tactoids' size follows

the same trend seen before - the lower the concentration of sodium alginate, the bigger the tactoids formed. The network seems to be made of small tactoids connected in continuous lines, which appear to also have a size change with the sample dilution.

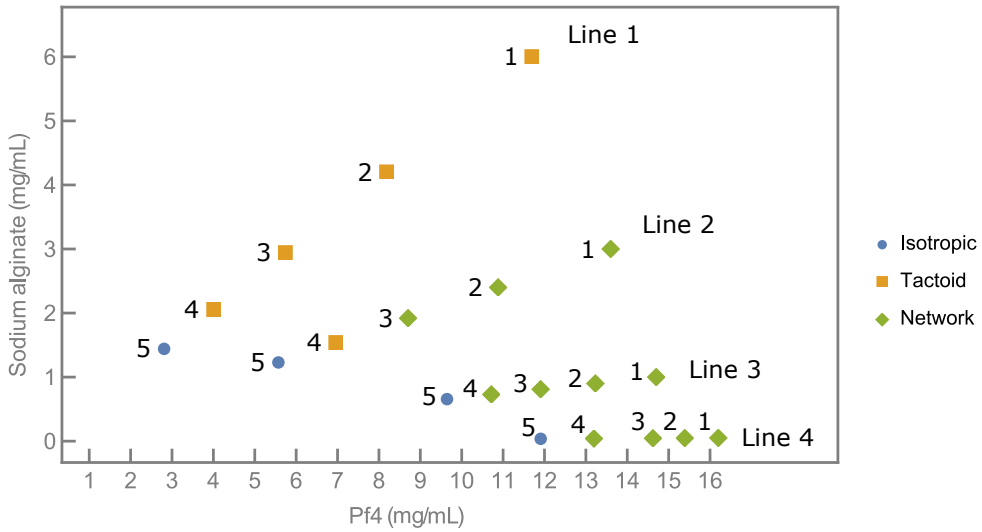


Figure 4.12: Experimental phase diagram showing four dilution lines with the circular blue dot representing the isotropic phase, the orange squares the tactoids and the green diamond the network structures. The numbers in each line are the dilution points.

In the isotropic phase, it is possible to see individual viruses on the wall of the capillary since they stick to the glass wall and move much slower than in bulk. Part of this is likely due to the presence of polymer and, consequently, the depletion interaction, pushing the virus against the wall. Also, labelling can change the behaviour of particles, including enhancement in the adherence to glass. At the outer layer of the labelled particle, there is a buildup of the dye's hydrophilic domains, which has a strong interaction with the hydroxyl groups found on the glass surface [110, 111].

The interplay between a few different parameters is related to the structures formed, mainly the viscosity of the system, the depletion interaction, and the polydispersity of the mesogens. Network structures were seen at higher concentrations of Pf4 and lower concentrations of sodium alginate. The concentrations of sodium alginate used in the phase diagram are not high, visibly looking low viscosity (as confirmed in chapter 6). Samples around 10 mg/mL start being visibly more viscous, with the viscosity measurement for the pure polymer 15 mg/mL presented in chapter 6. On the other hand, during the preparation of the sample, it was observed the increase in viscosity of the Pf4 sample with the concentration within the range of the phase diagram.

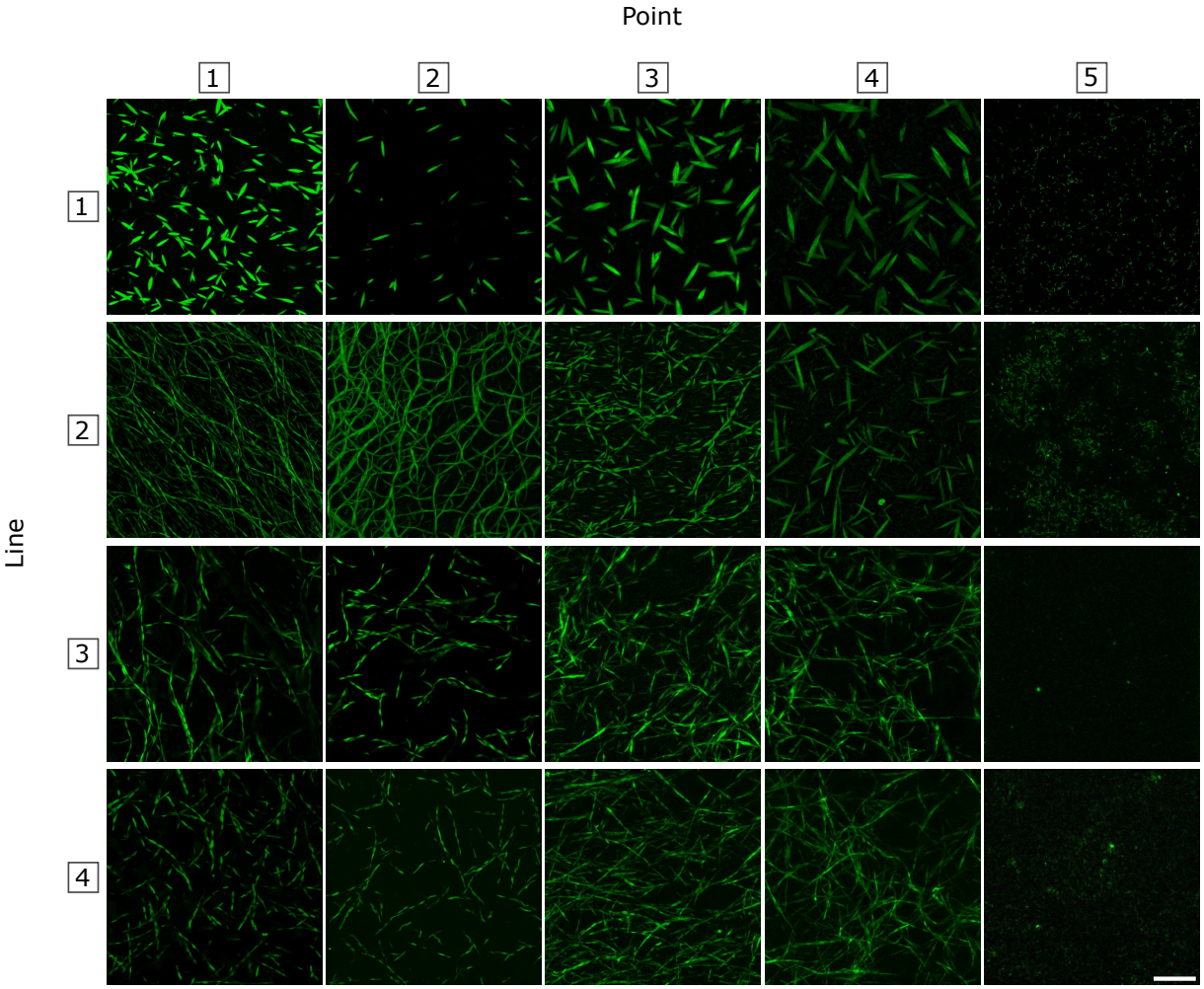


Figure 4.13: Confocal microscope images of the tactoids with different concentrations (for each dilution line), 24 h equilibrating. All images are the same size and the scale bar represents 20 μm.

Furthermore, networks have been observed in other colloidal systems of rod-like particles such as CNC [99], polyamides [72] and clays [100]. The concentration of the components and the polydispersity of the rods were associated with the formation of such structures. A higher concentration of mesogens can result in an arrested state, in which the mobility of the tactoids or bundles is reduced, and networks are formed [72,100]. The filament length was also connected with this state. For longer rods, especially for flexible ones, it is likely they entangle, and form a network, and the system is in a gel-like state, which hinders the phase separation. [21,38]. It has been shown that for samples of F-actin with an average filament bigger than 3 μm, the transition is between a topologically ordered isotropic phase and a weakly aligned nematic. The suppression of rotational diffusion likely prevents long filaments from flipping in the concentrated F-actin [21], and a similar phenomenon is possibly occurring in our system.

The low depletion attraction, high concentration of rods and viscosity of the system, can

help explain why on dilutions lines 3 and 4 only networks are observed, and why at the end of dilution line 2 tactoids were formed. On the other hand, an increase in the concentration of the polymer increases the depletion attraction between the rod-like particles, leading to the formation of tactoids or bundles [72]. This was observed for dilution line 1, in which only tactoids are obtained.

The polydispersity and aspect ratio of the rods are also important parameters. It has been shown in the literature, that when the sample is composed of highly polydisperse rods, there is a large gap in volume fraction between the isotropic and nematic phases. This results in the broadening of the coexisting region, and higher contrast in density and viscosity between the phases. Also, the viscosity of the nematic phase is anisotropic, with the one parallel to the director (direction of the network arm) being similar to the one of the isotropic phase and significantly higher for the viscosity perpendicular to the director. The slower dynamics of the nematic phase and the contrast in density and viscosity result in an arrested state and gelation, with the network being formed [100]. Our sample is significantly polydisperse [51], with this being, probably, an important variable for the formation of the networks we have observed. Furthermore, long rods can allow the formation of tactoids or bundles that can have a common mesogen, resulting in this "continuous line" as shown schematically in figure 4.14.

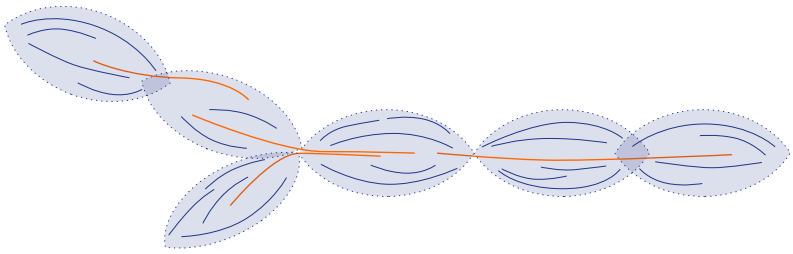


Figure 4.14: Schematic representation of a network, showing in orange longer mesogens in common between different tactoids.

To study the network further, a sample equivalent to the first point of line 4 was imaged after different equilibration times (figure 4.15). The images for each day are from different parts of the capillary, so we can see that the sample is not homogeneous. This can be due to the sample preparation since it is difficult to properly homogenise a small amount of a viscous liquid or it could be due to local interactions. Over time, the networks seem to be assembling into bigger structures. It was not possible to observe any structure after two months, probably because of some contamination in the system (we noticed the presence of microorganisms in the sodium alginate every 2 to 3 months).

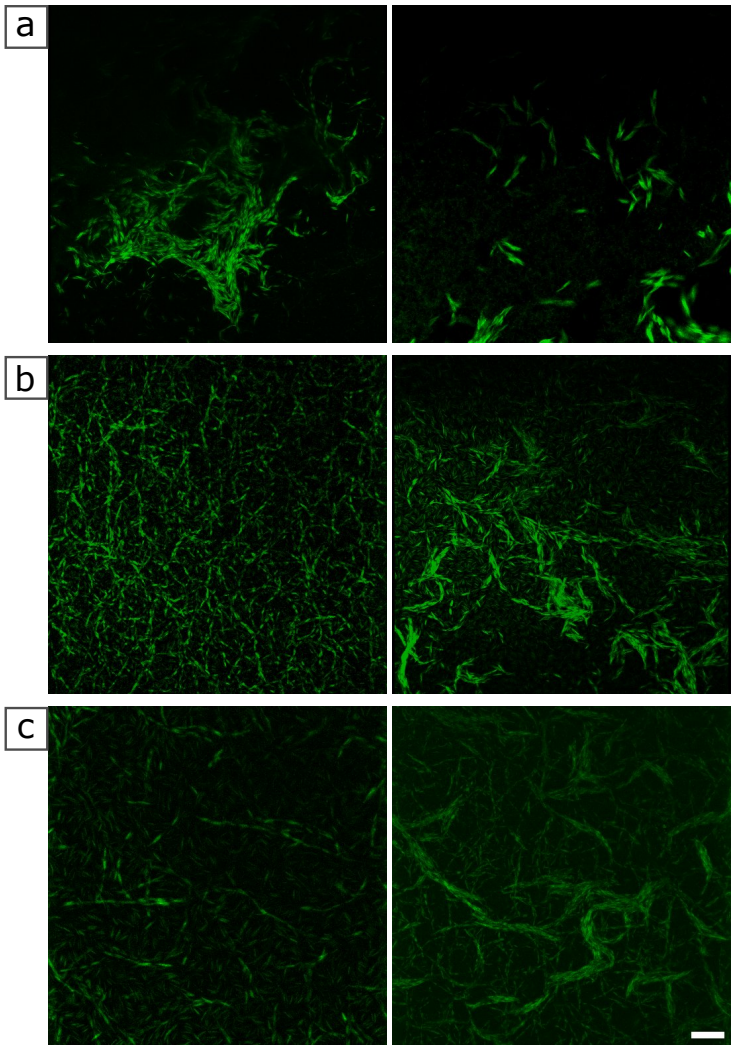


Figure 4.15: Confocal microscope images of the network structures (line 4 pt 1) at different positions (images right and left) and after (a) 17 days, (b) 41 days, and (c) 56 days equilibrating. All images are the same size and the scale bar represents 10 μm.

4.3.4 Theoretical phase diagram

We also calculated the phase diagram using Onsager and free volume theory, which did not consider the polydispersity of the mesogen and polymer nor the charge of the system. Both the virus and polymer are significantly polydisperse, sodium alginate is a polyelectrolyte and PBS has high ionic strength (0.16 M), so the theory does not account for all aspects of the actual system. Here we present three phase diagrams calculated for different values of the aspect ratio and molecular mass of the phage. We always assumed the same molecular mass for the polymer (250 kDa), based on the polydispersity, and the radius of gyration (20 nm) was determined based on [112]. The diameter of the virus used was 6.2 nm since no polydispersity has been observed for this. The length (and consequently aspect ratio) was changed according to some

hypothesis, as explained below, and the mass followed similarly.

First, we assumed all viruses had the full length (3.8 μm) and mass (60.8 MDa), as shown in figure 4.16a. As can be seen, the boundaries obtained are not consistent with the experimental observations, which is expected, considering the actual polydispersity of the mesogens. Then, we the average value for the length (2.68 μm) and decrease the mass proportionally (42.9 MDa). The result agrees more with the experiments than the previous one as shown in figure 4.16b. Last, we used a weighted average for the length and mass of the phage. In the samples used, there were 34 % of ghost filaments, a virus that does not present genetic material and has a smaller length and mass. Considering the average length and mass of the phage and ghost filaments, we obtained a value of 2.16 μmfor the length and 45.6 MDa for the mass. This gives the best agreement with the experiments (figure 4.16c).

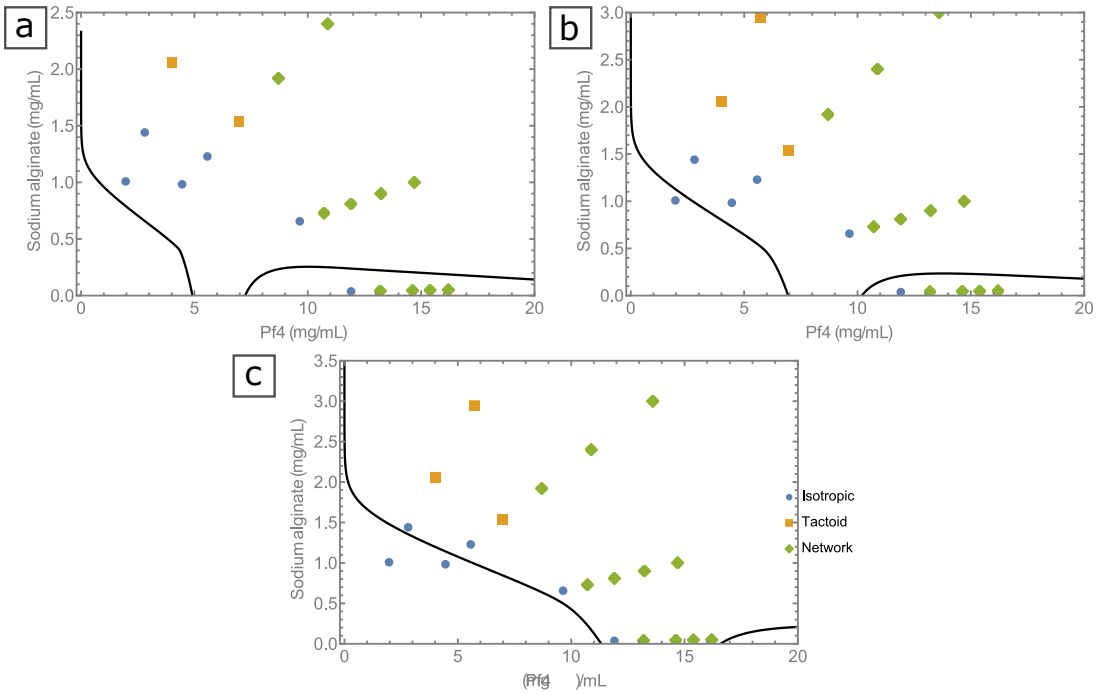


Figure 4.16: Experimental phase diagram with theoretical one (black line) calculated using (a) maximum, (b) average, and (c) weighted average values for the length and mass of the phage.

Considering the assumptions and simplifications made in this model, the agreement between the experiments and theory is good. The theory allows us to estimate the boundaries of the phases and presents the possibility of evaluating how to shift the boundaries (e.g. by having shorter or thicker rods). To consider polydispersity, flexibility and charge in our calculations, we would need to solve more complicated equations. Polydispersity broadens the coexistence region. Charged particles and polymers shift the actual boundaries, and the presence of salt

has an effect since it changes the effective diameter and the radius of gyration [2, 113]. Still, we do not believe there would be a significant benefit, considering the good agreement between the experimental and theoretical phase diagrams.

Besides the approximations and simplifications in our calculations, the actual boundaries of the phase diagram depend on many other experimental variables. Possible virus mutation which can result in changes in size or in the external protein layer. The latter would have an effect on the intermolecular interactions, similar to using labelled or unlabelled viruses or a mixture of the two. The method used for virus isolation, especially considering the one most commonly used is by precipitation through the addition of polymer. This is the method used in our work, where the polymer PEG was employed, possibly resulting in trace amounts of the polymer, even after purification, and affecting the total depletant concentration in the system.

These may help explain the differences seen between this work and the phase diagram presented by Secor *et al.* [50] made using labelled viruses(figure 4.17). We obtained tactoid in regions of high Pf4 concentration and high polymer concentration, where they obtained isotropic. A small region that was biphasic for them was isotropic to us (at the end of dilution line 1). The difference is in a small region, suggesting the general reproducibility of the phase diagram, but still indicative of the importance of the actual batch.

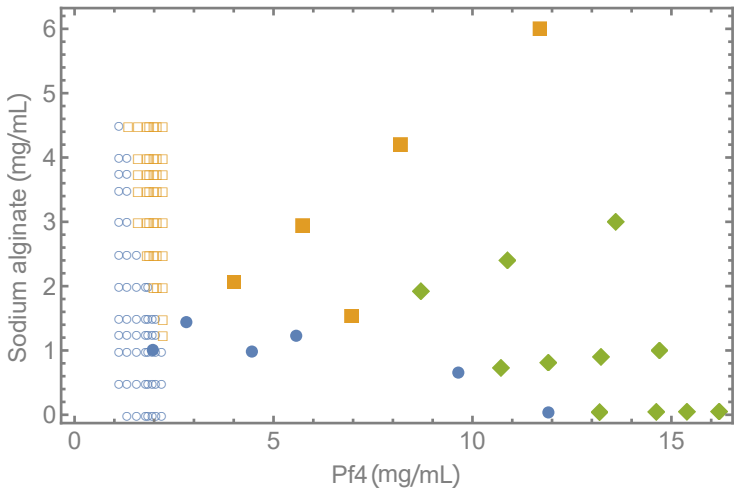


Figure 4.17: Experimental phase diagram with the circular blue dot representing the isotropic phase, the orange squares the tactoids and the green diamond the network structures. Comparison of our results (filled markers) with the ones presented by Secor *et al.* [50] represented here by the empty markers.

4.3.5 Conclusion

In this chapter, we investigated the phase behaviour of tactoids formed by the mixture of rod-like Pf4 phages and biopolymer sodium alginate. We looked at the tactoid growth over time, and the size, finding a relationship of both with the concentration of each component. We also obtained an experimental phase diagram, in which a biphasic region was found and further divided into tactoids and networks. Finally, we also compared to a theoretical phase diagram which allowed us to roughly determine the mono- and biphasic regions.

By following the tactoid growth, we observed that the higher the polymer concentration the quicker the droplets form. At smaller concentrations of polymer, we could see a bright background, probably an isotropic phase, and follow the tactoids formation over the next few hours, until they stabilized at a relatively big size. For the higher concentration, we could not do the same since the droplets formed almost instantaneously. Based on our results and the literature, it is likely that nucleation and growth is the mechanism followed by our system.

The size of the tactoids is greatly dependent on the concentration of sodium alginate, with an inverse relationship. The number density of tactoids in the sample depends on the concentration of Pf4. We noticed an increase in the volume of the tactoid following a decrease in the number of tactoids, indicating they were merging to form bigger droplets. Differently than expected and previously observed, the tactoids' aspect ratio decreased with the increase in volume. For bigger tactoids, we also observed the formation of flower-like arrays, probably related to the fractionation of the mesogens and the presence of long filaments forming a nucleus for the tactoids.

In the experimental phase diagram, we obtained the isotropic phase and a biphasic region (tactoids and network structures). The nematic phase was not seen possibly because of the high concentrations needed for the formation of such phase. The network seems to be formed by small tactoids in continuous lines, probably related to the aspect ratio and/or the polydispersity of the mesogens in the sample. We also obtained a theoretical phase diagram using a simplified model. A weighted average for the virus length and mass gave the best agreement. Considering all the approximations used, the agreement is quite good and can be used to obtain rough boundaries for the phase diagram.

By investigating the phase behaviour of the tactoids, we were able to correlate it with

other mesogens well known in the literature and to draw a picture of the main properties of the system. Some differences were observed in this work from previous ones done in the group and the literature, which may be related to the batch used. Differences in the isolation, aspect ratio and polydispersity of the phase can have a big impact on the timescale, size, and actual boundary of the phase diagram. Still, our results helped us understand better the behaviour of the tactoids, seeing differences in size, growth time and phase formation with the concentration of each component. These results will be useful when exploring their relationship with impurities (chapter 5).

Acknowledgments

We would like to thank Dr Abul Tarafder for the preparation of the Pf4.

Chapter 5

The effect of impurities on the behaviour of Pf4 tactoids

Abstract

In this chapter, we investigated the interaction of tactoids with a rod as an impurity. Four different configurations were found and classified as no attachment, partial attachment, sandwich and encapsulation. We presented the results with the bacteria *B. subtilis* and *E. coli*, and with synthetic rods (SU8 and silica). We evaluated the effects of surface properties and geometry connected with each configuration and with the absence of encapsulation for *B. subtilis* and silica rods. We found a relationship between the length of the tactoid and the length of the rod and the aspect ratio of the rod itself for encapsulation to be obtained. To help us understand this problem, we explored the system theoretically, first by looking exclusively at the elastic energy of the encapsulated configuration, and later by looking at all energy components of a free boundary tactoid. Using the second model, we obtained all the states seen empirically. We further noticed that the rod preferred to be close to the tip of the tactoid, so the proximity of the defects minimized the energy of the system, with high aspect ratio rods having a smaller energetic cost. Finally, we noticed that having a quasi-2D setup altered the system and encapsulation was obtained for all the impurities evaluated.

5.1 Introduction

P. aeruginosa is the main pathogen responsible for the morbidity and mortality of patients with cystic fibrosis (CF) and may cause severe infections in patients with a compromised immune system [53]. Upon antimicrobial treatment, the pathogen may become resistant to antibiotics by forming biofilms [114], within which the bacteria can produce different components. For *P. aeruginosa*, it has been shown that Pf phage production is upregulated [56–58] and Pf4 has a symbiotic relationship in this bacteria's biofilms. [50]

In the presence of a non-adsorbing polymer, such as alginate produced by the bacteria, the depletion effect facilitates a phase separation into a phase rich in virus particles (nematic phase) in coexistence with a phase poor in virus particles (isotropic phase). It was shown that the formation of nematic droplets, called tactoids, protect *P. aeruginosa* against antibiotics [50], and later this was attributed to these tactoids tendency to encapsulate the bacterial cells. In the presence of just one of the components (either Pf4 or the polymer sodium alginate), the cells are not more tolerant to antibiotics, suggesting that the presence of virus particles forming tactoids is necessary for this protection. [51]

Such liquid crystalline phase behaviour displayed by mixtures of virus particles and polymer is well-known for certain viruses and was the topic of chapter 4. The shape and director field of a tactoid depends on the competition between the elastic properties of the nematic phase, the surface tension between the isotropic and the nematic phase, and the anchoring strength at the IN interface [39, 40]. The values of the elasticity, surface, and anchoring terms, are functions of the length, aspect ratio, and stiffness of the elongated particles [18, 115]. In addition, they will depend on the polymer concentration [116–118], and the ionic strength of the dispersion [119], further complicated by using a polyelectrolyte such as alginate [66].

In this work, we introduce a third body to the dispersion of virus particles and polymer. We have used two different types of bacteria (gram-positive and gram-negative) as well as synthetic rod-shaped particles. From this point onwards we will refer to this third body either as bacteria or as rods. We will take care to refer to rod-like virus particles as virus particles or viruses. The introduction of a third species further complicates the physics and brings with it the surface tension between the rod and the isotropic or nematic phase, as well as an anchoring term between the rod and the nematic phase. We have identified four different states (Figure 5.1)

when studying the mixture of virus, polymer, and rod: (i) no attachment when the rods and tactoids do not interact and remain separated; (ii) partial attachment if the outside of one tactoid attaches to one of the long sides of the rod; (iii) a sandwich state when the outside of two tactoids attach to the same rod; and (iv) encapsulation if the majority of the rod is inside a tactoid.

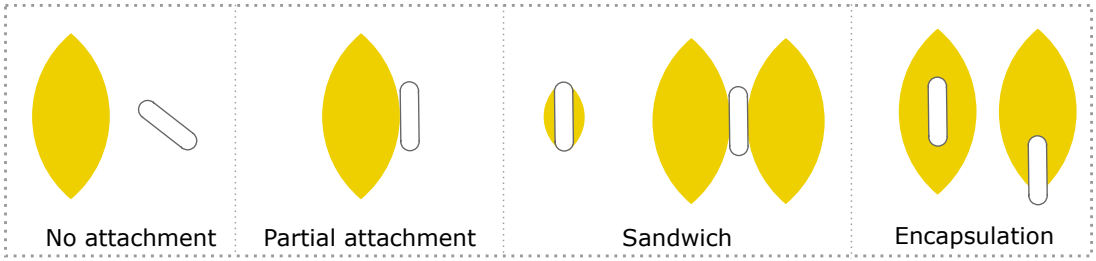


Figure 5.1: Schematic of assigned configurations, experimentally observed, of the rod (in white) and the nematic droplet, or tactoid (in yellow) behaviour

We aim to categorize and understand these different configurations. To this end, we have performed a range of experiments, on different bacterial rods as well as on different colloidal model rods, all mixed with Pf4 virus and sodium alginate polymer. We begin by presenting the experimental system (section 5.2). The number of competing terms further suggest a theoretical (simulational) approach to scan the parameter space, and we used a model considering the elastic energy in section 5.3.1 and a more complete free boundary model in section 5.3.2. We then introduce the experimental results, first by presenting the bacterial rods (section 5.4.1), in which model organisms of the two main domains of bacteria membranes, *E. coli* (gram-), and *B. subtilis* (gram+) were used. This is followed by the results with synthetic rods (section 5.4.2), namely silica and SU8 rods, which allowed us to explore the effect of surface properties and made it easier to vary the size and aspect ratio of the rods. Finally, we end the experimental results by looking at the effect of surface modification on silica rods (section 5.4.3). Subsequently, the two different numerical analyses are discussed to shed some light on the experimental observations (sections 5.4.4 and 5.4.5). We finish the chapter with the results of experiments done in quasi-2D set-up (section 5.4.6) and with conclusions and outlook in section 5.5.

5.2 Experimental Method

The experiments were done using the Pf4 isolated and purified as described in section 2.2.1, tactoids prepared as explained in section 2.2.4, bacteria as described in section 2.2.3 and the

synthetic rods and their modifications as in sections 2.2.2, 3.3.5, and 3.3.3. Table 5.1 shows the size and zeta potential of all the rods used here and of *P. aeruginosa* for comparison. Here we will briefly summarize how the experiments presented in this chapter were done.

Table 5.1: Size and zeta potential of synthetic rods and bacteria used in the work.

Rod	Length (µm)	Diameter (µm)	Zeta potential (mV)
Thick	2.43 ± 0.26	0.98 ± 0.06	-13.9
Thin	1.67 ± 0.20	0.41 ± 0.06	-12.1
SU8	3.7 ± 1.6	0.52 ± 0.17	-1.4
P. aeruginosa	1 to 5 [120]	0.5 to 1 [120]	-7 to -12 [121, 122]
E. coli	1.5 to 1.9 [123]	0.6 to 1 [123]	-22 to -48 [123–125]
B. subtilis	2 to 6 [126]	<1 [126]	-17 to -34 [124, 125]

The rods were mixed with the labelled virus for a final concentration of 1 mg/mL Pf4 and posteriorly with the sodium alginate at a concentration ranging from 2 to 5 mg/mL. Because the size of the tactoids depends highly on the concentration of the biopolymer and on the time after preparation, different concentrations and equilibration times were used to allow multiple sizes of tactoid to be obtained. After adding all the components in a vial, the mixture was vortexed for 5 min and then the sample was placed in the square capillary and sealed with epoxy glue, fixed to a glass slide (figure 2.2b).

For the 2D experiments, a similar procedure was followed, but after vortexing the mixture, the samples were left equilibrating in the vial. After, an aliquot was put in an agar pad and covered with a glass slide (quasi-2D system). A cover was added to avoid water evaporation from the agar (figure 2.2c).

Once the samples had equilibrated, the system was imaged using a Zeiss LSM Exciter 5 (Confocal Laser Scanning Microscope) with a 63x objective.

5.3 Theoretical background

5.3.1 Elastic energy of tactoid

The calculation for the tactoids was based on the work done by Lewis *et al.* for the nematic phase in rectangular confinement [29]. It was done assuming a 2D tactoid with a fixed circular or spindle-like shape, described by the intersection of two congruent circles and centred at the

opposite shift value in the x-axis. The radius and shift in the x-axis (s_x) were determined based on the aspect ratio and area desired.

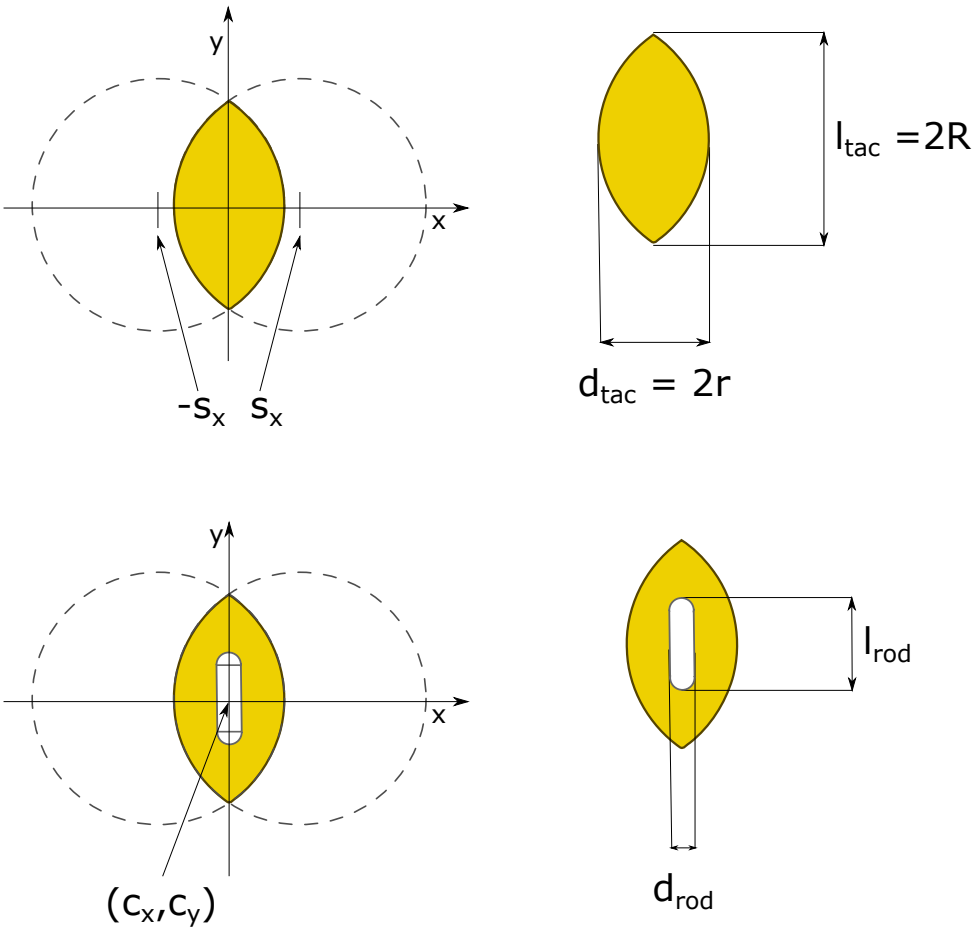


Figure 5.2: Schematic representation of the spindle-like domain used.

For this 2D system, the director (see figure 1.2) can be expressed as a unit vector in the xy-plane by

$$\mathbf{n} = \begin{cases} \cos(\theta(x,y)), \\ \sin(\theta(x,y)). \end{cases} \tag{5.1}$$

The Oseen-Frank energy can be written in terms of θ as

$$E[\theta] = \frac{K_3}{2} \iint_\Omega |\nabla\theta|^2 - \delta(\theta_y \cos\theta - \theta_x \sin\theta)^2 \, d\Omega, \tag{5.2}$$

where $\delta = 1 - K_1/K_3$, and K_1 and K_3 are the elastic constants for splay and bend, respectively, as described in section 1.2.3. This expression can be further simplified using the one constant

approximation to

$$E[\theta] = \frac{K}{2} \iint_{\Omega} |\nabla\theta|^2 d\Omega. \tag{5.3}$$

Minimizing eq. (5.2), we obtain the Euler-Lagrange equation

$$\nabla^2\theta + \delta \left(\frac{1}{2} \sin 2\theta(\theta_y^2 + 2\theta_x y - \theta_x^2) + \theta_x\theta_y \cos 2\theta - \theta_{xx} \sin^2\theta - \theta_{yy} \cos^2\theta \right) = 0, \tag{5.4}$$

whereas for the one constant approximation, the minimization of equation 5.3, results in the Laplace equation

$$\nabla^2\theta = 0. \tag{5.5}$$

Equation (5.5) can be solved analytically, however, this is not the case for eq. (5.4). So, we decided to solve all the equations numerically using the software COMSOL. We assumed the director was bipolar with the boojums (point defects of the bipolar field - figure 1.7) at the tip, using the boundary conditions shown in eq. (5.6).

$$\theta = \begin{cases} \arctan\left(\dfrac{y}{x + s_x}\right) + \dfrac{\pi}{2} & \text{for right side} \\ \arctan\left(\dfrac{y}{x - s_x}\right) + \dfrac{\pi}{2} & \text{for left side} \end{cases} \tag{5.6}$$

When using strong anchoring (Dirichlet boundary conditions) θ is discontinuous at each tip of the tactoid, creating a point defect with infinite energy. The simplest way to deal with these defects is to create a regularized domain (figure 5.3), in which a circle of radius ϵ, smaller than the correlation length, and centred at the point defect, is eliminated from the energy calculation. In our case, we used $\epsilon = 0.005$. This value was chosen based on the literature [29], which is proportional to the nematic correlation length. We solved the equation for the entire tactoid and then obtained the energy for the regularized domain using eq. (5.3), obtaining what we called regularized energy.

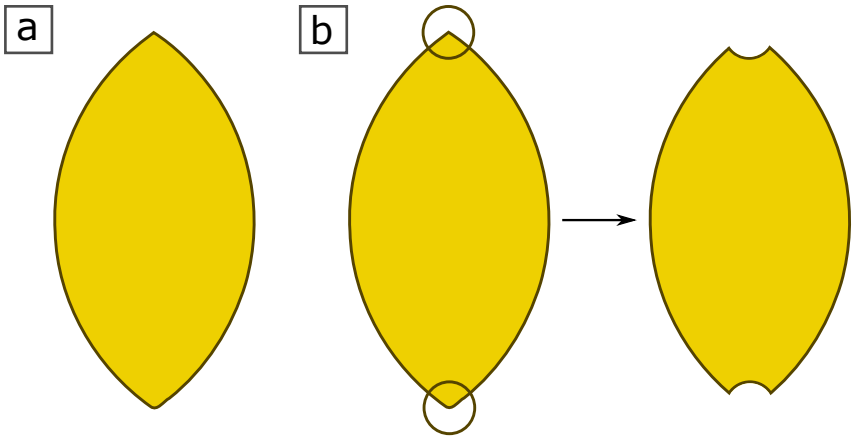


Figure 5.3: (a) Domain used in the calculation of the tactoid director and (b) elimination of a circle around the defect on the tactoid tip, resulting in the regularized domain, used in the calculation of energy (then called regularized energy).

We then added a spherocylindrical rod (similar shape to the bacteria) in the centre of the tactoid. We assumed strong anchoring at the surface of the rod, using the Dirichlet boundary conditions:

$$\theta = \begin{cases} \arctan\left(\dfrac{y - l_{rod}/2 - cy}{x} + \dfrac{\pi}{2}\right) & \text{top,} \\ \arctan\left(\dfrac{y + l_{rod}/2 - cy}{x} + \dfrac{\pi}{2}\right) & \text{bottom,} \\ \dfrac{\pi}{2} & \text{sides.} \end{cases} \tag{5.7}$$

The addition of rods with strong anchoring, adds two other defects at the tip of the rods. The same idea of regularized energy was applied here.

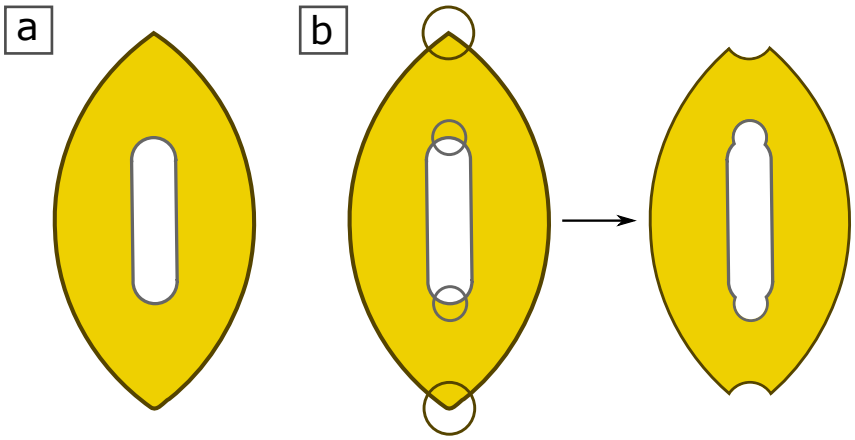


Figure 5.4: (a) Domain used in the calculation of the tactoid director in the presence of a rod and (b) elimination of a circle around the defect on the tactoid tip, resulting in the regularized domain, used in the calculation of energy (then called regularized energy).

5.3.2 Free boundary numerical model

This theory and the subsequent calculations were done by Dr Yucen Han, Prof Apala Majumdar (Department of Mathematics and Statistics, University of Strathclyde, United Kingdom) and Prof Lei Zhang (Beijing International Center for Mathematical Research, Peking University, China).

We describe the mixture of Pf4 virus and alginate without a rod within a Ginzburg–Landau free energy [127]. The two macroscopic order parameters to describe the system are the angle θ and the scalar parameter s. The θ is the angle of unit vector $\mathbf{n} = (\cos\theta, \sin\theta)$ as before and s is a measure of the density, with $s \approx 1$ corresponding to the nematic phase and $s \approx 0$ the isotropic phase.

The energy density of the Ginzburgh–Landau free energy is as follows,

$$f(s,\theta) = f_l + f_{bulk} + f_{el} + f_{anch}. \tag{5.8}$$

where

$$f_l = \frac{\sigma_c}{2}|\nabla s|^2, \tag{5.9}$$

$$f_{bulk} = \frac{\sigma_c}{4\epsilon_c^2}s^2(s-1)^2, \tag{5.10}$$

$$f_{el} = \frac{K_c}{2}s^2|\nabla\theta|^2, \tag{5.11}$$

$$f_{anch} = \frac{A_c}{2}\left((\cos\theta, \sin\theta)\cdot\nabla s\right)^2. \tag{5.12}$$

We model the system in 2D. The energy density f_l describes the energy of the interface between nematic and isotropic phases, which, in our 2D model, is proportional to the line tension. In eq. (5.9) and eq. (5.10), σ_c is the mixing energy density constant. The bulk energy density f_{bulk} is given by a double-well potential of equal depth, which drives the phase separation between the nematics and isotropic phases. The parameter ϵ_c is the interface width. The elastic energy density f_{el} is the simplest form of Oseen–Frank energy density for the nematics phase within the one-constant approximation, in which K_c is the elastic constant. The planar anchoring energy density f_{anch} forces the director to lie along the interface, where A_c is the anchoring strength.

The free energy terms can be nondimensionalized as

$$\tilde{\mathbf{x}} = \mathbf{x}/L_c, \sigma = \sigma_c L_c/E_c,\ \epsilon = \epsilon_c/L_c,\ K = K_c L_c/E_c,\ A = A_c L_c/E_c. \tag{5.13}$$

where L_c is a characteristic length scale, and E_c is a characteristic energy scale. Then we can write the energy densities in dimensionless form as

$$\tilde{f_l} = \frac{\sigma}{2}|\tilde{\nabla} s|^2, \tag{5.14}$$

$$\tilde{f}_{bulk} = \frac{\lambda}{4} s^2 (s-1)^2, \tag{5.15}$$

$$\tilde{f}_{el} = \frac{K}{2} s^2 |\tilde{\nabla}\theta|^2, \tag{5.16}$$

$$\tilde{f}_{anch} = \frac{A}{2}\left((\cos\theta, \sin\theta)\cdot\tilde{\nabla} s\right)^2, \tag{5.17}$$

where $\lambda = \sigma/\epsilon^2$. We choose the dimensionless parameters $\sigma = 1$, $\lambda = 10^5$, $K = 20$, and $A = 20$, and this is at present, a phenomenological choice. In the following, we drop the tilde for ease of notation.

This model derives from the one in [128]. We change the vector order parameter $\mathbf{n}$ into the angle θ to avoid the additional constraint for unit length on $\mathbf{n}$, and change the linearity of s into quadratic form in eq. (5.16), which avoids s to be negative. The choices of parameters σ, K, and A play an important role in the shape of the tactoid. The paper [129] analysed the competition between elastic and surface energies in three limiting choices.

Next, we model the spherocylindrical impurity. The rod is a 2D spherocylinder, which is composed of a rectangle with length l and capped by two semicircles with diameter h. The rod is fixed at the centre of the box. The simulation is performed with periodic boundary conditions. The boundary of rod $\partial\Omega_{rod}$ can be separated by three parts, the long straight edges of rod $\partial\Omega_l = \{y = \pm l/2\} \cap \partial\Omega_{rod}$, left semicircle $\partial\Omega_{Lsc} = \partial\Omega_{rod} \backslash \partial\Omega_l \cap \{x < 0\}$, and right semicircle $\partial\Omega_{Rsc} = \partial\Omega_{rod} \backslash \partial\Omega_l \cap \{x > 0\}$. According to the experimental results in [51], Pf4 phages are observed to be degenerate planar anchoring (similar to [29]), also referred as tangential anchoring, so we impose the tangential Dirichlet boundary condition for θ on $\partial\Omega_{rod}$

as

$$\theta = \begin{cases} 0 & \partial\Omega_l, \\ arctan(-(x+l/2)/y) & \partial\Omega_{Lsc}, \\ arctan(-(x-l/2)/y) & \partial\Omega_{Rsc}, \end{cases} \tag{5.18}$$

and natural boundary conditions for s on two ends of the rod

$$\frac{\partial s}{\partial \mathbf{v}} = 0,\ \partial\Omega_{Lsc} \cup \partial\Omega_{Rsc}, \tag{5.19}$$

where $\mathbf{v}$ is the normal vector of a boundary.

The remaining boundary condition to be imposed is for s on the two straight edges of bacteria $\partial\Omega_l$. We add a surface anchoring potential between the nematic phase and rod as follows

$$\int_{\partial\Omega_l} W_l(s-1)^2 \mathrm{dS}. \tag{5.20}$$

The non-dimensional parameter $W_l = W_{cl}L_c^2/E_c$, where W_{cl} is the physical anchoring strength between the rod and nematic phase. W_l can be tuned to achieve different boundary conditions. $W_l = 0$ indicates natural boundary condition, and as $W_l \to \infty$, the minimizer of the free energy functional converges to the solution with Dirichlet(strong) boundary condition with $s = 1$ on $\partial\Omega_l$. If W_l is finite but larger than zero, we are in the weak anchoring regime.

We assume s has mass conservation, and, hence, the dynamics of s is supposed to be driven by energy minimization with mass conservation, and the dynamics of θ by energy minimization only. We couple the system with a Cahn–Hilliard equation [130] governing the dynamics of order parameter s, and an Allen-Cahn equation [131, 132] for the direction of nematics θ.

We use a backward Euler scheme for s and a forward Euler scheme for θ scheme with a stabilizer on temporal direction as in [128]. The time-step is set to $\Delta t = 1e-3$, and stabilizer coefficients $\alpha = 1e1$, $\beta = 2e1$. For spatial discretization, we use the Finite Element Method with a Newton solver in FEniCS package [133]. We introduce a new variable $\mu = -\sigma\Delta s + \frac{\lambda}{2}s(s-1)(2s-1) + Ks|\nabla\theta|^2 - W\nabla\cdot\{(\cos\theta,\sin\theta)\cdot\nabla s(\cos\theta,\sin\theta)\}$ in order to turn the equation into a second order partial differential equation. Lagrange elements of order 1 are used for the spatial discretization on a domain Ω with mesh size $h < \frac{1}{256}$. The tolerance in every temporal

iteration is set to $1e-13$. We stop calculating if the energy difference of the solutions between two consecutive iterations is less than $1e-5$.

5.4 Results and Discussion

In this section, we will first present the experimental results for the bacteria, *E. coli* and *B. subtilis*, followed by the synthetic colloidal rods, silica and SU8. Next, we will qualitatively show the results for the silica rods with surface modification. We will then present the results from the numerical calculations considering only the elastic energy and, subsequently, considering all energy components of the system. In the last subsection, we will present the results in a quasi-2D set-up.

5.4.1 Experiments with bacteria

The experiments described in this subsection were done by Dr Iago Grobas.

The interaction between rod-shaped bacteria and tactoids made of Pf4 viruses has previously been studied for *P. aeruginosa* [51], where the nematic phase was found to surround the cells. Electron microscopy images showed that the virus was close to the outer membrane of the bacteria, which would be expected - as explained in the introduction the depletion interaction mediated by the alginate polymer pushed the virus against the bacterium. To assess if the type of bacterial membrane plays a role in this phenomenon we used the model organisms for the two major forms of bacterial membranes: *E. coli* for gram - and *B. subtilis* for gram +.

The previously studied *P. aeruginosa* is gram -, as is *E. coli*, so their cell membranes share similar constructions [134], and we only focus on the model bacteria in this work. Figure 5.5 (a-c) presents typical confocal images for each of the identified configurations for *E. coli*. These are subsequently categorized by hand into the four configurations described in section 5.1, which allows obtaining the distribution of the three configurations where there is contact between the tactoid and bacterium. As can be seen from the distribution plot, the partial attachment is most commonly observed, followed by the sandwich state, and finally, the encapsulation, see figure 5.5 f.

A distribution of states was not presented in Tarafder *et al.* for *P. aeruginosa* [51], but

it is possible to observe a high recurrence of encapsulation. One possible explanation for this difference is the lipopolysaccharide (LPS) - the molecule that covers 75 % of the area of the outermost part of the bacterial membrane [135] - since the composition of this molecule is dependent on multiple factors, including species [136,137]. This distinction can result in different surface morphology and intermolecular interactions, in turn affecting the anchoring orientation and strength [19]. Another possible explanation will be discussed in section 5.4.6 and relates to differences in the experimental setup.

To further determine whether the configurations seen so far are specific to the gram - cell membrane, we repeated the experiments with *B. subtilis* (figure 5.5 d,e). Their cell wall does not have the outer membrane formed by LPS, thus ending in peptidoglycan, which has a different molecular assembly and chemical composition [134], probably affecting the anchoring with the bacteria wall. Partial attachment was again the most common state, followed by the sandwich state (figure 5.5 f). Encapsulation was not observed. These results demonstrate that surface interactions play an important role, but are not the only parameters since the predominant state is the same for both gram - and gram +. This points in the direction of the experiments presented in the next section, where the interaction with inert colloidal rods is presented.

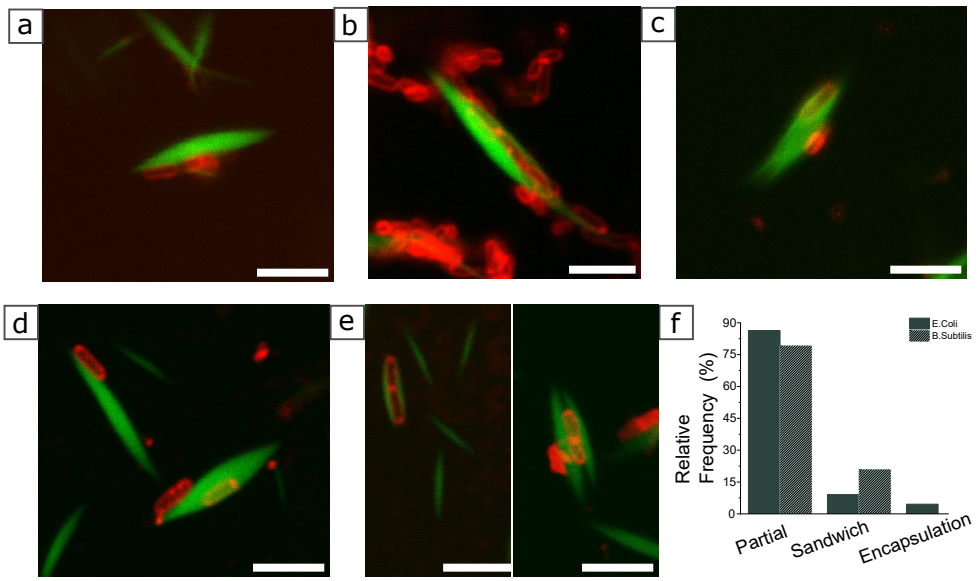


Figure 5.5: Configurations obtained for the bacteria. Confocal microscopy images of bacteria, in red, (a,b,c) *E. coli* and (d,e) *B. subtilis*, and their different interactions with the Pf4 tactoids,in green, (a,d) partial attachment, (b,e) sandwich and (c) encapsulation; (f) histogram of the states observed. All the images are the same size and the scale bar is 5 μm.

5.4.2 Experiments with synthetic rods

The experiments described in this subsection were done in collaboration with Dr Iago Grobas.

As explained in sections 3.3.3 and 2.2.2, we synthesized rods made of silica and SU8 with a spherocylindrical shape and similar size to the bacteria to address surface and geometry properties. The two materials used are negatively charged, but SU8 is hydrophobic [138] while silica is hydrophilic [90].

For both rods we observed no attachment, partial attachment, and the sandwich state; encapsulation was only observed for SU8 rods (figure 5.6 a-e). Partial attachment and sandwich were seen in similar frequencies for both materials, with the former being the most common configuration (figure 5.6 f). This indicates that these synthetic rods can successfully replicate the interaction observed in the bacterial system. It also indicates that multiple surface properties are at play. Silica rods wettability and zeta potential are more similar to the *P. aeruginosa* bacteria than SU8 rods, but no encapsulation is observed for the former synthetic rods.

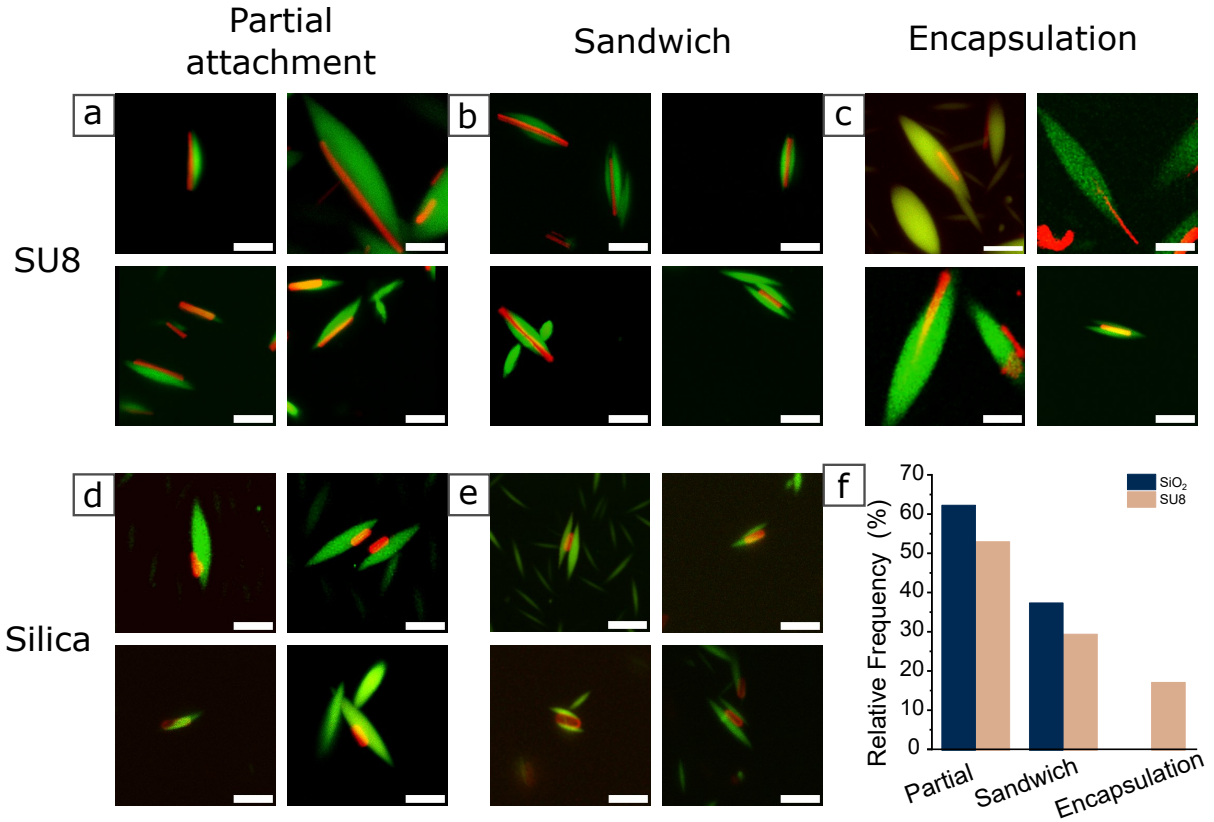


Figure 5.6: Configurations obtained for the synthetic rods. Confocal microscope images of (a,b,c) SU8 and (d,e) silica rods, in red, interacting with Pf4 tactoid, in green, (a,d) partial attachment, (b,e) sandwich and (c) encapsulation; (f) histogram of the states observed. All the images are the same size and the scale bar is 5 μm.

Furthermore, the rods did not always attach to the middle of the tactoids, and especially for encapsulation, it is common to see rods at the tip. In the sandwich configuration, when a rod is of similar size to the tactoids, the individual tactoids are seen to wet the rods, i.e. the tactoid seems to spread on the colloidal surface. This means that they lose the curvature in half of the droplet, maintaining a straight interface in contact with the side of the rod. This was observed more frequently for the SU8 rods, possibly because they are generally longer than the silica rods, but equally have different surface properties.

Since a range of states is possible for each type of rod (both for the synthetic rods and for the bacterial rods), other properties are important in determining the interaction between the rod and the tactoid. We, therefore, analysed the data in terms of geometrical parameters: from the confocal images, we calculated the ratio between the length of the rod and the length of the tactoid ($r_{\mathrm{rt}} = l_{\mathrm{rod}}/l_{\mathrm{tactoid}}$). This is plotted against the type of configuration in figure 5.7 a. In the case of partial attachments, the average and standard deviation of the ratio r_{rt} for both materials are nearly identical. For the sandwich state, the averages of the ratio for each material are nearly double the ones for partial attachment; in the case of SU8, the standard deviation is also much larger. The larger ratios indicate that rods tend to get sandwiched when their size is comparable to the length of the tactoid.

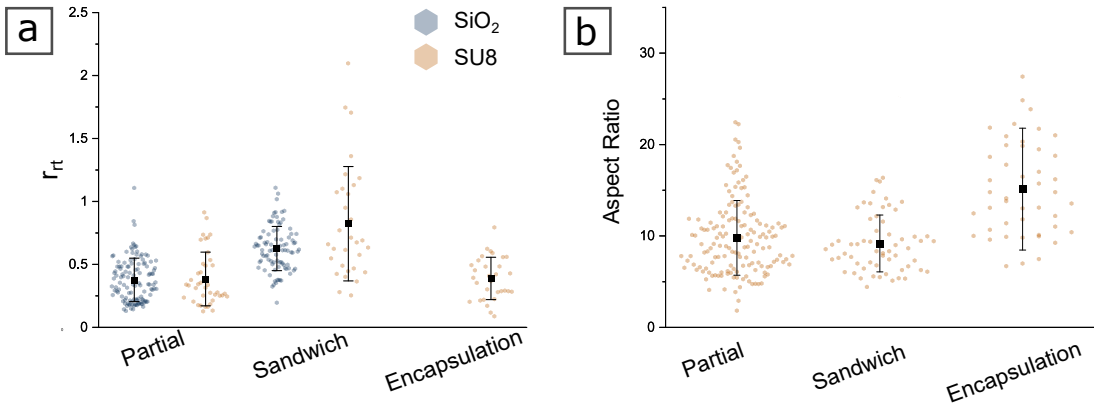


Figure 5.7: Effect of the rod-tactoid dimensions in the type of configuration obtained experimentally. Column scatters distribution of the configurations obtained experimentally relating (a) the ratio of the length of the rod by the length of the tactoid (avg ratios ± sd) and (b) the aspect ratio (length by diameter) of the SU8 rods (avg ratios ± sd).

The data for encapsulation is similar in average and standard deviation as those for partial attachment. Since encapsulation happens only for SU8, we also looked at the size of the actual rods and found that this configuration happens for particles with larger aspect ratios ($l_{\mathrm{rod}}/d_{\mathrm{rod}}$),

with an average of 15, as shown in figure 5.7 b, as well as for longer tactoids. For a given tactoid size, the defects at the tips of the rod and the tips of the tactoid will be closer together for a longer rod, which is elastically favourable. If one end of the rod is at the tip of the tactoid or even sticks out the elastic penalty is even smaller.

To check whether silica rods with a higher aspect ratio (i.e. thin rods) would get encapsulated, new silica rods were synthesized and mixed with tactoids as shown in figure 5.8. The most common state observed was still partial attachment with a preference for the rod to go to the tip of the tactoid. The average aspect ratio of these silica rods was 3.75 times smaller than the average for the SU8 rods that were encapsulated, and we did not observe the encapsulated state for silica rods; we note that higher aspect ratio spherocylindrical silica rods are difficult to synthesize. Furthermore, the aspect ratio of SU8 rods is much larger than the aspect ratio of the bacteria (table 5.1), again highlighting that a combination of surface properties and geometry determines the occurrence of the different states.

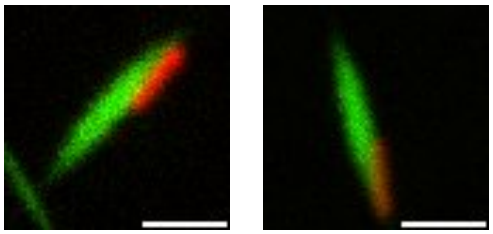


Figure 5.8: Confocal microscope images of high aspect ratio (thin) silica rods (in red) interacting with Pf4 tactoids (in green). Only partial attachment was observed with a slight preference for the rods to attach at the tip of the tactoid rather than at the middle. All the images are the same size and the scale bar is 2 μm.

5.4.3 Experiments with surface modified silica rods

Different surface modifications were done on the silica rods to investigate if different surface properties may be responsible for the configurations seen. The results of these modifications are presented in figure 5.9, and more hydrophobic or positively charged silica rods were obtained. We will show just the qualitative results for these rods since no significant changes were observed in comparison with the pure silica rods. Sandwich, no attachment and partial attachment were seen, but again encapsulation was not observed.

Previous results in the literature indicate that electrostatic forces are an important factor in the interaction of viruses with substrates. In particular, a study has looked at viruses with

silica surfaces, and noticed that viruses in a medium with pH above their isoelectric point (pI) - negatively charged surface - adsorbed exclusively to positively charged silica surfaces. When close to the isoelectric point, they adsorbed to any charged surface, but to a smaller magnitude [139]. The pI for Pf4 is not known, but the zeta potential in PBS is negative, so we evaluated if a positive surface modified with 3-aminopropyltriethoxysilane (APTS) would result in different configurations. No significant qualitative changes in the configurations were observed and encapsulation was not obtained.

Since electrostatic forces did not have an influence, we evaluated the wettability (surface tension), specifically hydrophobic surfaces, considering that the SU8 rods got encapsulated. We used two different silanes since it has been shown in the literature that Hexamethyldisilazane (HDMS) produces particles that are more hydrophobic than Trimethylsilyl chloride (TMSCl) for the same conditions used [94]. Characterizing the wettability of particles is challenging, so we did a qualitative test shown in figure 3.10. We know the particles are hydrophobic, but not the magnitude, making it difficult to compare the wettability of these particles with the SU8 rods. However, we also obtained different zeta potentials for them (table 3.2), with HDMS modification resulting in a charge similar to the pure rod and TMSCl being almost neutral. Again, no differences were observed compared to the hydrophilic silica rods.

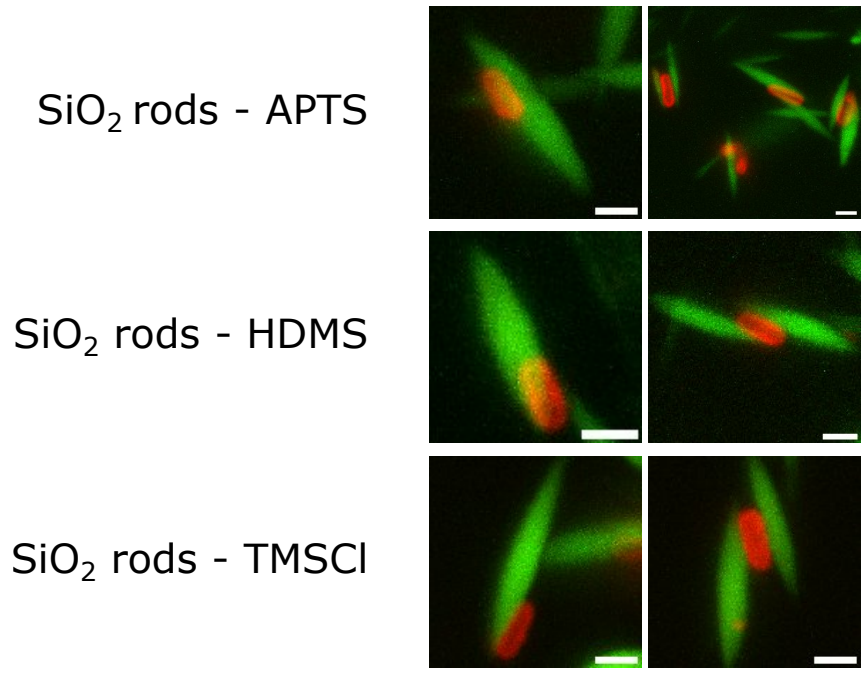


Figure 5.9: Confocal microscope images for the suspension with rods modified with (a) APTS, (b) HDMS and (c) TMSCl. All the images are the same size and the scale bar is 2 μm.

Zeta potential and wettability are two surface properties that we investigated. However, anchoring depends on more parameters, such as surface topography. Silica rods are porous (figure 3.8), and the new layers from the surface modification are more likely rough, which may affect how the virus interacts with the surface. Further investigation and characterization of the surfaces are necessary, but it is clear that for synthetic rods, geometry plays an important role. We explore this topic further using theory in the next sessions.

5.4.4 Elastic energy calculations

The shape and director of tactoids by themselves have been extensively studied in the literature [39, 40, 44]. However, our focus was to analyse the effect of the addition of a rod. We started with a model, looking just at the elastic energy of a fixed-shape tactoid. At the tip of the tactoid, the director changes discontinuously, creating a defect of infinity energy, so we calculated the regularized energy as explained in 1.2.4 and in Lewis *et al.* [29]. Using the one constant approximation, we looked at how the elastic energy changes with the aspect ratio for a tactoid of constant area. The larger the aspect ratio of the tactoid, the smaller the energy, as shown in figure 5.10. This was expected since when the size of a tactoid increases, the ratio decreases and the area parameters dominate. For a bipolar tactoid, the longer the tactoid the less the director changes, so the smaller the elastic cost [39].

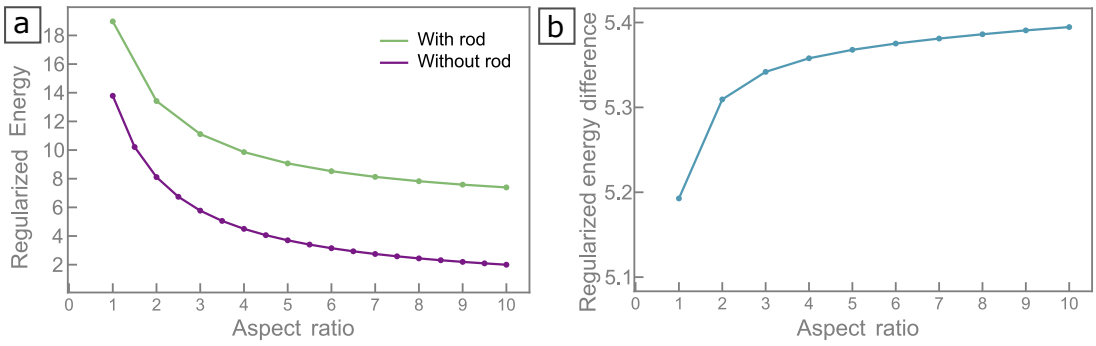


Figure 5.10: (a) Regularized energy and (b) difference of energy of the tactoid (length=0.5 and diameter = 0.05) per aspect ratio with and without the addition of the rod.

We then performed the same calculation for a tactoid with the insertion of a rod, assuming strong homogeneous anchoring with the rod surface. At the rod's tip, the director is discontinuous and creates a point defect similar to the one observed at the tip of the tactoid. Again, we

used the regularised energy and as we can see in figure 5.10, a similar trend as the one before is followed - the energy decreases with the increase in tactoid aspect ratio. Compared with the tactoid alone, we see the energy increases due to this addition, related to the cost for the director change from the uniform field around the rod and the addition of a point defect in the tip of the rod. The cost of inserting the rod increases with the aspect ratio, being almost 4 % higher for ratio 10 than for ratio 1 (figure 5.10 b).

Then, we evaluated the effect of changing the rod size, first by changing the length while keeping the diameter constant. Considering the different lengths of the tactoids for different ratios and the relationship found between the ratio of the rod with the tactoid, we calculated the regularized energy depending on $r_{\mathrm{rt}} = l_{\mathrm{rod}}/l_{\mathrm{tactoid}}$. In figure 5.11, it is possible to see mainly a decrease in energy with the increase in the rod's length. The energy change is small, so the increase in the length does not compensate for the energetic cost of adding the rod for different ratios. The decrease in energy for longer rods is probably associated with the defects since they get closer; the defect in the tip of the tactoid is positive while in the tip of the rod is negative, thus they attract each other and minimize the change in the director.

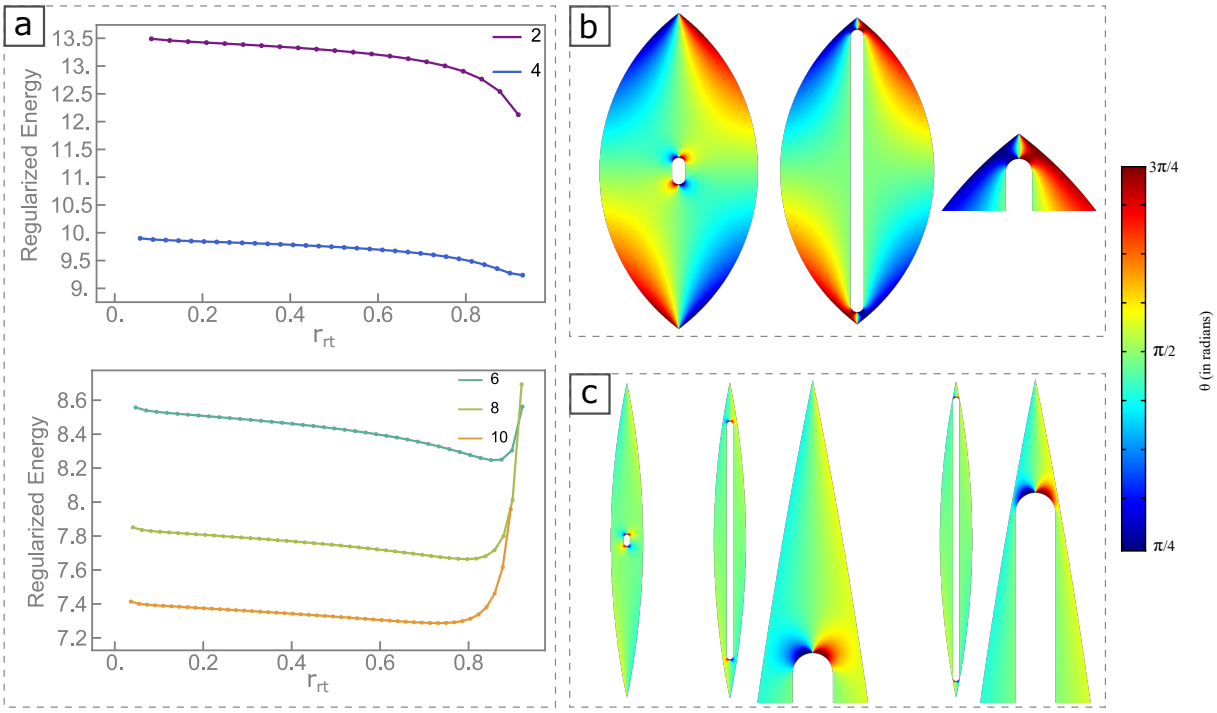


Figure 5.11: (a) Regularized energy of the system by the normalized length (length of the rod divided by the length of the tactoid) and images of the director field for a tactoid of ratio (b) 2 and (c) 10, with rods of different size at the centre.

For the higher aspect ratios (6 above), there is a minimum in energy with the increase of length, with a steep increase in the energy with further rod length increase. High aspect ratios are thin near the tip, so when the rod goes up it gets very close to the limits of the tactoid. The interaction with the limiting walls of the tactoid causes a bigger distortion than the compensation for the proximity of the defects. The decrease in diameter when getting closer to the tactoid tip is more pronounced for a higher aspect ratio, explaining why this minimum happens at a relatively lower distance for a higher aspect ratio (figure 5.11 b,c). For the two defects to get closer, the rod would not be fully inside the tactoid anymore, and this model is not applicable in this situation.

We then investigated if a similar energy trend would be observed when moving the centre of rods close to the tip. The relative position (normalized against the maximum position of the rod while remaining completely inside the tactoid) was used here, so we can compare rods of different lengths (figure 5.12). For a tactoid of aspect ratio 2, the closer the rod got to the tip, the smaller the energy, a similar trend to the one seen for the rod's length. For each position, the longer the rod, the smaller the energy, and the sharper the decrease in energy. This is probably related to the minimization of the energy due to the defects getting closer as explained previously. The difference in energy between the rod at the centre and close to the tip is highest for the longest rods.

The increase to aspect ratio 4 initially leads to a similar trend to the one observed for ratio 2, until getting very close to the end of the tactoid, in which the director change and in one case, even a slight increase in energy is seen. Increasing the aspect ratio further, a clear trend with decrease, a minimum and steep increase is observed. The bigger the tactoid aspect ratio, the minimum gets less deep and at relatively lower positions; the longer the rod the deeper the minimum energy gets before the increase of energy. This increase in energy can be explained by the proximity of the rod to the boundary surface of the tactoid, resulting in a distortion of the director and, consequently, increasing the energy of the system, as seen for the rod's length. With the higher aspect ratios, we see that for the lengths above the minimum seen in figure 5.11, the initial energy is higher (as expected) and the same increase in energy is seen for the other lengths.

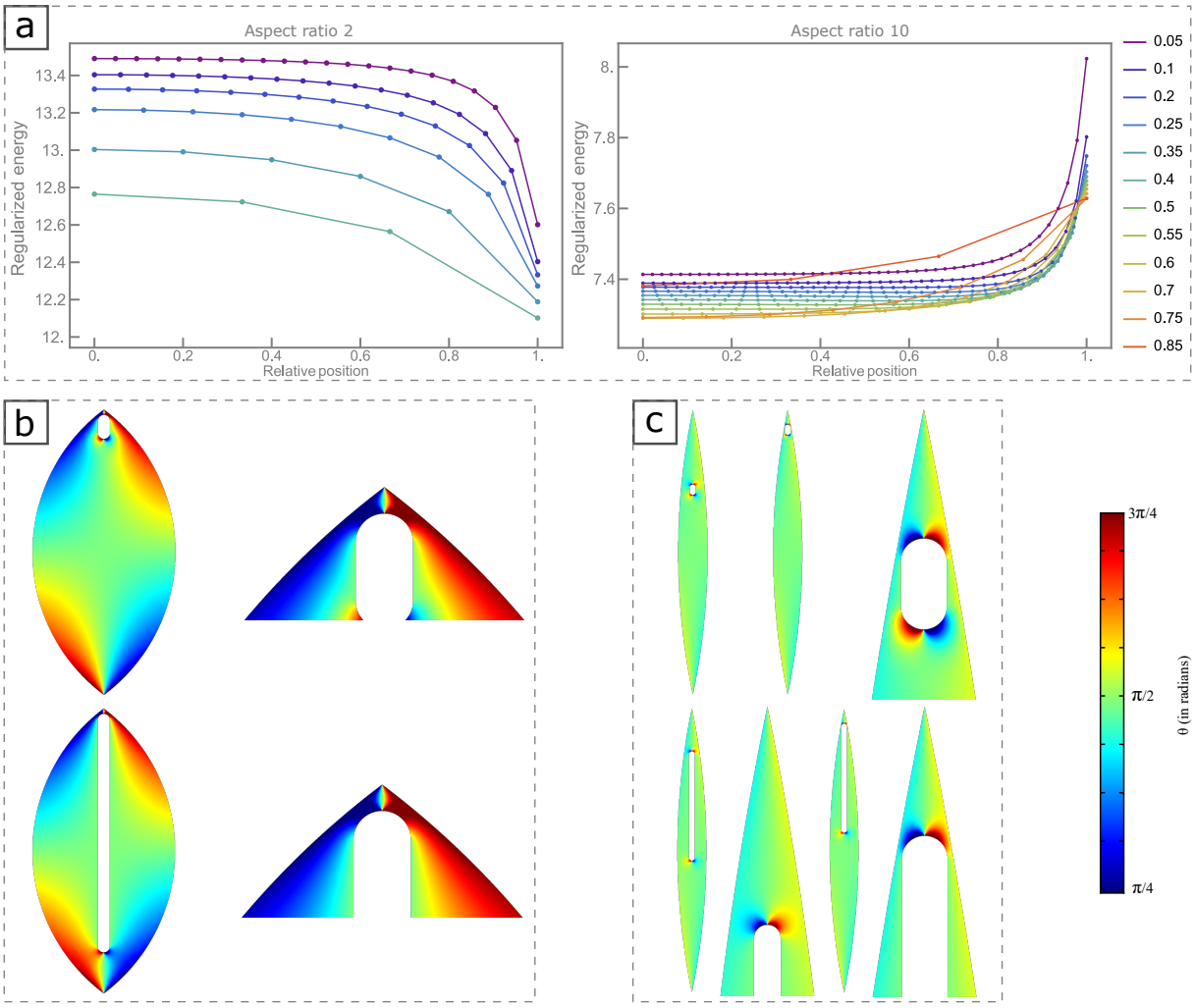


Figure 5.12: (a) Regularized energy of the system by relative position (regarding the maximum position), for different rod's normalized lengths. Images of the director field for tactoids of ratio (b) 2 and (c) 10, with rods of different sizes at different positions, and magnification for the position closest to the tip.

Next, we looked at the effect of changing the rod's diameter for a constant rod length - the thinner the rod, the lower the energy – as shown in figure 5.13. This can be explained by a smaller perturbation since the director deviates less for thinner rods. In the limit of the diameter equal to the mesogen one, the energy of the tactoid without impurity would be obtained. Furthermore, we can see that the energy follows a decay and the higher the aspect ratio the steeper the gradient. Consequently, for larger aspect ratios, the energy difference is bigger (7.4 for ratio 2 vs. 8.3 for ratio 10).

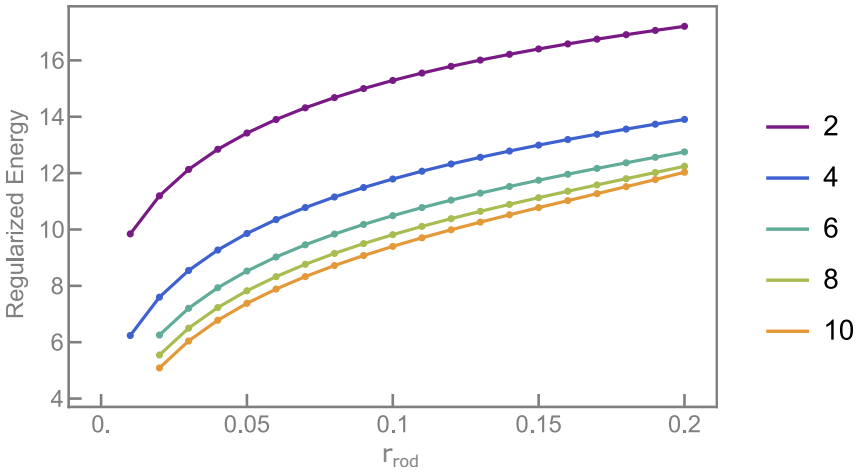


Figure 5.13: Regularized energy for different rod's diameter (r_{rod}), with each line representing the aspect ratio of the tactoid.

Again, we investigated the change in the position (figure 5.14) and the trend followed had similarities to the one observed for length. For ratio 2, the energy decreased with the rod getting closer to the tip for all evaluated diameters. With the increase in aspect ratio, the trend depends on the diameter of the rod. A diameter of 0.05 demonstrates this very clearly; it only decreases for ratios 4 and 6 but presents a minimum for ratios 8 and 10. Thick rods present a minimum, and the thicker the rod, the steeper the increase in energy. This corroborates further our hypothesis that the defects approximation decreases the energy, but being closer to the surface of the tactoid leads to a significant distortion of the director.

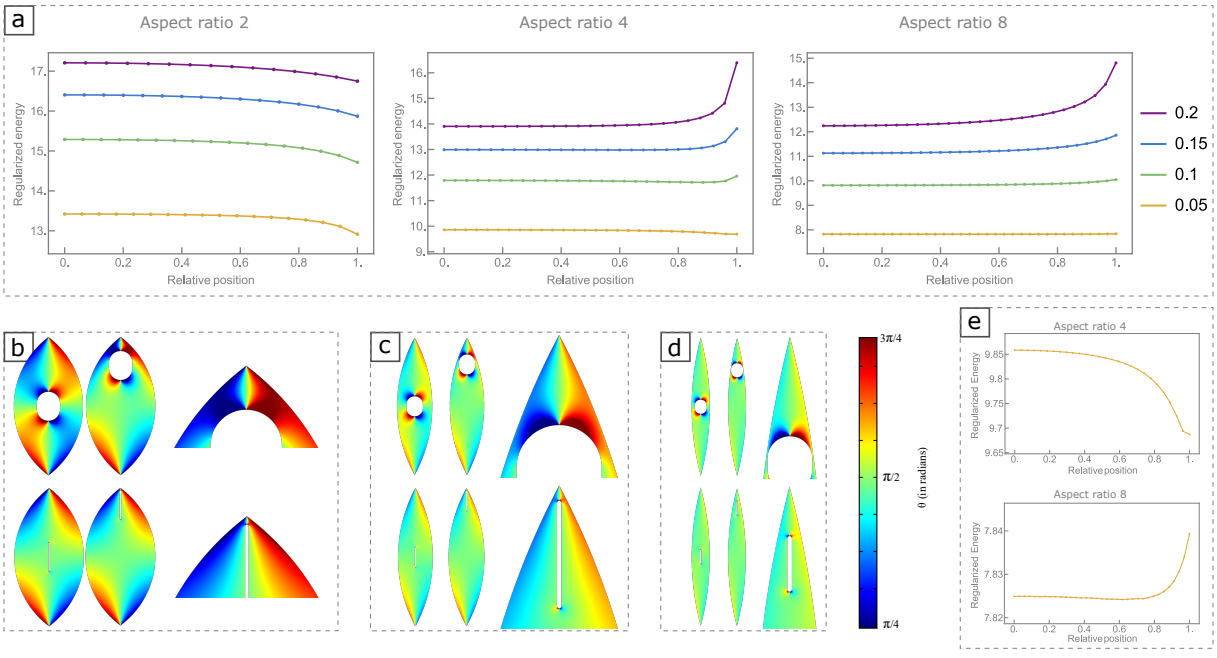


Figure 5.14: (a) Regularized energy of the system by relative position (regarding the maximum position), for different rod's diameter. Images of the director field for tactoids of ratio (b) 2, (c) 4 and (d) 8, with rods of different sizes and at different positions.

Finally, we evaluated the effect of having different elastic constants. As explained in section 5.3.1, we only consider splay (K_1) and bend (K_3) constants, using $\delta = 1 - K_1/K_3$. In this way, the higher and more positive values express greater bend and lower splay cost, with negative values representing the opposite. Using unequal constants is a closer model to reality since we expect that these constants are not equal. These constants are dependent on the characteristics of the mesogen forming the liquid crystal and are not known for the Pf4 virus, so we explored a range of δ values from -0.9 to 0.9.

We similarly performed the calculations as for the one constant approximation and compared the values for the tactoid on its own with the one including a rod. On figure 5.15 we show the results for aspect ratios 2 and 10 since the ones in between follow the same trend as those two – the larger the delta, the smaller the energy. The smaller the aspect ratio the sharper the decrease and at a high delta, the energy for both ratios is almost equal for each case (with or without the rod). This is probably connected to the defect in the tip of the tactoid and rod.

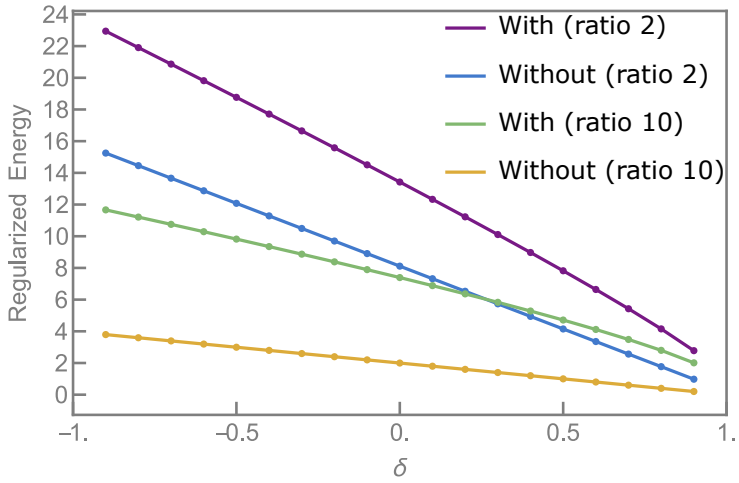


Figure 5.15: (a) Regularized energy by delta for aspect ratios 2 and 10 with and without the addition of the rod.

This can be further seen when looking at the cost of adding the rod for different delta (figure 5.16); the higher the delta, the smaller the cost and the more similar it is for different aspect ratios. The defect at the tip of the tactoid is a splay deformation while the bend deformation is seen at the hemisphere at the extreme of the rods. For high delta, the splay cost is low, minimizing the cost of the defect at the tip and leading to the decrease in energy for all aspect ratios. For the rod addition, the high bend cost leads to a lower extrapolation length of the defect at the tip of the rod. As a result, the distortion of the director and, consequently, the

elastic cost of this defect decreases.

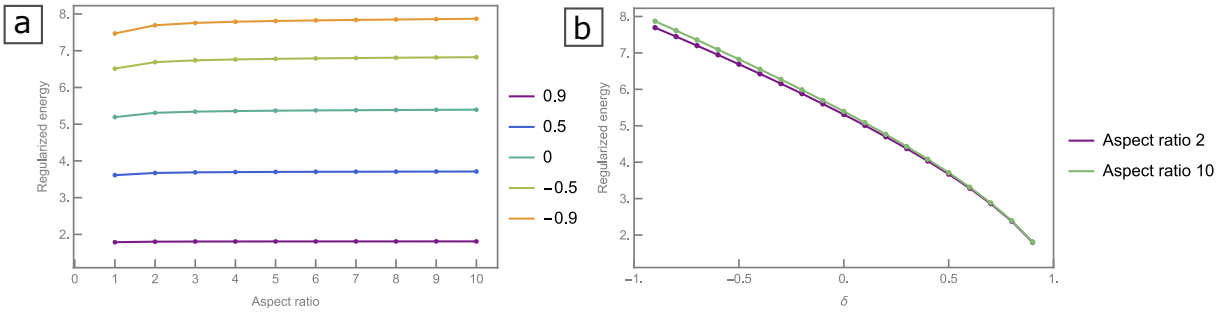


Figure 5.16: Regularized energy difference (a) by aspect ratio for selected deltas and (b) by delta for aspect ratios 2 and 10 with and without the addition of the rod.

5.4.5 Numerical model

The calculations described in this subsection were performed by Dr Yucen Han, Prof Apala Majumdar (Department of Mathematics and Statistics, University of Strathclyde, United Kingdom) and Prof Lei Zhang (Beijing International Center for Mathematical Research, Peking University, China).

To better understand the experimental observations we solved the model presented in section 5.3.2. The first simulation (section 5.4.4) considers a tactoid of fixed shape, initially defined, with and without a rod, so only the elastic constant is calculated. In this second simulation, an initial nematic nucleus is defined, but the system is allowed to go to the final configuration, with the different configurations being obtained using different parameters. Depending on the initial conditions, three different states were found: no attachment, partial attachment and sandwich/encapsulation, as shown in figure 5.17. All three states are observed when the anchoring strength associated with the rod surface (W_l) is zero (eq. (5.20)). As W_l increases, the no attachment configuration loses stability, and only two states are observed. At even stronger anchoring and in the strong anchoring limit, the partial attachment state also loses its stability and the only configuration observed is the sandwich state.

For the finite anchoring strengths explored here, partial attachment is energetically the most stable configuration. This state leads to a reduction in the contact between the isotropic and nematic phases and has only two-point defects at the tips of the tactoid, similar to the no attachment state. As W_l increases, the energies for partial attachment and the sandwich state also increase; having only an isotropic phase along the rod is no longer stable. From some

anchoring strength, the rod cannot be exposed to the isotropic phase and instead becomes encapsulated/sandwiched. The observed states are in qualitative agreement with the experimental observations, i.e. similar states are observed in the 4 experimental systems and the numerical model; however, the kinetic pathways to the different states will be different and may explain differences in observed frequencies.

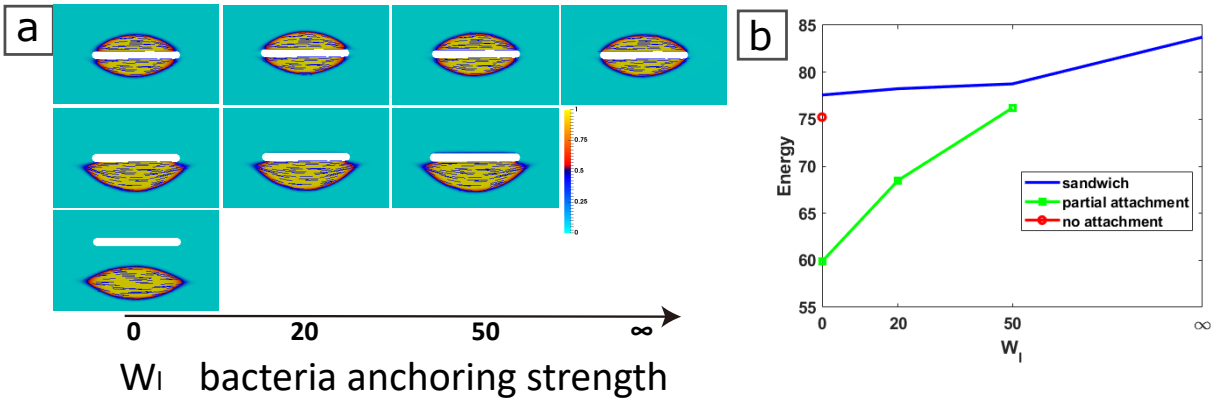


Figure 5.17: Effect of the surface anchoring strength in the interaction between rod and tactoid. (a) Phase diagram of three (metastable) equilibria (no encapsulation, partial attachment, and sandwich) at $\sigma = 1$, $\lambda =$ 1e5, K = 20, W = 20. (b) Energy plot of the states seen in (a).

We next explore the size relationship between the rod and tactoid for three different lengths and widths of the rods (figure 5.18) at a finite anchoring strength of $W_l = 20$. At this anchoring strength the partial attached state, indicated by subscript 1, has lower energy than the sandwich/encapsulation state, indicated by subscript 2. For both states, the energy decreases as a function of the length of the rod l (figure 5.18 c). The reason is that the interfacial "area" between isotropic and nematic phases decreases with rod length. More nematic material can align with the rod. Surprisingly, the energy does not depend strongly on the thickness of the rod.

Furthermore, for the shortest rod and at a given "volume" of tactoid, the sandwich state with the rod sticking out on both sides of the tactoid, is no longer stable, and instead, the rod becomes encapsulated, with one end still sticking out. This leads to a defect around the end of the rod inside the tactoid. Given the natural boundary condition used in the calculations, we see a melted (isotropic) region, resulting in a considerable increase in energy. For the thinnest rod, this melted region is the smallest and therefore has the lowest energy. This defect near the tip of the encapsulated rod has been observed in the experiments with *P. aeruginosa* by Tarafder

et al. [51], so we decided to use a similar experimental set-up used in their experiments, quasi 2D, as explained in the experimental section 5.2 and below (section 5.4.6). Also, our simulation is done assuming a continuum model, however, the tactoids are only a few virus length, so the applicability of a such model may not be the best approach.

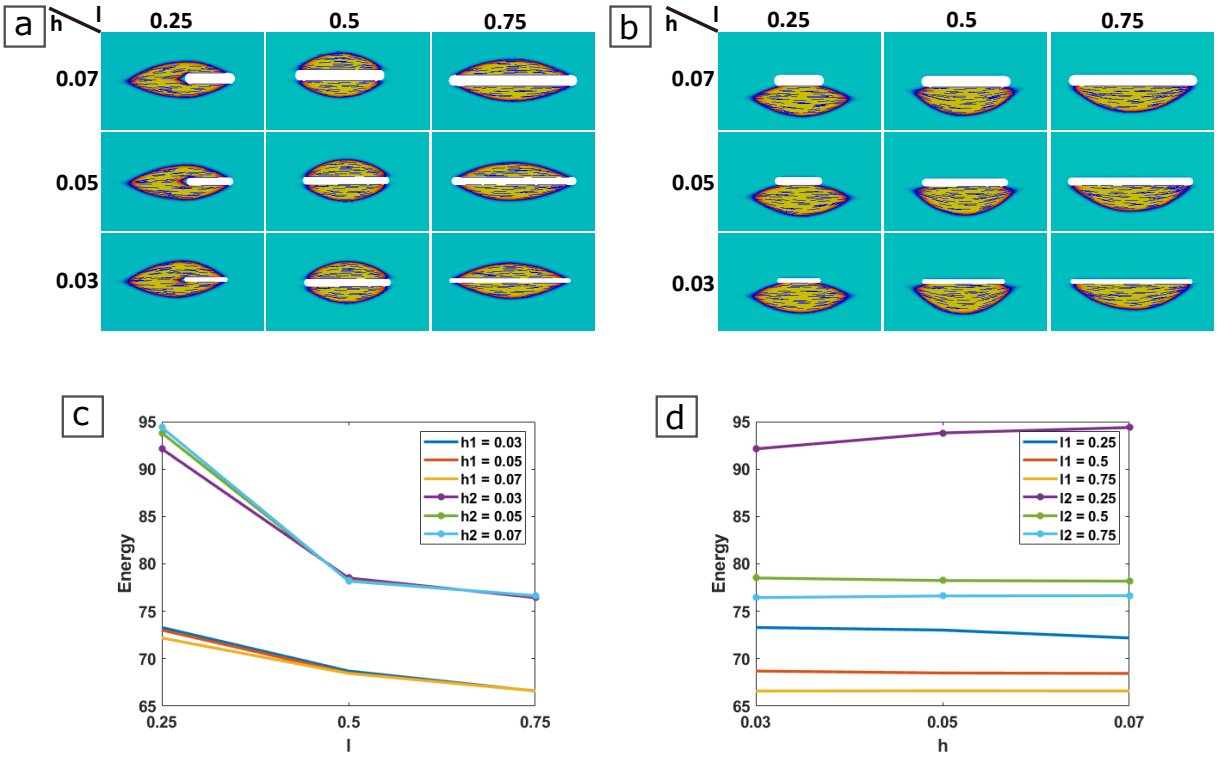


Figure 5.18: Effect of the rod-tactoid dimensions in the type of configuration obtained in the simulation with the same parameters as before and changing rods diameter (h) and length(l) for (a) encapsulation/sandwich (named h2 and l2) and (b) partial attachment (named h1 or l1), and, (c,d) corresponding energy plots for different rod's diameters and lengths having two tactoids.

5.4.6 Quasi 2D experiments result

The experiments described in this subsection were done in collaboration with Dr Iago Grobas.

In comparison with the original work with *P. aeruginosa*, we typically observed that encapsulation was less prominent, which may be connected to the different setups used in that work. There, the system was sandwiched between an agar pad and a cover slide constituting a quasi-2D state. This is in contrast to the capillaries used here, where the bacteria are in 3D bulk. To confirm whether this confinement could affect the configurations obtained, we repeated our experiments with all the rods using a similar setup as in Tarafder *et al.* [51], and the results

for encapsulation are shown in figure 5.19.

Importantly, we found that the shape of the tactoids was different than in 3D, and indeed in this more confined setup, we did see encapsulation for all rods, including *B. subtilis* and silica rods (modified or not). This highlights the importance of this exact geometry. Moreover, the colloidal rods diffuse and sediment in 3D, but are trapped in the 2D setup, and the bacteria swim in 3D, but considerably less when stuck on agar. A full quantitative analysis was not done due to the small number of samples, but it looks as if encapsulation is still the least common case. All of these factors will play a role in the observed configurations and may be related to the anchoring direction the rod surface imposes.

These results are more similar but still different than the ones seen for *P. aeruginosa* [51], in which the tip of the tactoids encapsulating the bacteria was more round. There may be still experimental procedure differences, but, as mentioned in chapter 4, specific batches can lead to differences in phase behaviour. The virus may mutate, which can play a significant role in changes in size, external protein layer, and others.

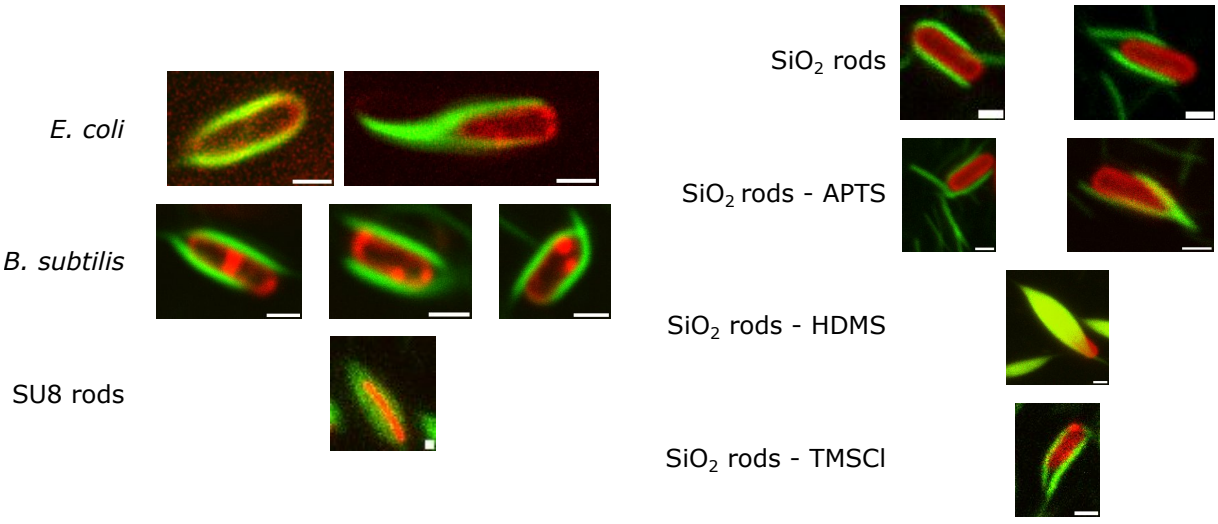


Figure 5.19: Confocal microscope images for all the rods studied in the quasi 2D system. Scale bar is 1 μm.

5.5 Conclusions and Outlook

In this chapter, we were able to study the behaviour of the tactoids in the presence of different impurities. Four configurations were seen: no attachment, partial attachment, sandwich and

encapsulation. The three first states were observed for all the rods tested, while encapsulation was only obtained for *E. coli* and SU8 rods. We determined a geometrical relationship between configuration and the size of the rod and of the tactoid. It was not clear how this relates to the rods' surface properties.

As mentioned in section 5.4.5 the numerical results found similar states as in the experiment. It primarily highlighted the importance of surface anchoring, with stronger anchoring promoting the encapsulation/sandwich state, whilst at low anchoring strength, all states could be observed. In this case, partial attachment has the lowest energy. We furthermore observe that in the numerical results, the rod seems to define the shape and to some extent the size of the tactoid; this is not the case in the experiments.

Encapsulation was experimentally less notable than previously reported [51], possibly related to its high elastic cost. The surface energies are not enough to compensate for this cost and with all energy components considered, encapsulation still has a high energetic value. This energetic cost may help to explain why encapsulation is not seen for all impurities. This state was observed for long aspect ratio rods since this geometry of rods allows the defect to get closer and reduces the disturbance of the director, minimizing the energetic cost. Furthermore, the proximity of the defects also helps to explain why usually encapsulation was found not perfectly centred when considering all the energies.

There are several limitations in both simulations, which may explain some of the differences between the experiments. First, only the elastic condition is considered in the initial calculation using a fixed-shape tactoid. Then, when all the energy components are taken into consideration, the boundary condition used at the curved part of the rod is a natural boundary condition. This may explain the formation of the isotropic phase when one end of the rod sticks into the tactoid (figure 5.18). Secondly, the simulations were in 2 dimensions, whereas the majority of our experiments were done in 3 dimensions. Qualitative changes were seen in the quasi-2D set-up, and encapsulation was found for all the rods studied.

The complexity of the problem is further highlighted by potential differences in anchoring, not only in anchoring strength but also in the preferred orientation. In the numerical model we have assumed homogeneous (planar) anchoring; in previous work on colloidal virus particles [29, 140], namely *fd* virus, we have indeed seen such anchoring, but it is unclear if the behaviour in the vicinity of bacteria walls, or indeed colloidal rods, will follow that trend. Evaluating well-

defined surfaces with characterized anchoring and the effect of confinement can shed further light on this problem.

Acknowledgments

We would like to thank Dr Iago Grobas, from our research group, for all the help with part of the experiments presented in this chapter. We also would like to thank Dr Yucen Han and Prof Apala Majumdar from the Department of Mathematics and Statistics, University of Strathclyde and Prof Lei Zhang from the Beijing International Center for Mathematical Research, Peking University for the calculations performed. Finally, we would like to thank Dr Abul Tarafder and Prof Tanmay Bharat for the Pf4 samples provided.

Chapter 6

Rheological behaviour of Pf4 and sodium alginate mixtures

Abstract

In this chapter, we studied the rheology of the Pf4/sodium alginate system. For that, we prepared samples corresponding to different points that we imaged before (chapter 4), being then able to compare the effect of tactoid size and the structure with the rheological behaviour. We observed an increase in the viscosity of the samples with Pf4 compared to the pure polymer. For concentrations corresponding to tactoids, the fluid was still more liquid-like while for the network structures, we saw a transition from solid- to liquid-like behaviour as a function of stress and frequency. We interpreted these observations in light of biofilm stability and clearance.

6.1 Introduction

We will start with the experimental methods followed by the results and discussion. The latter will be divided into the experiments done with samples in the tactoid range and then in the network structure range. This will be associated with the results presented in chapter 4 and, finally, we will present our conclusions.

6.1.1 Rheology basics

Rheology can be defined as the study of material deformation and flow. Here, we will present the basic concepts using the books from Schramm [141] and Barnes [142]. First, we look at what may happen to a material under stress. A perfect solid will respond with an elastic deformation, with the energy used to deform the material being stored (e.g. by stretching the structure) and fully recovered once the force is released. Differently, an ideal fluid flows under stress - the energy applied is used to suppress the internal friction, thus, being completely lost, and irreversibly dissipated. This resistance is called viscosity (η) and it is defined as shear stress (τ) divided by shear rate ($\dot{\gamma}$): $\eta = \tau/\dot{\gamma}$.

Most real-life materials are neither an ideal solid nor an ideal fluid and a number of them can flow and are elastic, being called visco-elastic. Viscoelasticity is a characteristic being caused by the presence of long entangled polymer chains, cross-links, and aggregates. Their elastic and viscous components are usually characterized using a rheometer. This equipment measures the response of the material under the influence of stress or strain, and in our case, we used a stress-controlled instrument. A torque is applied, associated with the stress by a constant specific to the geometry used, and the resulting strain is measured. Different geometries can be used, such as parallel plates, cone plates or concentric cylinders (one fixed, one rotating in all cases) as shown in figure 6.1.

The shear stress applied by these instruments can be understood by thinking about two parallel plates with the bottom one fixed and the top one moving. At low rates, the material deforms laminarly with such movement as schematically shown in figure 6.2. Shear stress is defined as $\tau = F/A$ where F is the shear force and A the area of the plate (units $N/m^2 = Pa$), and the shear rate is defined as $\dot{\gamma} = v/h$, where v is the velocity and h is the shear gap (units

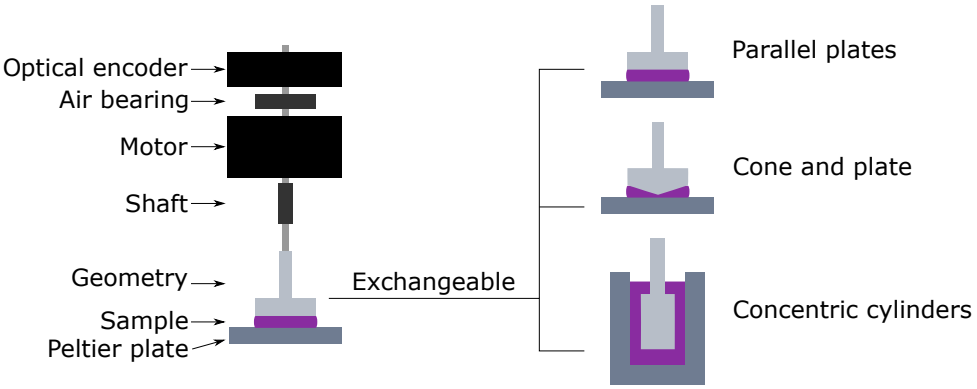


Figure 6.1: Sketch of a stress-controlled rheometer and main geometries used.

$ms^{-1}/m = s^{-1}$). The stress is obtained by the torque applied, through a constant dependent on the geometry, and the shear rate by the velocity since the shear gap is known.



Figure 6.2: Sketch of shear stress applied with a force F at a velocity v to parallel plates of area A with a distance h between them, resulting in a laminar flow.

Many experiments can be performed in a rheometer, and the most common ones are creep and recovery, flow and oscillatory tests. The first one is a test in which a certain amount of stress is constantly applied (creep) and then released (recovery), and is usually used for materials with a significant elasticity. Flow sweep and oscillatory tests are the ones used in this work and the theory behind them will be explored further.

Flow sweep

Flow sweeps are experiments usually performed on fluid-like samples to obtain the viscosity dependence on the shear rate. Different behaviours are observed and a summary of them is shown in figure 6.3. When the viscosity does not depend on the shear rate, the fluid is called Newtonian, and water is the most well-known example. When the viscosity does depend on the shear rate, the fluids are then called non-Newtonian.

Shear thinning fluids, also known as pseudoplastic, are characterized by a decrease in viscosity with the shear rate, a reversible phenomenon for most materials. This is commonly

seen when the structures forming the fluid align with the shear, being able to flow more easily. This behaviour can also be the result of aggregate destruction, stretching of chains, or stretching or deformation of particles. The opposite behaviour, in which the viscosity of the fluid increases with the shear rate is called shear thickening, or dilatant fluid.

Last, a plastic liquid (or Bingham plastic), is a fluid that does not flow until a minimum yield point is achieved, after which shear thinning behaviour is observed. They can keep their shape due to the intermolecular network. A force smaller than the one sustaining the network will result in elastic deformation. Higher shear stress, above the yield point, will result in a break-up of the network and leads to the flow of the material.

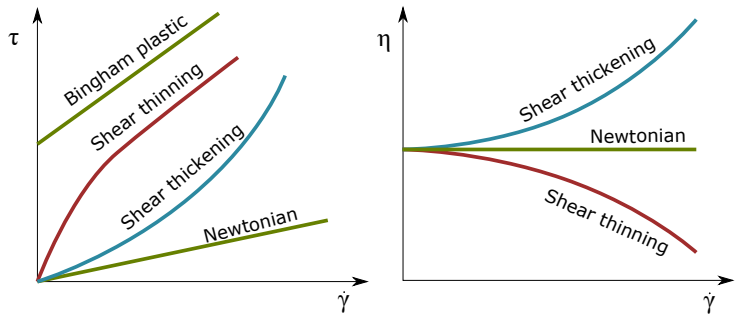


Figure 6.3: Example of different fluid behaviours under different shear rates.

Oscillatory tests

In oscillatory tests, stress is applied as a sinusoidal time function and the time-dependent strain is measured. If the displacement is not too large, then a sinusoidal response curve is obtained. This makes it possible to evaluate how the elasticity and viscosity of a sample vary with the stress (amplitude sweep) or frequency (frequency sweep). A perfect solid strain response will follow a perfect phase with the applied stress, while a perfect fluid will have a 90° phase shift (figure 6.4). Viscoelastic fluids have a phase angle between 0 and 90°, being below 45° for gel-like and above it for the fluid state.

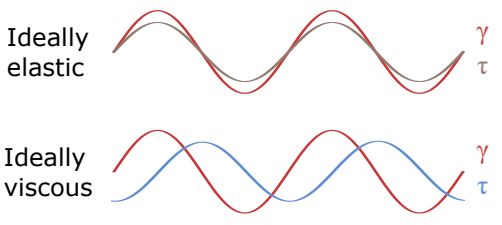


Figure 6.4: Oscilatorry sine curve stress and the corresponding strain for a perfect fluid and perfect solid.

The total resistance of a substance against the applied strain is defined as the complex modulus $G^* = \tau_0/\gamma_0$, where τ_0 represents the shear-stress amplitude and γ_0 refers to the strain amplitude. The complex modulus can be divided into an elastic or storage modulus (G') and a viscous or loss modulus (G"):

$$G^* = G' + iG'', \tag{6.1}$$

where $G' = G\cos(\delta), G'' = G\sin(\delta)$, and δ is the phase angle shift. The term storage modulus refers to the temporary loss of energy that can be recovered afterwards, being the only term contributing to a perfect solid. On the other hand, the loss modulus refers to the irreversible loss of energy and it is associated with fluid behaviour. In this case, a complex viscosity can be defined, which describes the total resistance of the sample against the dynamic shear.

A stress sweep, also called amplitude sweep describes the non-destructive deformation range of the sample by changing the amplitude of the sinusoidal curve while keeping the frequency constant (figure 6.5 a). The main use of this mode is to determine the linear viscoelastic range (LVR) of a sample. It is also possible to do a frequency sweep in which the time-dependent behaviour is evaluated by applying a sinusoidal curve with constant amplitude and variable frequency (figure 6.5 b). High frequencies describe fast motion (or short timescales), while low frequency describes slow motion or even rest. The stress chosen should be within the LVR and both tests assume the sample is time stable. By keeping both amplitude and frequency constant it is possible to perform a time or temperature sweep.

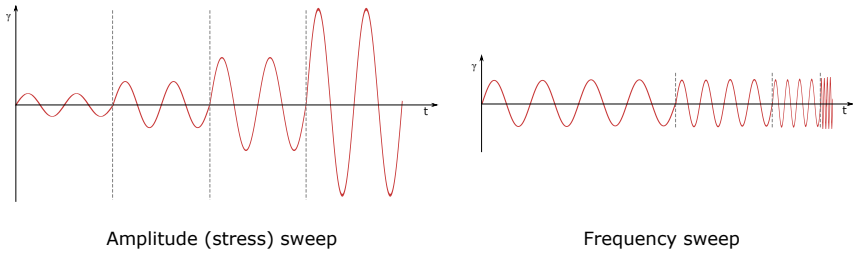


Figure 6.5: Oscillatory sine curve stress and the corresponding strain for a perfect fluid and perfect solid.

The linear viscoelastic range refers to the limit where G* (or each of its components) is constant with the change of stress. This region is where the deformation of the sample is small or applied slowly to the point the molecular arrangement is never far from equilibrium, and the stress and strain are linearly related. Above this value, the sample is deformed beyond the internal temporary bonds (for molecules), aggregates are destroyed, and a major part of the

energy is lost as heat. Figure 6.6 shows a typical amplitude sweep curve within the LVR region and outside of it.

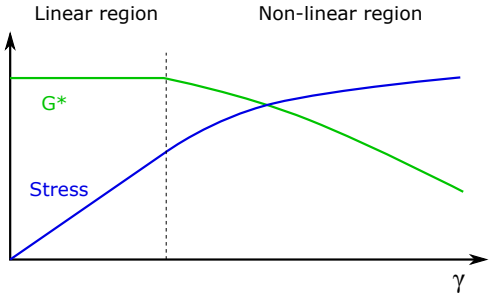


Figure 6.6: Example of a stress sweep curve showing a linear and a non-linear viscoelastic region.

Studying samples within this range is important because the theory behind the behaviour of visco-elasticity involves linear differential equations. Leaving the LVR leads to deviations that cannot be accounted by the usual theory. The non-linear behaviour is more complex to understand and can be attributed to inhomogeneities, rearrangement of particles, surface effects, and others. To understand non-linear behaviour, rheology is usually used with other techniques such as microscopy.

6.1.2 Motivation and outline

This chapter is a work in progress that, besides showing how the presence of tactoids changes the properties of the system (and probably of the biofilm), also helps to understand what has been presented in chapter 4. Looking at the viscosity, it is possible to understand further the differences in kinetics growth and size of the tactoids (sections 4.3.1 and 4.3.2). It helps to see that the low concentration of polymer and low viscosity of the system makes it easier for the mesogens and the tactoids to move and form bigger droplets. It also shows a significant increase in viscosity with the increase in polymer concentration, especially in the presence of the rods. This can further help us to understand why the tactoids grow so little in this case and may have a harder time coalescing.

When looking at the network, it is possible to see the increase in elasticity of the system, formation of an interconnected structure, complementing our visual observations. In this chapter, we will present the rheological study of pure sodium alginate samples and in the presence of Pf4. Knowing that the rheological properties matter for the protection from pathogens, it

is important to evaluate how this behaviour is connected with the presence of a nematic phase (tactoid).

6.2 Experimental method

The samples used in these experiments were done using non-labelled Pf4, prepared as described in section 2.2.1, and mixed with sodium alginate as described in section 2.2.4. All samples were prepared in a centrifuge tube and equilibrated for 24 hours before the rheology experiments were performed. We left the samples equilibrating for only 24h because this was the interval used to obtain the images for the phase diagram and for the size determination. All the concentrations and names for the samples done are presented in table 6.1, where S is used for sodium alginate, P for Pf4 and the number represents the concentration in mg/mL with the last number corresponding to the first decimal point. Except for S08P119, all samples were tested twice to confirm the trends observed.

Table 6.1: Name and concentration of the samples studied in this chapter.

Name	Sodium alginate (mg/mL)	Pf4 (mg/mL)
S25	2.5	0.0
S25P10	2.5	1.0
S25P20	2.5	2.0
S150	15.0	0.0
S150P10	15.0	1.0
S24	2.4	0.0
S24P109	2.4	10.9
S08	0.8	0.8
S08P119	0.8	11.0

The experiments were done with a stress-controlled AR-G2 rheometer from TA. Two geometries were used: a stainless steel 20 mm parallel plate and an aluminium 60 mm 0.99° cone plate. The first was used for the tactoid samples since the available volume of the sample is small. We chose a 200 μm gap to use the smallest amount possible of the sample (approximately 80 μL used per experiment) while still ensuring a value more than 10 times bigger than the tactoids size we measured. This geometry could also be used for sodium alginate 15 mg/mL. The second one was used for all the other sodium alginate samples since they have a low viscosity and had more sample available (approximately 1 mL used per experiment).

The rheometer's bearing was checked daily and the geometry and instrument were also

calibrated and mapped (rotational and oscillatory) daily with the geometry and the solvent trap filled as it was going to be used. Flow and oscillatory experiments were performed, all at 20 °C and with the motor in soft mode. For the flow sweep, the angular velocity was evaluated between 10 and 0.01 $rad.s^{-1}$, with equilibration and an average time of 120 seconds. For the stress sweep, a frequency of 0.04 Hz was used, changing the torque from 0.01 to 50 $\mu N.m$, while for the frequency sweep a torque of 0.1 $\mu N.m$ was chosen, and the frequency was evaluated between 0.01 to 10 Hz. Only for S24P109, the frequency sweep was repeated with a new sample at 0.02 μNm. For both oscillatory tests, 20 acquisition cycles were used to obtain an acceptable average.

6.3 Results and discussion

Even though it is known that the presence of divalent cations in biofilms [143] affect the rheological properties of sodium alginate, we decided to study a system similar to the ones used for the microscope images, containing only monovalent cations present in the PBS. This is also the reason why we left the samples equilibrating for only 24 h, knowing they would not be fully equilibrated after this amount of time. Our experiments were done close to the limit of the instrument's ability. Furthermore, considering the low viscosity of the samples, the ideal was to perform the experiments using a geometry with a large diameter (at least 40 mm rather than the 20 mm one used). Because of that, we checked if the instrument was giving good results using a 20 mm plate with decane, a sample of known low viscosity and low surface tension, and a standard oil of higher viscosity (S60), as exemplified in figure 6.7.

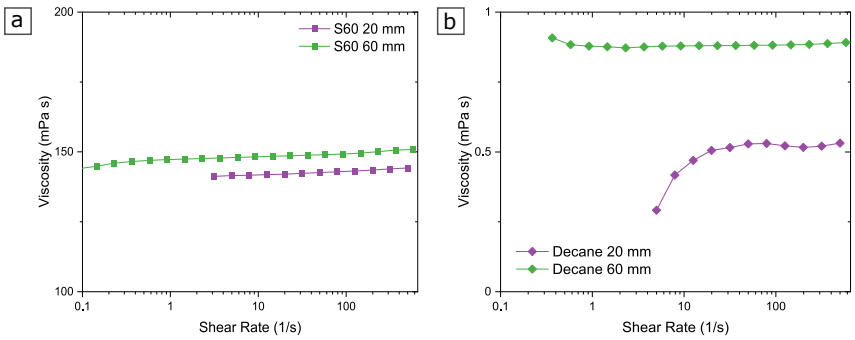


Figure 6.7: Flow curve of (a) standard S60 and (b) decane performed using the 20 and the 60 mm geometries.

The values were slightly lower for the smaller geometry, but we confirmed that the in-

strument gave acceptable results for our conditions. It is still imperative to be careful when analysing the data presented here, especially for oscillatory tests. In this latter case, inertia can play a significant role and all the points with phase shift >150° are highlighted in our results since they are inertia dominated. Therefore, all the results will only be qualitatively compared.

6.3.1 Tactoid samples

Sodium alginate 2.5 mg/mL seems visibly to have low viscosity, so we decided to obtain the flow curves on its own (S25) and with the addition of 1 and 2 mg/mL Pf4 (S25P10 and S25P20, respectively). First, we looked at the flow curves obtained using a 20 mm parallel plate or a 60 mm cone and plate for the sodium alginate to evaluate if it was acceptable to compare samples done with different geometries (figure 6.8 a). The viscosity increases when decreasing the geometry diameter, as seen for the standards initially tested. Since we expected a higher viscosity for the samples with Pf4, and lower surface tension, we proceeded using the 60 mm for S25.

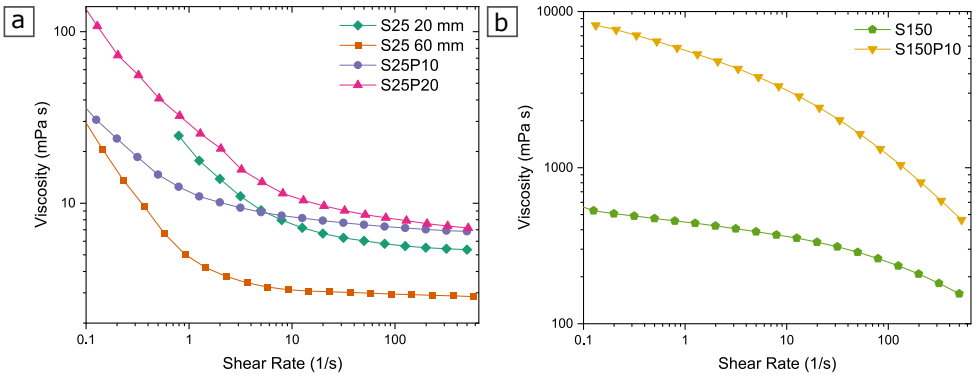


Figure 6.8: Flow curve of samples (a) S25 (comparison of experiments performed using the 20 and the 60 mm geometries), S25P10, and S25P20 and (b) S150, and S150P10 samples.

As can be seen in figure 6.8 b, all the samples are shear thinning as expected - the polymer networks and the tactoids align with the shear and the viscosity decreases. The addition of Pf4 and the formation of tactoid results in an increase in the viscosity of the system. Considering there are no bivalent cations in our sample, it is likely that this increase in viscosity was caused by the presence of the nematic phase instead of cross-linking and entanglement of the polymer. This result also agrees with our microscopy observations and with the results obtained by Secor *et al.* [50]. It is important to note that at low torque (and shear rate), the effect of surface tension effects can be seen in samples of low viscosity through the steep increase in viscosity at

low shear rates, and it is likely this is being observed for these samples.

Surprisingly, when we compare the two samples with Pf4 concentration, we see a small viscosity difference, with a higher value for S25P20. This may be connected to the particle size and volume fraction. As shown in chapter 4 (figures 4.9 and 4.10), for 24 h, the increase in Pf4 concentration from 1 to 2 mg/mL resulted in a slight decrease in tactoid volume, increase in number density, and increase in the aspect ratio average and polydispersity.

For a system of equal volume fraction, the viscosity increases when the size of the particle decreases since the number of particles (and interactions) also increases. Similarly, for particles of similar size, the increase in particle number, and, consequently, in volume fraction, will change the number of interactions, and the flow behaviour will go from Newtonian to shear thinning up to shear thickening. Looking specifically at rods, it has been shown in the literature that the excluded volume strongly increases with the concentration of the rods. When the number density is much bigger than the overlap density, the rotational dynamics are reduced and a strong shear-thinning behaviour is obtained [22, 144, 145]. Also, for polydisperse samples, as the fraction of long rods increases, the shear-thinning behaviour is more pronounced, meaning that longer rods dominate the shear-thinning behaviour. At very low shear rate, both species (short and long) hinder each other, so the system is quenched and the average length dictates the behaviour. At intermediate shear rate, the longer particles govern the shear thinning behaviour and the system is highly sensitive to the applied flow. Finally, at very high shear rate, hydrodynamic effects have to be considered [146].

S25P20 has more particles (higher tactoid number density), and a higher concentration of rods, so at a low shear rate, the rotational dynamics is hindered, and, consequently, the sample has a higher viscosity, as well as a steeper shear thinning behaviour. Last, since at high shear rates the rods are aligned and variations tend to an extremum [144, 146], we see similar values for both samples. It is also important to note that we are not sure of the rod length distribution in each phase, which can also have an impact on our observations.

Sodium alginate 2.5 mg/mL was the lowest concentration of polymer we studied in chapter 4, hence we also evaluated the opposite end, the highest concentration of polymer (15 mg/mL). It is possible to see, again, that we have a shear-thinning fluid and a significantly higher viscosity for both samples (S150 and S150P10). The entanglement of the chains increases with the polymer concentration, and, consequently, so does the viscosity. This seems to be the

most important parameter when comparing the viscosity of the samples with different sodium alginate concentrations. The difference between the S150 and S150P10 is bigger than for S25 and S25P10. The first form tactoids with smaller volume and aspect ratio, but higher number density than the latter. This increase in the number of particles can explain the difference in viscosity observed.

Due to the higher viscosity of this sample, we also examined the oscillatory behaviour, presented in figure 6.9 a. We began with the amplitude sweep to evaluate the LVR. Even at this higher concentration of sodium alginate and with the addition of Pf4, the sample is more liquid-like than solid-like (G"$>$G'). We can observe a long LVR for both samples, with the range for the storage modulus being shorter. Both moduli are higher for S15P10 than for the pure polymer, compatible with the observation of the increase of viscosity. Again, this behaviour is probably related to the presence of tactoids in the sample.

We then performed a frequency sweep of the sample (figure 6.9 b). With the increase in frequency, we see a decrease in complex viscosity and an increase in G' and G". For all the frequencies used here, the sample is more liquid-like. This type of curve is characteristic of weakly structured samples, indicating that the tactoids are dispersed throughout the isotropic phase and do not form an interconnected structure (compatible with the microscope images).

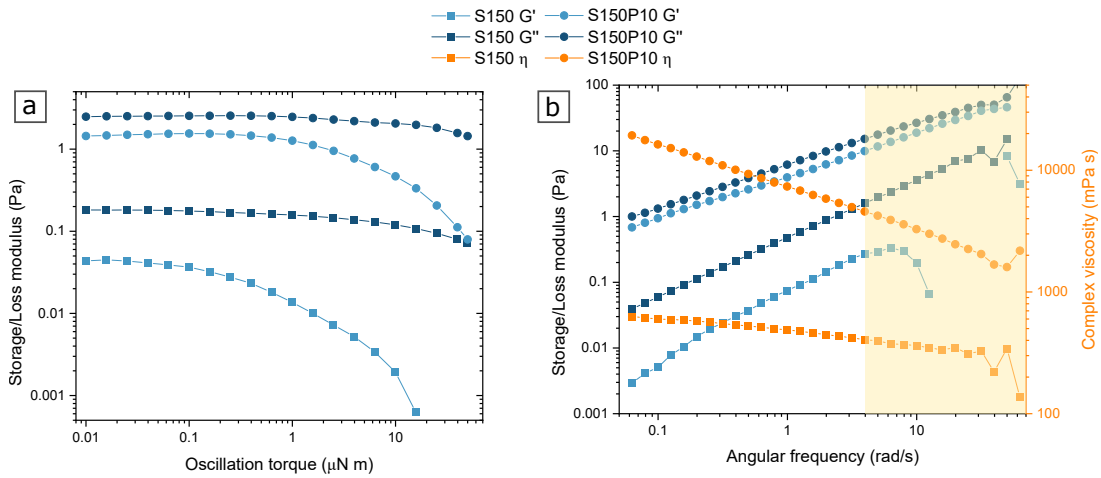


Figure 6.9: Oscillatory (a) stress and (b) frequency sweep of S150 and S150P10 samples.

6.3.2 Network samples

The S24P109 sample is the same concentration as point 2 line 2 of the phase diagram, in which a network-like structure has been seen (figure 4.12). Even though the polymer has low viscosity,

we first obtained the oscillatory curves (amplitude and frequency sweep) for the polymer only, so we could compare them with the behaviour of the network. First, we performed a stress sweep (figure 6.10 a) and we can see that the polymer is fluid-like as expected. The sample with tactoid (S24P109) shows an initial high elastic value and a cross-over to fluid-like behaviour. Also, both G' and G" are higher for S24P109, indicating the stronger resistance of the system.

The sample does not have a clear LVR, but we investigated the frequency sweep for small torque (figure 6.10 b). We can see that for the polymer sample, there is a decrease in the complex viscosity and an increase in G' and G" with the frequency. A similar trend is followed by the viscosity for sample S24P109, but the complex moduli are very close. This could be due to the torque used being too close to the cross-over point and the rheometer could not distinguish well each component of G*. We repeated the experiments using a lower torque (figure 6.10 c) and we can see the crossing of G' and G", with the sample getting more fluid-like with frequency. We also note that G' is almost independent of the frequency, which indicates a structured sample [147], as expected for the network formed.

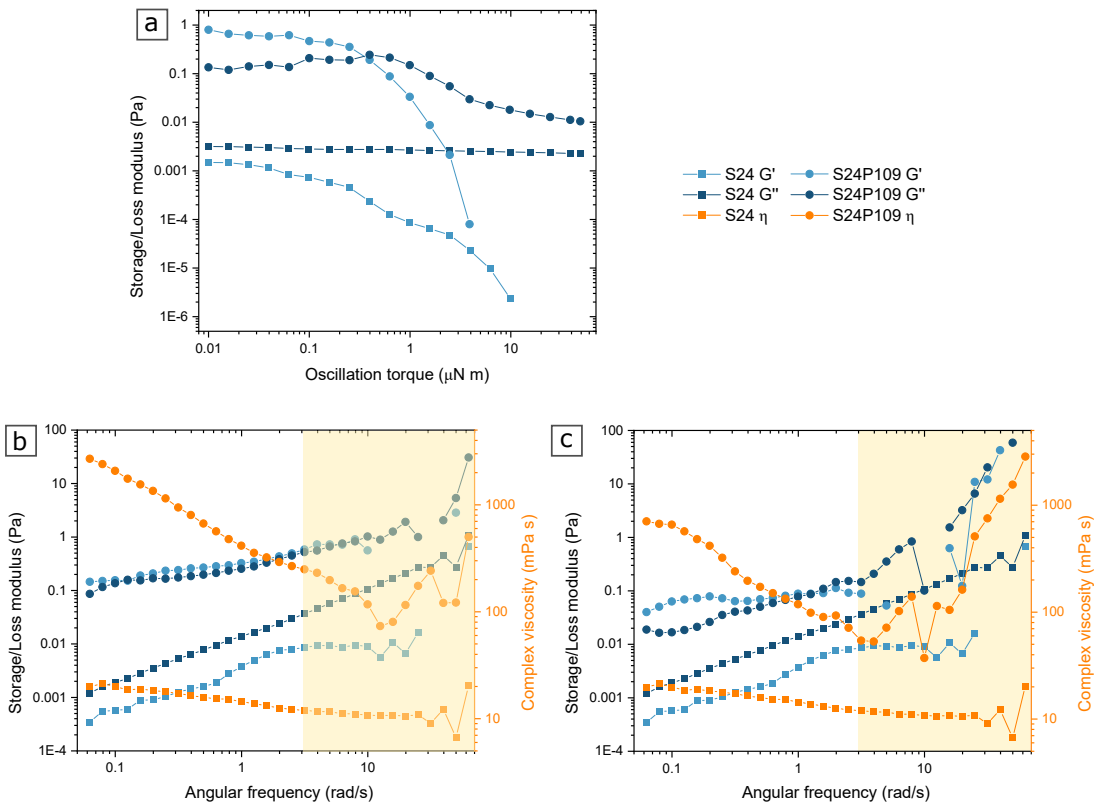


Figure 6.10: Oscillatory (a) stress and (b) frequency sweep at torque 0.1 and (c) 0.02 μNm of S24 and S24P109. The orange shade indicates the points where the phase angle>150°. The values of G' at high stress are not shown in the graph because they are complex values due to the inertia overcompensation.

We then proceeded to do experiments with a sample corresponding to point 3 of line 3 from the phase diagram (sodium alginate 0.8 mg/mL and Pf4 11.9 mg/mL). S08P119 has a lower concentration of polymer and a higher concentration of phage than the previous one, and, from the microscope images (figure 4.12), seems to have a less interconnected network. For the amplitude sweep, we see, as previously, that the polymer is completely fluid-like while the tactoid sample starts more solid-like. The crossover for S08P119 is at lower torque than the one for S24P109 and the values of G' and G" are smaller. This indicates this sample is less structured, a result in agreement with the microscopy images.

This sample also does not have a clearly delimitated LVR, but, again, we performed a frequency sweep. The curve is more similar to the one seen for tactoids (S150P10) – G' and G" increase and the complex viscosity decreases with the frequency. This is further indicative of the weak structure of the sample. However, for S08P119, G', G" and the complex viscosity are smaller than for S150P10, but bigger than for S25P10, indicating there is some level of structure, especially considering this sample has only 0.8 mg/mL sodium alginate.

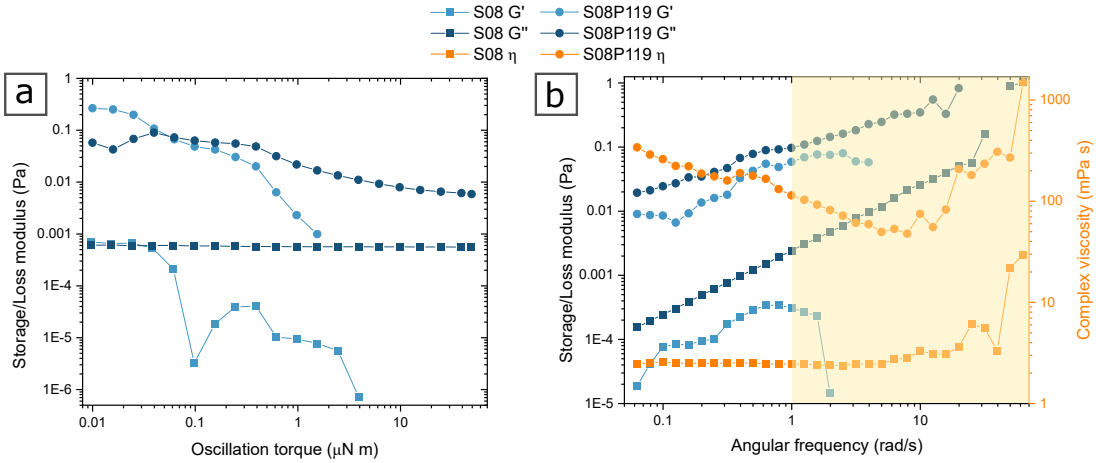


Figure 6.11: Oscillatory (a) stress and (b) frequency sweep of S08 and S08P119. The orange shade indicates the points where the phase angle>150°. The values of G' at high stress are not shown in the graph because they are complex values due to the inertia overcompensation.

6.4 Conclusions and outlook

We have characterized the rheological behaviour of pure sodium alginate samples or in the presence of Pf4, with both components evaluated in different concentrations. Even with a properly calibrated and mapped rheometer, our results are noisy since we used the instrument very close to its limit. This is because for low-viscosity samples, bigger geometries are necessary

than the 20 mm we used. With the amount of sample we had available, it is not possible to use the ideal geometry, so we chose to do a qualitative analysis.

We note that sodium alginate is more fluid-like and possesses shear-thinning behaviour, as previously described in the literature [67]. The addition of Pf4 changed this behaviour in different ways, depending on the concentration. For concentrations where there was formation of tactoids (as indicated by the results in chapter 4), the sample was still more liquid-like and shear-thinning, but there was an increase in viscosity due to the nematic phase. When the concentration of phage was in the values that we previously observed network structures, a transition from more solid-like to fluid-like behaviour was observed. One of these samples is more structured than the other, in agreement with the microscope images.

Evaluating more points, at different times, and using more samples to check reproducibility is an important step to understanding the rheological changes due to the formation of a nematic phase. Considering the amount of sample possible to be isolated, exploring microrheology offers a good alternative, which would also offer a good insight into the heterogeneity of the samples. Having these pieces of information is quite important in developing methods to tackle *P. aeruginosa*, considering the mechanisms for clearance of mucus and biofilm of infected patients.

Chapter 7

Conclusion

In this final chapter, we will go through the thesis chapter by chapter, report the main findings and then make recommendations for further work. We began this thesis by exploring the well-known synthesis of silica rods. It involves several variables, which makes the production of particles with an exact desired morphology challenging. We made bent-core rods, using perturbations during the particle growth, and the temperature was the most promising one. The bending of particles is highly dependent on the ammonium hydroxide concentration and on the extension of hydrolysis of the precursor (TEOS) used. These two variables are related to the change in the rates of hydrolysis and condensation, which has been previously shown to change the rods morphology [87]. The amount of base can be easily tracked using pH, however, the level of precursor hydrolysis is harder to determine and even harder to control. This results in a challenging synthesis to reproduce, making it difficult to obtain the desired morphology.

Subsequently, we focused the rest of the thesis on the phase behaviour of tactoids formed by the suspension of Pf4 phage in sodium alginate using microscopy and rheology. We observed a relationship between tactoid growth and size with the concentration of the polymer – high concentrations of sodium alginate result in smaller and quickly formed droplets. This is most likely related to the strong depletion interaction, leading to the rapid formation of numerous small tactoids, and with the high viscosity of the system, being difficult for them to diffuse and merge. Especially for a lower concentration of polymer, we noticed an increase in the volume of tactoids following a decrease in the number of tactoids, indicating they were merging to form bigger droplets. The tactoid aspect ratio decreased with the droplet volume. This is probably

related to the presence of polymer, which has a strong effect on the dimensions of the tactoids. We also found a relationship between the concentration of tactoids in the sample and the number density of Pf4.

We then explored the phase diagram experimentally, in which we obtained an isotropic and a biphasic region, where tactoids and a network-like structure were seen. Networks formed at higher concentrations of virus and smaller concentrations of polymer and seemed to consist of a line of small tactoids connecting head to tail. The formation of these structures is probably related to the viscosity of the system, weak depletion attraction, and high polydispersity of the Pf4 virus. We suppose that long mesogens are probably spanning more than one tactoid, connecting them. This is a similar reason for the flower-like arrays we saw for bigger tactoids.

The boundaries of the theoretical phase diagram were in good agreement with the experimental points. The theory is simplified, not considering charge and polydispersity, so the agreement is a positive surprise, with the weighted average for the virus length and mass giving the best agreement. This opens the door to understanding how changing the properties of the rods (e.g. using antibodies) can help to disrupt the nematic phase. The theory cannot distinguish between the tactoids and network, and it indicated we did not obtain a purely nematic phase because the necessary concentration of Pf4 for such phase is higher than we were able to obtain experimentally.

The phase behaviour of these tactoids can be correlated with observations done for other mesogens previously described in the literature. Investigating the effects of polydispersity, aspect ratio, and stiffens, can help to understand the impact on which structure is formed, size, growth kinetics, and the rheological behaviour. Studying the growth and rheological behaviour of more concentrations and with different equilibration times would shed further light on this problem.

To study the effect of impurities in the Pf4 tactoids, we synthesized spherocylindrical silica rods in different sizes to be used as a model for *P. aeruginosa* bacteria. The size and zeta potential of the rods were similar to the ones reported in the literature for this pathogen. We also modified the surface of these particles making them either positive or hydrophobic. Furthermore, to evaluate the effect of different impurities, we used another synthetic rod (SU8) and bacteria (*E. coli* and *B. subtilis*). We found four configurations that we classified as no attachment, partial attachment, sandwich and encapsulation. We associated the state formed with the size ratio between the length of the tactoid and of the impurity and with the aspect

ratio of the rod itself. The effect of the surface property was not clarified since modifying the surface of the silica particles to positive or hydrophobic was not enough to observe encapsulation, which was obtained for the hydrophobic SU8 rods.

The free boundary numerical results found all the states we obtained experimentally, having a differentiation of sandwich/encapsulation depending on the size of the rod. These results also showed that surface anchoring is important and the stronger it gets the fewer configurations are stable – no attachment quickly loses stability, and partial attachment later. Only sandwich/encapsulation is observed at stronger anchoring. Besides the anchoring strength, there is also the anchoring orientation. The calculations assumed homogeneous (planar) anchoring, which has been reported to be the case for *P. aeruginosa*, but no evidence shows this is the case for the rods we studied. Furthermore, for these theoretical results, the size of the tactoid was connected with the size of the rod, which is not the case experimentally, with sodium alginate still being the most important parameter in determining the dimensions of the droplets.

Encapsulation was less common than previously reported, probably connected with the high energetic value of this state. This may explain why this configuration was not observed for all impurities. Higher aspect ratio rods got encapsulated, probably because the defects on the tip of the rod and of the tactoid got closer. The proximity of defects was shown to minimize the elastic cost, which can be obtained by using a longer rod or by moving it close to the tip of the tactoid. This can also justify why it is common to find the rods dislocated from the centre of the tactoid.

The simulations were done in 2 dimensions, while most experiments were done in 3 dimensions, probably explaining the differences observed between experiment and theory. Qualitative changes in the tactoid shape were seen in the quasi-2D imaging set-up, and encapsulation was found for all the rods studied, indicating that confinement has an important role in this problem. It is likely this is partially related to the impurities being almost immobile in this setup (the bacteria cannot swim, the rods move less and so do the formed tactoids).

We have characterized the rheological behaviour of pure sodium alginate samples or in the presence of Pf4. Both components were evaluated at different concentrations, equal to some of the samples used in the experiments with the confocal microscope, allowing us to associate the results obtained with both techniques. All the samples are fluid shear-thinning and in the presence of the phage, the viscosity increases compared to the pure polymer sample. If the

structures formed are tactoids, the sample shows a more fluid-like behaviour, confirming the lack of structure. On the other hand, the samples in the network range presented a transition from more solid-like to fluid-like with S24P109 appearing to be more structured than S08P119, which agrees with the microscope images.

To further understand the effects of impurities in the system and the relationship with the configurations obtained, it is important to evaluate well-defined surfaces with characterized anchoring. Also, one should evaluate if the geometrical relationships hold for distinct surfaces. Finally, one could explore the effect of confinement, exploring different sizes of tactoids and identifying if geometry, surface, and other parameters lead to encapsulation. Exploring micro-rheology would also offer a good insight into the heterogeneity of the samples. Having these pieces of information is quite important in developing methods to tackle *P. aeruginosa* biofilm, considering the mechanisms for clearance in infected patients.

Bibliography

[1] Willem. Norde. *Colloids and interfaces in life sciences and bionanotechnology: Second edition.* CRC Press, 2011.

[2] Henk N.W. Lekkerkerker and Remco Tuinier. *Colloids and the Depletion Interaction*, volume 833 of *Lecture Notes in Physics.* Springer Netherlands, Dordrecht, 2011.

[3] D. Fennell. Evans and Hakan. Wennerstrom. *The colloidal domain : where physics, chemistry, biology, and technology meet.* Wiley-VCH, 1999.

[4] Lars Onsager. The effects of shape on the interaction of colloidal particles. *Ann. N. Y. Acad. Sci.*, 51(4):627–659, may 1949.

[5] Valerie J. Anderson and Henk N. W. Lekkerkerker. Insights into phase transition kinetics from colloid science. *Nature*, 416(6883):811–815, apr 2002.

[6] Vinothan N. Manoharan. Colloidal matter: Packing, geometry, and entropy. *Science*, 349(6251), 2015.

[7] A. Einstein. Über die von der molekularkinetischen Theorie der Wärme geforderte Bewegung von in ruhenden Flüssigkeiten suspendierten Teilchen. *Ann. d. Phys.*, 322(8):549–560, 1905.

[8] Lars Onsager. Theories of Concentrated electrolytes. *Chem. Rev.*, (1):73–89, 1933.

[9] Lars Onsager. the Effects of Shape on the Interaction of Colloidal Particles. *Ann. N. Y. Acad. Sci.*, 51(4):627–659, 1949.

[10] William G. McMillan and Joseph E. Mayer. The statistical thermodynamics of multicomponent systems. *J. Chem. Phys.*, 13(7):276–305, 1945.

[11] Peter J. Lu and David A. Weitz. Colloidal Particles: Crystals, Glasses, and Gels. *Annu. Rev. Condens. Matter Phys.*, 4(1):217–233, apr 2013.

[12] Sho Asakura and Fumio Oosawa. Interaction between particles suspended in solutions of macromolecules. *J. Polym. Sci.*, 33(126):183–192, 1958.

[13] Sho Asakura and Fumio Oosawa. On interaction between two bodies immersed in a solution of macromolecules. *J. Chem. Phys.*, 22(7):1255–1256, 1954.

[14] Kun Zhao and Thomas G Mason. Directing colloidal self-assembly through roughness-controlled depletion attractions. *Phys. Rev. Lett.*, 99(26):1–4, 2007.

[15] Seymour S. Cohen. the Isolation and Crystallization of Plant Viruses and Other Protein Macro Molecules By Means of Hydrophilic Colloids. *J. Biol. Chem.*, 144(2):353–362, 1942.

[16] R. Leberman. The isolation of plant viruses by means of "simple" coacervates. *Virology*, 30(3):341–347, 1966.

[17] Masao Doi. *Soft Matter Physics*. Oxford University Press, jun 2013.

[18] Pierre Gilles de. Gennes and Jacques. Prost. *The physics of liquid crystals*. Clarendon Press, 1993.

[19] Jonathan V. Selinger. *Introduction to the Theory of Soft Matter*. Soft and Biological Matter. Springer International Publishing, 2016.

[20] V Tsvetkov. Über die molekülanordnung in der anisotrop-flüssigen phase. *Acta Physicochim USSR*, 16:132–147, 1942.

[21] Jorge Viamontes and Jay X. Tang. Continuous isotropic-nematic liquid crystalline transition of F -actin solutions. *Phys. Rev. E*, 67(4):040701, apr 2003.

[22] M. Doi and S. F. Edwards. Dynamics of rod-like macromolecules in concentrated solution. Part 1. *J. Chem. Soc. Faraday Trans. 2*, 74(6):560, 1978.

[23] C. W. Oseen. The theory of liquid crystals. *Trans. Faraday Soc.*, 29(140):883, 1933.

[24] F C Frank. Liquid crystals. On the theory of liquid crystals. *Discuss. Faraday Soc.*, 25(I):19, 1958.

[25] Olivia Shiels. Tactoids of the pf4 bacteriophage. Master's thesis, University of Oxford, 2020.

[26] Sin Doo Lee and Robert B Meyer. Computations of the phase equilibrium, elastic constants, and viscosities of a hard-rod nematic liquid crystal. *J. Chem. Phys.*, 84(6):3443–3448, mar 1986.

[27] Victor G Taratuta, Alan J Hurd, and Robert B Meyer. Light-scattering study of a polymer nematic liquid crystal. *Phys. Rev. Lett.*, 55(2):246–249, jul 1985.

[28] Massimo Bagnani, Paride Azzari, Cristiano De Michele, Mario Arcari, and Raffaele Mezzenga. Elastic constants of biological filamentous colloids: Estimation and implications on nematic and cholesteric tactoid morphologies. *Soft Matter*, 17(8):2158–2169, 2021.

[29] Alexander H. Lewis, Ioana Garlea, José Alvarado, Oliver J. Dammone, Peter D. Howell, Apala Majumdar, Bela M. Mulder, M. P. Lettinga, Gijsje H. Koenderink, and Dirk G.A.L. Aarts. Colloidal liquid crystals in rectangular confinement: Theory and experiment. *Soft Matter*, 10(39):7865–7873, 2014.

[30] Alfred Saupe. Disclinations and Properties of the Directorfield in Nematic and Cholesteric Liquid Crystals. *Mol. Cryst. Liq. Cryst.*, 21(3-4):211–238, jan 1973.

[31] Andrew D Price and Daniel K Schwartz. Anchoring of a nematic liquid crystal on a wettability gradient. *Langmuir*, 22(23):9753–9759, 2006.

[32] T Rasing and I Musevic. *Surfaces and Interfaces of Liquid Crystals*. Springer Berlin Heidelberg, 2010.

[33] Joseph A Castellano. Surface Anchoring of Liquid Crystal Molecules on Various Substrates. *Mol. Cryst. Liq. Cryst.*, 94(1-2):33–41, jan 1983.

[34] B. Jerome. Surface effects and anchoring in liquid crystals. *Reports Prog. Phys.*, 54(3):391–451, 1991.

[35] M. Paul Lettinga, Kyongok Kang, Arnout Imhof, Didi Derks, and Jan K.G. Dhont. Kinetic pathways of the nematic-isotropic phase transition as studied by confocal microscopy on rod-like viruses. *J. Phys. Condens. Matter*, 17(45), 2005.

[36] Pei Xi Wang, Wadood Y Hamad, and Mark J. MacLachlan. Structure and transformation of tactoids in cellulose nanocrystal suspensions. *Nat. Commun.*, 7(May):1–8, 2016.

[37] Kimberly L. Weirich, Shiladitya Banerjee, Kinjal Dasbiswas, Thomas A. Witten, Suriyanarayanan Vaikuntanathan, and Margaret L. Gardel. Liquid behavior of cross-linked actin bundles. *Proc. Natl. Acad. Sci. U. S. A.*, 114(9):2131–2136, 2017.

[38] Patrick W. Oakes, Jorge Viamontes, and Jay X. Tang. Growth of tactoidal droplets during the first-order isotropic to nematic phase transition of F-actin. *Phys. Rev. E - Stat. Nonlinear, Soft Matter Phys.*, 75(6):1–11, 2007.

[39] Peter Prinsen and Paul van der Schoot. Shape and director-field transformation of tactoids. *Phys. Rev. E - Stat. Physics, Plasmas, Fluids, Relat. Interdiscip. Top.*, 68(2):11, 2003.

[40] P. Prinsen and P. Van Der Schoot. Continuous director-field transformation of nematic tactoids. *Eur. Phys. J. E*, 13(1):35–41, 2004.

[41] A. V. Kaznacheev, M. M. Bogdanov, and S. A. Taraskin. The nature of prolate shape of tactoids in lyotropic inorganic liquid crystals. *J. Exp. Theor. Phys.*, 95(1):57–63, jul 2002.

[42] Massimo Bagnani, Gustav Nyström, Cristiano De Michele, and Raffaele Mezzenga. Amyloid Fibrils Length Controls Shape and Structure of Nematic and Cholesteric Tactoids. *ACS Nano*, 13(1):591–600, 2019.

[43] Paride Azzari, Massimo Bagnani, and Raffaele Mezzenga. Liquid–liquid crystalline phase separation in biological filamentous colloids: nucleation, growth and order–order transitions of cholesteric tactoids. *Soft Matter*, 17(27):6627–6636, 2021.

[44] Hamed Almohammadi, Sayyed Ahmad Khadem, Massimo Bagnani, Alejandro D. Rey, and Raffaele Mezzenga. Shape and structural relaxation of colloidal tactoids. *Nat. Commun.*, 13(1):1–10, 2022.

[45] Zvonimir Dogic and Seth Fraden. Development of model colloidal liquid crystals and the kinetics of the isotropic-smectic transition. *Philos. Trans. R. Soc. A Math. Phys. Eng. Sci.*, 359(1782):997–1015, 2001.

[46] Zvonimir Dogic, Kirstin R. Purdy, Eric Grelet, Marie Adams, and Seth Fraden. Isotropic-nematic phase transition in suspensions of filamentous virus and the neutral polymer Dextran. *Phys. Rev. E - Stat. Physics, Plasmas, Fluids, Relat. Interdiscip. Top.*, 69(5):9, 2004.

[47] F. C. Bawden, N. W. Pirie, J. D. Bernal, and I. Fankuchen. Liquid Crystalline Substances from Virus-infected Plants. *Nature*, 138(3503):1051–1052, dec 1936.

[48] Naohito Urakami, Masayuki Imai, Yoh Sano, and Masako Takasu. The isotropic-nematic transition and the phase separation of the tobacco mosaic virus particles with polysaccharide. *J. Chem. Phys.*, 111(5):2322–2328, 1999.

[49] Zvonimir Dogic and Seth Fraden. Ordered phases of filamentous viruses. *Curr. Opin. Colloid Interface Sci.*, 11(1):47–55, 2006.

[50] Patrick R Secor, Johanna M Sweere, Lia A Michaels, Andrey V Malkovskiy, Daniel Lazzareschi, Ethan Katznelson, Jayakumar Rajadas, Michael E Birnbaum, Allison Arrigoni, Kathleen R Braun, Stephen P Evanko, David A Stevens, Werner Kaminsky, Pradeep K Singh, William C Parks, and Paul L Bollyky. Filamentous bacteriophage promote biofilm assembly and function. *Cell Host Microbe*, 18(5):549–559, 2015.

[51] Abul K Tarafder, Andriko von Kügelgen, Adam J Mellul, Ulrike Schulze, Dirk G.A.L. Aarts, and Tanmay A.M. Bharat. Phage liquid crystalline droplets form occlusive sheaths that encapsulate and protect infectious rod-shaped bacteria. *Proc. Natl. Acad. Sci. U. S. A.*, 117(9):4724–4731, 2020.

[52] Hans-Curt Flemming and Jost Wingender. The biofilm matrix. *Nat. Rev. Microbiol.*, 8(9):623–633, sep 2010.

[53] J.A. Colmer-Hamood, N. Dzvova, C. Kruczek, and A.N. Hamood. In Vitro Analysis of Pseudomonas aeruginosa Virulence Using Conditions That Mimic the Environment at Specific Infection Sites. In *Prog. Mol. Biol. Transl. Sci.*, volume 142, pages 151–191. Elsevier B.V., jan 2016.

[54] WHO. Prioritization of pathogens to guide discovery, research and development of new antibiotics for drug-resistant bacterial infections, including tuberculosis. 2017.

[55] Sandra Castang and Simon L. Dove. Basis for the Essentiality of H-NS Family Members in Pseudomonas aeruginosa. *J. Bacteriol.*, 194(18):5101–5109, sep 2012.

[56] M Whiteley, M G Bangera, R E Bumgarner, M R Parsek, G M Teitzel, S Lory, and E P Greenberg. Gene expression in Pseudomonas aeruginosa biofilms. *Nature*, 413(October):860–864, 2001.

[57] Elizabeth B. Burgener, Johanna M. Sweere, Michelle S. Bach, Patrick R. Secor, Naomi Haddock, Laura K. Jennings, Rasmus L. Marvig, Helle Krogh Johansen, Elio Rossi, Xiou Cao, Lu Tian, Laurence Nedelec, Søren Molin, Paul L. Bollyky, and Carlos E. Milla. Filamentous bacteriophages are associated with chronic Pseudomonas lung infections and antibiotic resistance in cystic fibrosis. *Sci. Transl. Med.*, 11(488):1–12, apr 2019.

[58] Jim Manos, Jonathan Arthur, Barbara Rose, Pholawat Tingpej, Carina Fung, Michelle Curtis, Jeremy S. Webb, Honghua Hu, Staffan Kjelleberg, Mark D. Gorrell, Peter Bye, and Colin Harbour. Transcriptome analyses and biofilm-forming characteristics of a clonal Pseudomonas aeruginosa from the cystic fibrosis lung. *J. Med. Microbiol.*, 57(12):1454–1465, dec 2008.

[59] Kerensa E. McElroy, Janice G. K. Hui, Jerry K. K. Woo, Alison W. S. Luk, Jeremy S. Webb, Staffan Kjelleberg, Scott A. Rice, and Torsten Thomas. Strain-specific parallel evolution drives short-term diversification during Pseudomonas aeruginosa biofilm formation. *Proc. Natl. Acad. Sci.*, 111(14), apr 2014.

[60] Johanna M. Sweere, Jonas D. Van Belleghem, Heather Ishak, Michelle S. Bach, Medeea Popescu, Vivekananda Sunkari, Gernot Kaber, Robert Manasherob, Gina A. Suh, Xiou Cao, Christiaan R. de Vries, Dung N. Lam, Payton L. Marshall, Maria Birukova, Ethan Katznelson, Daniel V. Lazzareschi, Swathi Balaji, Sundeep G. Keswani, Thomas R. Hawn, Patrick R. Secor, and Paul L. Bollyky. Bacteriophage trigger antiviral immunity and prevent clearance of bacterial infection. *Science*, 363(6434), mar 2019.

[61] Erin S. Gloag, Guy K. German, Paul Stoodley, and Daniel J. Wozniak. Viscoelastic properties of Pseudomonas aeruginosa variant biofilms. *Sci. Rep.*, 8(1):1–11, 2018.

[62] Markus Wloka, H. Rehage, H. C. Flemming, and J. Wingender. Rheological properties of viscoelastic biofilm extracellular polymeric substances and comparison to the behavior of calcium alginate gels. *Colloid Polym. Sci.*, 282(10):1067–1076, 2004.

[63] M. Wloka, H. Rehage, H. C. Flemming, and J. Wingender. Structure and rheological behaviour of the extracellular polymeric substance network of mucoid Pseudomonas aeruginosa biofilms. *Biofilms*, 2(4):275–283, 2005.

[64] Warren L. Jones, Michael P. Sutton, Ladean Mckittrick, and Philip S. Stewart. Chemical and antimicrobial treatments change the viscoelastic properties of bacterial biofilms. *Biofouling*, 27(2):207–215, 2011.

[65] Lydia C. Powell, Ahmed Sowedan, Saira Khan, Chris J. Wright, Karl Hawkins, Edvar Onsøyen, Rolf Myrvold, Katja E. Hill, and David W. Thomas. The effect of alginate oligosaccharides on the mechanical properties of Gram-negative biofilms. *Biofouling*, 29(4):413–421, 2013.

[66] Kuen Yong Lee and David J. Mooney. Alginate: Properties and biomedical applications. *Prog. Polym. Sci.*, 37(1):106–126, 2012.

[67] Andrea Dodero, Silvia Vicini, Marina Alloisio, and Maila Castellano. Rheological properties of sodium alginate solutions in the presence of added salt: an application of Kulicke equation. *Rheol. Acta*, 59(6):365–374, 2020.

[68] Takahiro Funami, Yapeng Fang, Sakie Noda, Sayaka Ishihara, Makoto Nakauma, Kurt I. Draget, Katsuyoshi Nishinari, and Glyn O. Phillips. Rheological properties of sodium alginate in an aqueous system during gelation in relation to supermolecular structures and Ca2+ binding. *Food Hydrocoll.*, 23(7):1746–1755, 2009.

[69] Carla Fernández-Rico, Taiki Yanagishima, Arran Curran, Dirk G.A.L. Aarts, and Roel P.A. Dullens. Synthesis of Colloidal SU-8 Polymer Rods Using Sonication. *Adv. Mater.*, 31(17), 2019.

[70] Liping Feng, Yanping Cao, Duoxia Xu, Shaojia Wang, and Jie Zhang. Molecular weight distribution, rheological property and structural changes of sodium alginate induced by ultrasound. *Ultrason. Sonochem.*, 34:609–615, 2017.

[71] Oded Orgad, Yoram Oren, Sharon L. Walker, and Moshe Herzberg. The role of alginate in Pseudomonas aeruginosa EPS adherence, viscoelastic properties and cell attachment. *Biofouling*, 27(7):787–798, 2011.

[72] Georgina M.H. Wilkins, Patrick T. Spicer, and Michael J. Solomon. Colloidal system to explore structural and dynamical transitions in rod networks, gels, and glasses. *Langmuir*, 25(16):8951–8959, 2009.

[73] S Bell and K Morris. *An Introduction to Microscopy*. Forensics and criminal justice. Taylor & Francis, 2010.

[74] Yang Yang, Guangdong Chen, Luz J. Martinez-Miranda, Hua Yu, Kun Liu, and Zhihong Nie. Synthesis and Liquid-Crystal Behavior of Bent Colloidal Silica Rods. *J. Am. Chem. Soc.*, 138(1):68–71, 2016.

[75] Peerzada Gh Jeelani, Prajakta Mulay, Rajesh Venkat, and C. Ramalingam. Multifaceted Application of Silica Nanoparticles. A Review. *Silicon*, 12(6):1337–1354, 2020.

[76] Anke Kuijk, Alfons van Blaaderen, and Arnout Imhof. Synthesis of Monodisperse, Rodlike Silica Colloids with Tunable Aspect Ratio. *J. Am. Chem. Soc.*, 133(8):2346–2349, 2011.

[77] Louis B.G. Cortes, Yongxiang Gao, Roel P.A. Dullens, and Dirk G.A.L. Aarts. Colloidal liquid crystals in square confinement: Isotropic, nematic and smectic phases. *J. Phys. Condens. Matter*, 29(6), 2017.

[78] Nico A.J.M. Sommerdijk Wright, John D. Sol-gel materials: chemistry and applications. *Choice Rev. Online*, 38(11):38–6197–38–6197, 2001.

[79] Larry L. Hench and Jon K. West. The Sol-Gel Process. *Chem. Rev.*, 90(1):33–72, 1990.

[80] K. Wan Jang, Seung Hoon Choi, Su Il Pyun, and Mu Shik Jhon. The effects of the water content, acidity, temperature and alcohol content on the acidic sol-gel polymerization of tetraethoxysilane (TEOS) with Monte Carlo simulation. *Mol. Simul.*, 27(1):1–16, 2001.

[81] Kenneth G Sharp. A two-component, non-aqueous route to silica gel. *J. Sol-Gel Sci. Technol.*, 2(1):35–41, 1994.

[82] P. Datskos, J. Chen, and J. Sharma. Addressable morphology control of silica structures by manipulating the reagent addition time. *RSC Adv.*, 4(5):2291–2294, 2014.

[83] Panos Datskos, Georgios Polizos, David A. Cullen, Mahabir Bhandari, and Jaswinder Sharma. Synthesis of Half-Sphere/Half-Funnel-Shaped Silica Structures by Reagent Localization and the Role of Water in Shape Control. *Chem. - A Eur. J.*, 22(52):18700–18704, 2016.

[84] Ryan P. Murphy, Kunlun Hong, and Norman J. Wagner. Synthetic control of the size, shape, and polydispersity of anisotropic silica colloids. *J. Colloid Interface Sci.*, 501:45–53, 2017.

[85] Ulrich Schubert. Part One Sol – Gel Chemistry and Methods. *Sol-Gel Handb. Synth. Charact. Appl.*, pages 1–28, 2015.

[86] Jianhui Zhang, Huaiyong Liu, Zhenlin Wang, and Naiben Ming. Au-induced polyvinylpyrrolidone aggregates with bound water for the highly shape-selective synthesis of silica nanostructure. *Chem. - A Eur. J.*, 14(14):4374–4380, 2008.

[87] Fabian Hagemans, Ravi Kumar Pujala, Danisha S. Hotie, Dominique M. E. Thies-Weesie, D. A. Matthijs de Winter, Johannes D. Meeldijk, Alfons van Blaaderen, and Arnout Imhof. Shaping Silica Rods by Tuning Hydrolysis and Condensation of Silica Precursors. *Chem. Mater.*, 31(2):521–531, jan 2019.

[88] Panos Datskos and Jaswinder Sharma. Synthesis of segmented silica rods by regulation of the growth temperature. *Angew. Chemie - Int. Ed.*, 53(2):451–454, 2014.

[89] Qiyu Yu, Kun Wang, Jing Zhang, Mingyang Liu, Yuanyuan Liu, and Chao Cheng. Synthesis of anisotropic silica colloids. *RSC Adv.*, 7(60):37542–37548, 2017.

[90] Tom F. O'Mahony and Michael A. Morris. Hydroxylation methods for mesoporous silica and their impact on surface functionalisation. *Microporous Mesoporous Mater.*, 317(February):110989, 2021.

[91] John A. Howarter and Jeffrey P. Youngblood. Optimization of silica silanization by 3-aminopropyltriethoxysilane. *Langmuir*, 22(26):11142–11147, 2006.

[92] Anke Kuijk, Arnout Imhof, Margriet H.W. Verkuijlen, Thijs H. Besseling, Ernst R.H. Van Eck, and Alfons Van Blaaderen. Colloidal silica rods: Material properties and fluorescent labeling. *Part. Part. Syst. Charact.*, 31(6):706–713, 2014.

[93] Joonyeong Kim, Joungmo Cho, Paul M. Seidler, Nicholas E. Kurland, and Vamsi K. Yadavalli. Investigations of chemical modifications of amino-terminated organic films on silicon substrates and controlled protein immobilization. *Langmuir*, 26(4):2599–2608, 2010.

[94] M. C. Capel-Sanchez, L. Barrio, J. M. Campos-Martin, and J. L.G. Fierro. Silylation and surface properties of chemically grafted hydrophobic silica. *J. Colloid Interface Sci.*, 277(1):146–153, 2004.

[95] Tuo Ji, Chi Ma, Logan Brisbin, Liwen Mu, Christopher G. Robertson, Yalin Dong, and Jiahua Zhu. Organosilane grafted silica: Quantitative correlation of microscopic surface characters and macroscopic surface properties. *Appl. Surf. Sci.*, 399:565–572, 2017.

[96] Yongxiang Gao, Violet Farkas, Roel P.A. Dullens, and Dirk G.A.L. Aarts. Structural disorder, filament growth and self-poisoning in short rods confined onto a flat wall. *Soft Matter*, 13(46):8678–8683, 2017.

[97] M. J. Hey and P. G. Kippax. Surface tensions of mixed aqueous solutions of tert-butanol and n-pentanol. *Colloids Surfaces A Physicochem. Eng. Asp.*, 262(1-3):198–203, 2005.

[98] Pei Xi Wang and Mark J. MacLachlan. Liquid crystalline tactoids: Ordered structure, defective coalescence and evolution in confined geometries. *Philos. Trans. R. Soc. A Math. Phys. Eng. Sci.*, 376(2112), 2018.

[99] Andy Tran, Wadood Y. Hamad, and Mark J. MacLachlan. Tactoid Annealing Improves Order in Self-Assembled Cellulose Nanocrystal Films with Chiral Nematic Structures. *Langmuir*, 34(2):646–652, 2018.

[100] Claudia Ferreiro-Córdova, C. Patrick Royall, and Jeroen S. van Duijneveldt. Anisotropic viscoelastic phase separation in polydisperse hard rods leads to nonsticky gelation. *Proc. Natl. Acad. Sci. U. S. A.*, 117(7):3415–3420, 2020.

[101] J. B. Clarke, J. W. Hastie, L. H. E. Kihlborg, R. Metselaar, and M. M. Thackeray. Definitions of terms relating to phase transitions of the solid state (iupac recommendations 1994). *Pure and Applied Chemistry*, 66(3):577–594, 1994.

[102] Adam Mellul. Liquid crystal phase behaviour of the pf4 bacteriophage. Master's thesis, University of Oxford, 2019.

[103] Alejandro Cuetos and Marjolein Dijkstra. Kinetic pathways for the isotropic-nematic phase transition in a system of colloidal hard rods: A simulation study. *Phys. Rev. Lett.*, 98(9):1–4, 2007.

[104] M. P.B. Van Bruggen, J. K.G. Dhont, and H. N.W. Lekkerkerker. Morphology and kinetics of the isotropic-nematic phase transition in dispersions of hard rods. *Macromolecules*, 32(7):2256–2264, 1999.

[105] Jorge Viamontes, Patrick W. Oakes, and Jay X. Tang. Isotropic to nematic liquid cystalline phase transition of F-actin varies from continuous to first oder. *Phys. Rev. Lett.*, 97(11):1–4, 2006.

[106] Z. X. Zhang and Jeroen S. Van Duijneveldt. Isotropic-nematic phase transition of non-aqueous suspensions of natural clay rods. *J. Chem. Phys.*, 124(15), 2006.

[107] M. Paul Lettinga, Kyongok Kang, Peter Holmqvist, Arnout Imhof, Didi Derks, and Jan K.G. Dhont. Nematic-isotropic spinodal decomposition kinetics of rodlike viruses. *Phys. Rev. E - Stat. Nonlinear, Soft Matter Phys.*, 73(1):1–7, 2006.

[108] Anna Modlinska, Ahmed M. Alsayed, and Thomas Gibaud. Condensation and dissolution of nematic droplets in dispersions of colloidal rods with thermo-sensitive depletants. *Sci. Rep.*, 5(July):1–10, 2015.

[109] H. H. Wensink and G. J. Vroege. Isotropic-nematic phase behavior of length-polydisperse hard rods. *J. Chem. Phys.*, 119(13):6868–6882, 2003.

[110] Valentin Lulevich, Yi Ping Shih, Su Hao Lo, and Gang Yu Liu. Cell tracing dyes significantly change single cell mechanics. *J. Phys. Chem. B*, 113(18):6511–6519, 2009.

[111] Luc S. De Clerck, Chris H. Bridts, Annemie M. Mertens, Marleen M. Moens, and Wim J. Stevens. Use of fluorescent dyes in the determination of adherence of human leucocytes to endothelial cells and the effect of fluorochromes on cellular function. *J. Immunol. Methods*, 172(1):115–124, 1994.

[112] F. Guillermo Díaz Baños, Ana I. Díez Peña, J. Ginés Hernánez Cifre, M. Carmen López Martínez, Alvaro Ortega, and José García De La Torre. Influence of ionic strength on the flexibility of alginate studied by size exclusion chromatography. *Carbohydr. Polym.*, 102(1):223–230, 2014.

[113] G. J. Vroege and H N W Lekkerkerker. Phase transitions in lyotropic colloidal and polymer liquid crystals. *Reports Prog. Phys.*, 55(8):1241–1309, aug 1992.

[114] Jing Yan and Bonnie L. Bassler. Surviving as a Community: Antibiotic Tolerance and Persistence in Bacterial Biofilms. *Cell Host Microbe*, 26(1):15–21, 2019.

[115] Theo Odijk. Elastic constants of nematic solutions of rod-like and semi-flexible polymers. *Liq. Cryst.*, 1(6):553–559, 1986.

[116] A. L. Alexe-Ionescu, G. Barbero, and L. Komitov. Anchoring of nematic liquid crystals on a thin polymeric film. *Phys. Rev. E - Stat. Nonlinear, Soft Matter Phys.*, 77(5):1–8, 2008.

[117] H. Hakemi. Elastic constants in dilute poly(styrene)/nematic liquid crystal solutions - Effects of concentration and molecular weight. *Polymer (Guildf).*, 40(14):4099–4103, 1999.

[118] M. B. Hamaneh and P. L. Taylor. Simulated anchoring of a nematic liquid crystal at a polymer surface. *Phys. Rev. E - Stat. Nonlinear, Soft Matter Phys.*, 77(2):1–7, 2008.

[119] Giovanni Barbero and Luiz Roberto Evangelista. *Adsorption Phenomena and Anchoring Energy in Nematic Liquid Crystals*. CRC Press, jul 2005.

[120] Stephen P. Diggle and Marvin Whiteley. Microbe profile: Pseudomonas aeruginosa: Opportunistic pathogen and lab rat. *Microbiol. (United Kingdom)*, 166(1):30–33, 2020.

[121] B. Gottenbos, H. C. Van Der Mei, H. J. Busscher, D. W. Grijpma, and J. Feijen. Initial adhesion and surface growth of Pseudomonas aeruginosa on negatively and positively charged poly(methacrylates). *J. Mater. Sci. Mater. Med.*, 10(12):853–855, 1999.

[122] Yang Liu, Ching Hong Yang, and Jin Li. Influence of extracellular polymeric substances on Pseudomonas aeruginosa transport and deposition profiles in porous media. *Environ. Sci. Technol.*, 41(1):198–205, 2007.

[123] C. H. Bolster, B. Z. Haznedaroglu, and S. L. Walker. Diversity in Cell Properties and Transport Behavior among 12 Different Environmental Escherichia coli Isolates . *J. Environ. Qual.*, 38(2):465–472, 2009.

[124] Manoranjan Arakha, Mohammed Saleem, Bairagi C. Mallick, and Suman Jha. The effects of interfacial potential on antimicrobial propensity of ZnO nanoparticle. *Sci. Rep.*, 5:1–10, 2015.

[125] Yueqi Zhang, Bin Du, Yuting Wu, Zhiwei Liu, Jiang Wang, Jianjie Xu, Zhaoyang Tong, Xihui Mu, and Bing Liu. Fe3 O4 @PDA@PEI Core-Shell Microspheres as a Novel Magnetic Sorbent for the Rapid and Broad-Spectrum Separation of Bacteria in Liquid Phase. *Materials (Basel).*, 15(6), 2022.

[126] Jeffery Errington and Lizah T. van der Aa. Microbe profile: Bacillus subtilis: Model organism for cellular development, and industrial workhorse. *Microbiol. (United Kingdom)*, 166(5):425–427, 2020.

[127] Vitaly L Ginzburg and Lev D Landau. On the theory of superconductivity. In *On superconductivity and superfluidity*, pages 113–137. Springer, 2009.

[128] Matthew Mata, Carlos J. Garcia-Cervera, and Hector D. Ceniceros. Ordering kinatics of a conserved binary mixture with a nematic liquid crystal component. *Journal of Non-Newtonian Fluid Mechanics*, 212:18–27, 2014.

[129] A. V. Kaznacheev, M. M. Bogdanov, and A. S. Sonin. The influence of anchoring energy on the prolate shape of tactoids in lyotropic inorganic liquid crystals. *Journal of Experimental and Theoretical Physics*, 97(6):1159–1167, 2003.

[130] John W Cahn and John E Hilliard. Free energy of a nonuniform system. i. interfacial free energy. *The Journal of chemical physics*, 28(2):258–267, 1958.

[131] Samuel M Allen and John W Cahn. On tricritical points resulting from the intersection of lines of higher-order transitions with spinodals. *Scripta Metallurgica*, 10(5):451–454, 1976.

[132] Samuel M Allen and John W Cahn. Coherent and incoherent equilibria in iron-rich iron-aluminum alloys. *Acta Metallurgica*, 23(9):1017–1026, 1975.

[133] Wells GE Logg A, Mardal KA. *Automated solution of differential equations by the finite element method: the FEniCS book*, volume 84. Springer Science and Business Media, 2012.

[134] Colin Kleanthous and Judith P. Armitage. The bacterial cell envelope. *Philos. Trans. R. Soc. B Biol. Sci.*, 370(1679):1–17, 2015.

[135] Anton P. Le Brun, Luke A. Clifton, Candice E. Halbert, Binhua Lin, Mati Meron, Peter J. Holden, Jeremy H. Lakey, and Stephen A. Holt. Structural characterization of a model gram-negative bacterial surface using lipopolysaccharides from rough strains of escherichia coli Biomacromolecules. *Biomacromolecules*, 15(8):3213, 2014.

[136] Christian R.H. Raetz and Chris Whitfield. Lipopolysaccharide endotoxins. *Annu. Rev. Biochem.*, 71:635–700, 2002.

[137] Blake Bertani and Natividad Ruiz. Function and Biogenesis of Lipopolysaccharides. *EcoSal Plus*, 8(1), 2018.

[138] Vijay Kumar and Niti Nipun Sharma. Synthesis of hydrophilic to superhydrophobic su8 surfaces. *Journal of Applied Polymer Science*, 132(18), 2015.

[139] K. S. Zerda, C. P. Gerba, K. C. Hou, and S. M. Goyal. Adsorption of viruses to charge-modified silica. *Appl. Environ. Microbiol.*, 49(1):91–95, 1985.

[140] Oliver J. Dammone, Ioannis Zacharoudiou, Roel P.A. Dullens, Julia M. Yeomans, M.P. Lettinga, and Dirk G.A.L. Aarts. Confinement induced splay-to-bend transition of colloidal rods. *Phys. Rev. Lett.*, 109(10):1–5, 2012.

[141] Gebhard Schramm. *A Practical Approach to Rheology and Rheometry*. Gebrueder HAAKE, 1994.

[142] H A Barnes, J.F. Hutton, and K. Walters F.R.S. *An Introdution to Rheology*. Elsevier, 1993.

[143] Ethan E. Mann and Daniel J. Wozniak. Pseudomonas biofilm matrix composition and niche biology. *FEMS Microbiol. Rev.*, 36(4):893–916, 2012.

[144] Masao Doi and Sam F. Edwards. Dynamics of rod-like macromolecules in concentrated solution. Part 2. *J. Chem. Soc. Faraday Trans. 2*, 74:918, 1978.

[145] Christian Lang, Joachim Kohlbrecher, Lionel Porcar, Aurel Radulescu, Karin Sellinghoff, Jan Karel George Dhont, and Minne Paul Lettinga. Microstructural Understanding of the Length- and Stiffness-Dependent Shear Thinning in Semidilute Colloidal Rods. *Macromolecules*, 52(24):9604–9612, dec 2019.

[146] Christian Lang and Minne Paul Lettinga. Shear Flow Behavior of Bidisperse Rodlike Colloids. *Macromolecules*, 53(7):2662–2668, 2020.

[147] R.G. Larson. *The Structure and Rheology of Complex Fluids*. Oxford University Press.